

043  
PAD  
14693

MEASUREMENTS OF COMPACT RADIO SOURCE SIZE AND  
STRUCTURE OF COMETARY ION TAILS USING  
INTERPLANETARY SCINTILLATION  
AT 103 MHz

BY

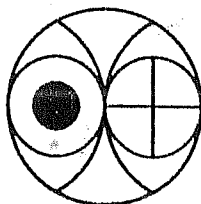
JANARDHAN PADMANABHAN

Ph.D. THESIS  
NOVEMBER 1991

043



B14693



PHYSICAL RESEARCH LABORATORY  
AHMEDABAD - 380 009  
INDIA

043  
PAD

MEASUREMENTS OF COMPACT RADIO SOURCE SIZE AND  
STRUCTURE OF COMETARY ION TAILS USING  
INTERPLANETARY SCINTILLATION  
AT 103 MHz

BY

JANARDHAN PADMANABHAN

PHYSICAL RESEARCH LABORATORY  
AHMEDABAD - 380 009  
INDIA

A THESIS  
SUBMITTED TO THE GUJARAT UNIVERSITY  
FOR THE DEGREE OF

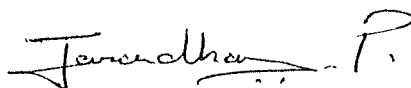
DOCTOR OF PHILOSOPHY

NOVEMBER 1991



# C E R T I F I C A T E

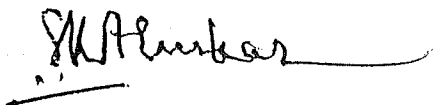
*I hearby declare that the work presented in this thesis is original and has not formed the basis for the award of any degree or diploma by any University or Institution.*



JANARDHAN PADMANABHAN  
(Author)

Physical Research Laboratory  
Ahmedabad - 380 009  
India.

CERTIFIED BY:



Prof. S. K. Alurkar  
(Thesis Supervisor)

Physical Research Laboratory  
Radio Astronomy Division  
Ahmedabad -380 009.  
India.

*Come, let us on the sea-shore stand  
And wonder at a grain of sand;  
And then into the meadow pass  
And marvel at a blade of grass;  
Or cast our vision high and far  
And thrill with wonder at a star.*

Robert Service, The Wonderer.

# Contents

List of Figures.....	v
List of Plates.....	x
List of Tables.....	xi
Research Publications.....	xiii
Papers Presented at Symposia and Conferences.....	xiv
Acknowledgements.....	xv
A Brief Summary of the Thesis .....	xviii

## Chapter I

INTRODUCTION.....	1
1.1 The Visible and Radio Windows.....	4
1.2 The Interplanetary Medium.....	6
1.3 IPS As a Probe to the Interplanetary and Interstellar Media.....	10
1.4 Comets - Their Origin and Relevance to Astronomy.....	12
1.4.1 Present Day Concepts.....	14
1.4.2 Optical and IPS Observations Of Comets. ....	14

1.5	Summary.....	16
-----	--------------	----

## Chapter - II

### INTERPLANETARY SCINTILLATION AND RELEVANT THEORY..... 19

2.1	Introduction.....	19
2.2	Arcsecond Resolution.....	21
2.3	Phase Modulation of a plane Wave Due to the IPM.....	23
2.4	The Fresnel Filter.....	26
2.5	Scintillation Index.....	32
2.6	Bandwidth Effect.....	36
2.7	Effect of Finite Source Size.....	38
2.8	Summary.....	40

## Chapter - III

### THE THALTEJ RADIO TELESCOPE AND ASSOCIATED INSTRUMENTATION..... 45

3.1	Introduction.....	45
3.2	The Thaltej Antenna Array.....	49
3.2.1	The Balun and Low Noise Preamplifier.....	52
3.3	The Correlation Receiver.....	60
3.3.1	The Scintillometer.....	66
3.3.2	Sensitivity of the Telescope.....	68
3.4	The 20,000 m <sup>2</sup> Array.....	80

3.5	The Digital Data Acquisition System.....	83
3.5.1	Source Library.....	86
3.5.2	Hex Encoder.....	87
3.5.3	Control Circuit.....	87
3.5.4	The Analogue-to-Digital (A/D) Converter.....	88
3.5.5	Mux-controller.....	89
3.5.6	Data Multiplexer.....	89
3.5.7	Pertec Controller.....	90

## Chapter - IV

	MEASUREMENTS OF ANGULAR SOURCE SIZE AND INTERSTELLAR SCATTERING AT 103 MHz.....	93
4.1	Introduction.....	93
4.2	The Method of Source Diameter Measurements Using IPS.....	97
4.3	Measurement of Scintillation Index.....	102
4.4	Measurement of Interstellar Scattering at 103 MHz.....	119
4.5	Conclusion.....	123

## Chapter - V

	ENHANCED IPS DUE TO COMETARY ION TAILS AT 103 MHZ - COMETS AUSTIN AND HALLEY.....	125
--	---	-----

5.1	Introduction.....	125
5.2	Observations and Analysis - Comet Austin (1989 c1) .....	127
5.2.1	Discussions and Conclusions.....	142
5.3	Enhanced Scintillations Due to Comet Halley .....	143
5.3.1	Observations and Analysis - Comet Halley.....	146
5.3.2	Estimation of the Amount of Enhancement from Other Causes.....	162
5.3.3	Results and Discussions.....	168
5.4	Conclusions.....	172

## Chapter - VI

### SCOPE FOR FUTURE WORK USING THE ENHANCED THALTEJ TELESCOPE..... 174

6.1	Angular Distribution of Radio Sources and IPS Surveys.....	174
6.2	Occultation Observations by Cometary Ion Tails.....	176
6.3	Velocity Measurements and Large-scale Structure of the Interplanetary Medium.....	177

### REFERENCES..... 182

# List of Figures

Figure No.		Page No.
1.1	Pictorial representation of the development of interplanetary scintillation.	3
2.1	IPS Geometry for the thin screen approximation.	22
2.2a - 2.2d	Development of an angular spectrum due to a phase modulating thin screen.	27
2.3a - 2.3c	Effect of the Fresnel Filter function on a Gaussian spectrum of phase fluctuations.	31
2.4	Development of a 2-D spectrum of intensity fluctuations on the observers plane.	42
3.1	Block diagram of IPS telescope at Thaltej.	48
3.2	Schematic representation of the 10,000 m <sup>2</sup> dipole array at Thaltej.	50
3.3	Circuit diagram of the Low Noise Preamplifier used with the 10,000 m <sup>2</sup> array.	55
3.4	Normalized declination power response of the Thaltej array, formed by one of two identical Butler Matrices.	59
3.5	Block diagram of the dual channel correlation receiver at Thaltej.	62
3.6 a	Square law detector output Vs input power, with and without Automatic Gain control - Sin Channel.	63

Figure No.		Page No.
3.6 b	Square law detector output Vs input power, with and without Automatic Gain control - Cos Channel	64
3.6 c	Square law detector output Vs input power, with and without Automatic Gain control - Sin and Cos Channels combined.	65
3.7	Block Diagram of the total power squaring scintillometer.	67
3.8	Positions of observed sources - in ecliptic coordinates.	75
3.9	Effective deflection Vs. Flux at 103 MHz - with and without Automatic Gain Control.	76
3.10	Block diagram of the enhanced 20,000 m <sup>2</sup> array, Thaltej.	82
3.11	Block diagram of digital data acquisition system used with the 10,000 m <sup>2</sup> array.	84
3.12	Block Diagram of the PC/XT based data acquisition system.	85
4.1	Theoretical curves for scintillation index as a function of elongation for different source sizes.	101
4.2 a	Variation of angular size with changing scintillation index ratio ( $\mathcal{R}$ ). $\mathcal{R}$ is calculated at $\epsilon_1 = 30^\circ$ and $\epsilon_2 = 60^\circ$ .	103
4.2 b	Variation of angular size with changing scintillation index ratio ( $\mathcal{R}$ ). $\mathcal{R}$ is calculated at $\epsilon_1 = 30^\circ$ and $\epsilon_2 = 70^\circ$ .	104
4.3 a	Log-log plot of scintillometer calibration in 1985.	107
4.3 b	Log-log plot of scintillometer calibration in 1986.	108



Figure No.		Page No.
4.3 c	Log-log plot of scintillometer calibration in 1987.	109
4.4 a	Observations of scintillation index (m) as a function of solar elongation ( $\epsilon$ ) for the sources 3C119 and 3C144.	110
4.4 b	Observations of scintillation index (m) as a function of solar elongation ( $\epsilon$ ) for the sources 3C147 and 3C48.	111
4.4 c	Observations of scintillation index (m) as a function of solar elongation ( $\epsilon$ ) for the sources 3C196 and CTA21.	112
4.4 d	Observations of scintillation index (m) as a function of solar elongation ( $\epsilon$ ) for the sources 3C237 and 3C222.	113
4.4 e	Observations of scintillation index (m) as a function of solar elongation ( $\epsilon$ ) for the sources 3C446 and 3C459.	114
4.4 f	Observations of scintillation index (m) as a function of solar elongation ( $\epsilon$ ) for the sources 3C2 and 3C298.	115
4.4 g	Observations of scintillation index (m) as a function of solar elongation ( $\epsilon$ ) for the sources 3C273 and 3C287.	116
4.5	Scatter plot of the derived values of $\Theta_s^2$ as a function of galactic latitude $ b $ .	121
4.6	The values of $\langle \Theta_s^2 \rangle$ for different ranges of galactic latitude $ b $ .	122

Figure No.		Page No.
5.1	Path of comet Austin projected on to the sky, showing the nuclear positions and tail axis at Ahmedabad transit on 13th and 14th May 1990.	130
5.2	Relative positions of Sun, Earth and Comet Austin - May 1990.	132
5.3	Relative positions of Sun Earth and Comet Halley - December 1985 and February 1986.	135
5.4	Normalized power spectrum of 2204+29 (3C441) during its occultation by the tail of Comet Austin on May 13, 1990.	139
5.5	Variation of scintillation index with changing solar elongation for the source 2314+03 (3C459). Also shown are the scintillation indices measured between 16 and 21 Dec. 1985 when the tail of comet Halley occulted the source.	147
5.6	Tail axis of comet Halley plotted for different values of position angle.	150
5.7	Actual path of the source 3C459 through the tail of comet Halley for a tail-lag of $-3^\circ$ .	151
5.8a - 5.8c	Normalized power spectra of 3C459 during 16 to 18 Dec. 1985.	155
5.8d - 5.8f	Normalized power spectra of 3C459 during 19 to 21 Dec. 1985.	156
5.9a - 5.9b	Variation of scale size (a) and rms electron density deviation ( $\Delta N$ ) as a function of distance on either side of the comet Halley's axis.	161
5.10	Spacecraft measurements of bulk speed (v), ion density (N) and Temperature ( $^\circ$ K) during the Bartels solar rotation period 2082 in December 1985.	163

Figure No.		Page No.
5.11	Preliminary H - Alpha solar synoptic chart for carrington rotation number 1769 showing the positions of coronal holes detected in 10830Å.	164
6.1	Solar wind velocities, derived using the single station technique, for the year 1986.	179
6.2	Solar wind velocities, derived using the single station technique, for the year 1990.	180

# List of Plates

Plate No.		Page No.
1	The Thaltej 10,000 m <sup>2</sup> dipole array as seen from below the reflecting plane.	46
2	Some typical recordings of 3C48, a strongly scintillating radio source showing the day-to-day variations in scintillation.	72
3	The chart recordings of the source 2204+29 during its occultation by the tail of comet Austin on May 13 and 14 1990.	128
4	A masked and contrast enhanced photo of comet Halley. ( <i>UK Schmidt Telescope, Royal Observatory, Edinburgh.</i> )	153
5	The chart recordings of the source 2314+038 during its occultation by the tail of comet Halley between 17 and 21 December 1985.	154

# List of Tables

Table No.		Page No.
1.1	Some relevant properties of the solar wind.	9
3.1	Balun characteristics.	54
3.2	Characteristics of the low noise preamplifier.	56
3.3	Characteristics of the Butler matrix.	58
3.4	Sources used to measure effective deflection as a function of flux at 103 MHz.	77
3.5	Interferometric observations of Cas A.	79
4.1	Calculated values of scintillation index at 103 MHz for different source sizes.	100
4.2	Source sizes determined at 103 MHz.	117
4.3	Comparison of Diameter estimates at different frequencies.	118
5.1	Occulted source elongations for different events.	133
5.2	Comet Austin Parameters.	136
5.3	Occulted and control source parameters during comet Austin Observations.	137
5.4	Estimated scale sizes and rms electron density deviations $\Delta N$ in the tail of comet Austin.	141
5.5	Source parameters during its occultation by comet Halley.	148

Table No.		Page No.
5.6	Spectral widths and rms phase deviations.	159
5.7	Scale sizes and rms electron density deviations $\Delta N$ for various velocities.	160
5.8	Estimated enhancements for different $\Delta N$ .	167
5.9	Scale Size and rms electron density deviations for a single velocity of $100 \text{ km sec}^{-1}$ .	170

# Research Publications

1. Quasar Enhanced.  
Alurkar, S.K., Sharma, A.K., Janardhan, P. and Bhonsle, R.V. (1989).  
*Nature* 338, 211.
2. Three-Site Solar Wind Observatory.  
Alurkar, S.K., Bobra, A.D., Nirman, N.S., Venat, P., and  
Janardhan, P. (1989 ). *Indian Journal of Pure and Applied Physics* 27,  
322.
3. Interplanetary Scintillation Network for 3-Dimensional Space  
Exploration in India.  
Bhonsle, R.V., Alurkar, S.K., Bobra, A.D., Lali, K.S., Nirman, N.S.,  
Venat, P., Sharma, A.K., and Janardhan, P. (1990). *Acta Astronautica*  
21, No.3, 189.
4. Enhanced Radio Source Scintillations due to Comet Austin(1989 c1).  
Janardhan, P., Alurkar, S.K., Bobra, A.D., and Slee, O.B.(1991a)  
*Aust. J. of Phys.* 44, No. 5, 565.
5. Power Spectral Analysis of Enhanced Scintillation of Quasar 3C459  
Due to Comet Halley.  
Janardhan, P., Alurkar, S.K., Bobra, A.D., Slee, O.B. and Waldron, D.  
(1991b). - *Aust. J. of Phys.* (In press).
6. Measurements of Compact Radio Source Size and Interstellar  
Scattering at 103 MHz Using Interplanetary Scintillation.  
Janardhan P. and Alurkar S.K. (Communicated).

# Papers Presented at Symposia and Conferences

1. Estimation of Solar Wind Velocity from the Three-Station IPS Observatory - India.  
Janardhan. P.  
*Proc. of the Indo-U.S. Workshop on IPS and Solar Activity* - Feb. 1988. (1991). pp 83.
2. Enhanced Scintillation of Radio Source 2204+29 By comet Austin (1989 c1) At 103 MHz.  
Janardhan, P., Alurkar, S.K., Bobra, A.D., Slee, O.B.  
(Presented at the Fourteenth Meeting of the Astronomical Society of India - Jan 29 to Feb 1, 1991).
3. A Summary of Radio Observations of Enhanced Scintillations Due to Cometary Ion Tails at 103 MHz.  
Janardhan. P.  
(Presented at the Indo-US workshop On Interplanetary Scintillation and Propagating Disturbances, Ahmedabad, Sept. 1991).
4. Possible Contribution of a Solar Transient Due to Enhanced Scintillation of a Quasar.  
Janardhan P. and Alurkar S.K.  
(Presented at the Symposium on Solar Connection with Transient Interplanetary processes (S O L T I P). September 30 to October 5, 1991, Liblice, Czechoslovakia).



# ACKNOWLEDGEMENTS

*To begin with I would like to express my thanks and gratitude to my thesis supervisor Prof. S. K. Alurkar who was responsible for the direction of this work. An experimental project of this nature, typically spanning 4-5 years, is based upon a good understanding of the basic physical processes involved and a wide and varied experience. During the course of this work, I have drawn upon both the knowledge and the experience of Prof. Alurkar through very many enlightening discussions and arguments, covering all aspects of meter wavelength radio astronomy. I have always found Prof. Alurkar ready to set aside other work in order to explain a viewpoint or discuss a problem. His incisive wit and enthusiasm has made my work much more of a pleasure and lot less of a chore than it otherwise might have been.*

*Two persons I would particularly like to thank here are Mr. A. D. Bobra, my good friend and colleague, and Prof. R.V. Bhonsle. I have found them both to have a deep understanding of radio telescopes and associated hardware, and while being very demanding at work, have both been willing to discuss or help in any way possible, at all hours of the day or night. It has been a pleasure to know them and work with them.*

*I am grateful to both Mr. S. L. Kayasth and Mr. A. H. Desai who have helped me constantly either on the field, while making tests or repairs of the antenna, or off during calibration procedures, documentation, and routine observations. Their sense of humour has on very many occasions provided the necessary impetus to get back to the antenna, on hot Ahmedabad summer days, during work in the field. I am also grateful to C.S. Krishnakumar for the help I received from him in scaling a large number of chart recordings, to Ms. Medha Alurkar for her help in programming, and to Mr. D. Stephen for typing many portions of the manuscript. Thanks are also due to my other colleagues at*

*Thaltej Ms. Harsha, Ms.Modi, Ms Vijaylakshmi, Dr. Vats, Dr. Sharma, K.J. Shah, Ali, Vishwanathan, Venat, Pancholi, Vinchhi, Phadke, Nirman, Dalal, Namisha, Lali, and R.C. Shah for their cooperation. Thanks are also due to Sandeep and Vishal from the field sites at Rajkot and Surat for taking care of the daily running of the outstations. It has been a pleasure to know them all and be their colleague.*

*The Director, Prof.R.K.Varma, and all the other faculty members at PRL deserve thanks for their encouragement and help. Particularly, discussions with Dr. B. Sitaram have been most enlightening and I'm grateful. I would also like to thank Dr. Ambastha and Dr. Bhatanagar of the Udaipur Solar observatory for their cooperation, help and encouragement. Mr. Ranpura of the photographic and documentation section requires special mention for his help in printing all the photos that went into this thesis and various publications, I am thankful to him for his meticulous work. The staff of the PRL library have also been most cooperative and I'd like to say here that I'm obliged.*

*I would like to express my thanks to Prof. Antony Hewish of the Mullard Radio Astronomy Observatory, Cambridge, for his continued interest in my work and for his encouragement, discussions and ideas. It was for me an honor to have the opportunity to meet, interact and work with Prof. Hewish. His bubbling nature coupled with a child like curiosity, an unparalleled enthusiasm for IPS and a deep commitment to learning and science has deeply impressed, inspired and motivated me. I would also like to thank Dr. Murray Dryer, Dr. Zdenka Smith, Dr. Thomas Detman and Dr. Richard Grubb from the National Oceanic and Atmospheric Administration, Boulder U.S.A.; Dr. Chris Salter from the National Radio Astronomy Observatory, Greenbank, U.S.A. and Dr. Bruce Slee from the Australia Telescope National Facility, NSW, Australia. The regular exchange of thoughts and ideas with them on the electronic mail has been very useful. My interaction with Dr. M. Kojima, from the Solar Terrestrial Environment Laboratory, Nagoya University, Japan, though very short, was most rewarding and I would like to thank him.too. I am very grateful to Duncan Waldron from the UK Schmidt Telescope Unit, Royal Observatory, Edinburgh, for providing me with a contrast enhanced print of comet Halley and for allowing me to make copies of it for the thesis.*

*Debates and discussions on a wide variety of topics, with students from various fields of research, and with different educational and cultural backgrounds, is a regular feature of a student's life at PRL. The inspirations, frustrations prejudices and occasional triumphs of a large number of people thus run through this thesis unseen and unacknowledged, except here where I would like to say that all these people have been my colleagues, but more importantly are my friends. They are - Subramanian, Krishnakumar, Krishnan, Raju, Sarangi, Mathews, Vijaykumar, Maqbool, Debi, Bhaskaran, and Banerjee.*

*I would also like to express my thanks to my young friend Anand Jain. His enthusiasm, optimistic outlook and courage in the face of very many personal difficulties has been very encouraging and inspiring especially when the going was tough and dull. It has given me immense pleasure to know him, his parents and all the other members of his family and to have him as a friend.*

*Finally my thanks are due to my parents who made it all possible, to T.S.Ganesh (VU2TS) for the long pleasant hours I've spent with him during my years in school and college, and from whom I've learnt so much, to my sisters for their encouragement, support and love, to Kanishka for her long and beautifully written letters, and to Rekha for her company, for the regular and long hours of discussions we had during her stay at PRL and for the continued contact she maintained, after she left, through letters and by electronic mail. Her tremendous enthusiasm and motivation for work, positive outlook and constantly cheerful attitude has, for me, always been a source of wonder and pleasure.*

*Financial assistance for this work came from the Departments of Space and Science & Technology, Govt. of India and a Special Foreign Currency (SFC) project, No. NA87AA-D-ER046, under the Indo-US collaboration.*

## A BRIEF SUMMARY OF THE THESIS

The work presented in this thesis is essentially divided into two distinct parts. The first part concerns studies of compact radio source size structure using IPS and related studies of interstellar scattering (ISS) at 103 MHz. The second part uses the IPS technique to study the plasma contained in the cometary ion tails. The entire work was carried out using the large filled-aperture dipole array at Thaltej, Ahmedabad. This telescope, operating at 103 MHz, is one of a network\* of three similar telescopes of the Radio Astronomy Group of the Physical Research Laboratory and is used to study the interplanetary medium (IPM) by the method of IPS. Since it began operating in mid-1984, a large amount of data has been gathered and since then the physical area of the telescope has been enhanced from  $5,000 \text{ m}^2$  in 1984 to  $10,000 \text{ m}^2$  in 1986 and finally  $20,000 \text{ m}^2$  in 1990.

The first part of this work has made use of the data obtained at Thaltej between mid-1984 and end of 1987 to determine the angular source sizes of a number of radio sources. The results of this analysis were then used in conjunction with the data available at 151.5 MHz (Readhead and

Hewish 1972) to determine the angular broadening caused at 103 MHz due to interstellar scattering as a function of galactic latitude. Small components in radio sources may be measured by high resolution techniques other than IPS, the most important method being the Very Long Baseline Interferometry (VLBI). Few experiments have been carried out using inter-continental baselines and milliarc second resolutions have been achieved. Such measurements, due to their high resolutions, restrict attention to the compact cores of radio sources which are typically in the range  $0.1''$  to  $1.0''$ . Now the interplanetary scale sizes that cause IPS are such that resolutions obtainable by IPS are also between  $0.1''$  and  $1.0''$ . Thus until more VLBI measurements are available IPS can provide preliminary and important though, limited information on compact structures in radio sources. Our motivation in the present work was two-fold with the first being to study the angular sizes of all sources detectable by our telescope and to see if the measurements could yield the latitudinal variation of ISS in our Galaxy. The second motivation was essentially to analyze the long-term behaviour of the telescope so that future work involving studies of large-scale interplanetary transients by the method of g-maps (Gapper *et al.*, 1982) and V-maps (Kojima *et al.*, 1987) can be carried out using the enhanced  $20,0000 \text{ m}^2$  array at Thaltej and the three site network respectively.

The second part of the work exploited the IPS technique to infer the structure and properties of cometary ion tails at large distances downstream of the nucleus, typically greater than  $0.1 \text{ A.U.}$  The comets studied during this work were comet Halley in 1985 and comet Austin in 1990. Both sets

of data were obtained when the tail of the comet swept across a compact radio source thus providing a thin random phase-changing plasma screen during the passage of the source through the telescope beam. The work on Comet Austin was carried out with the 20,000 m<sup>2</sup> array while that of Comet Halley was done with the 10,000 m<sup>2</sup> array. The results of these observations were compared with those of Comet Wilson, obtained when its tail occulted two southern galaxies on May 1st and May 2nd 1987 (Slee *et al.* 1990).

The thesis is divided into six chapters and the first chapter contains an introduction to the solar wind and various aspects of diffraction phenomena used to study the interplanetary medium (IPM) and the interstellar medium (ISM). The importance of IPS as an efficient probe to study the IPM and ISM is brought out. The chapter also contains a brief historical perspective of comets and their importance in astronomy.

The second chapter introduces the relevant theory of IPS as applied to studies of the IPM. The salient features of the phenomenon are brought out along with its inherent advantages and drawbacks. Since a great deal of literature is available about the methodology and various aspects of IPS, this chapter aims at only providing an understanding of the physical processes at work concerning IPS during the course of the present observations so that the rest of the work to follow can be appreciated.

A work of this nature is based entirely upon the data obtained by a telescope, comprising the dipole array, the beam-forming network (Butler

matrix), the receiving system, and the data acquisition system. In the third chapter therefore a detailed description of each of the sub-systems is given.

IPS is a phenomenon which is similar to the familiar twinkling of star light, in the optical region, caused due to the Earth's neutral atmosphere. It is well known that the amount of scintillation caused by a compact radio source is a function of the angular size of the source and the solar elongation ( $\epsilon$ ). Thus for a given source size the scintillation index measured will vary with elongation in a well-known manner (Readhead *et al.*, 1978). Continued measurements of scintillation, in the direction of a radio source, caused due to the IPM along the line of sight can eventually be combined with scattering theory and proper calibration of the system to yield the source diameter. The author has measured the diameters of 14 different radio sources at 103 MHz, using data obtained between mid-1984 and end of 1987, and compared these results with other available measurements at 151.5 MHz and 81.5 MHz. These measured diameters were then used in conjunction with similar measurements at 151.5 MHz to calculate the amount of ISS as a function of galactic latitude at 103 MHz. The contribution of ISS to source broadening at 103 MHz was found to be  $0.07 \pm 0.01$  seconds of arc.

The principal problem with the above approach is that there is a bias towards choosing the strongest scintillators because it is for these sources that the diameters can be determined with the best accuracy. Unfortunately the strongest scintillators are the most compact sources and this selection effect could reduce the measured ISS effect especially when dealing with a

small sample of sources, as is the case using the  $10,000 \text{ m}^2$  array. In the fourth chapter the methodology and results obtained in this study are described.

Several groups of observers have made conflicting claims about the existence of enhanced IPS as the plasma tail of a comet passes in front of a compact radio source. It has been shown recently (Alurkar *et al.*, 1986; Slee *et al.*, 1990; Janardhan *et al.*, 1990a, 1990b) that cometary plasma can contain a higher level of turbulence than the normal solar wind and give rise to enhanced scintillations. The fifth chapter contains a detailed study of enhanced scintillations caused by the ion tails of two comets Viz. Comet Halley and Comet Austin. The observations were made during the occultation of two radio galaxies by the tails of the comets. A detailed spectral analysis of the data, after taking into account the effect of the tail-lag, has given new insights into the structure of cometary ion tails at distances greater than 0.1 A.U. downstream of the nucleus. It has been found that the scale sizes along and close to the comet axis are much finer than those close to the transition region where the tail merges with the solar wind. The rms electron density variation  $\Delta N$  has also been found to vary in the two regions with very high values being found along the axis, as compared to the normal solar wind at 1 A.U., and much lower values along the edge. Recent spacecraft data available indicates that a shock front had reached the Earth on the 18th December 1985, the date on which the maximum scintillation was observed during the observations of Comet Halley. This data has also been looked into and it has been found that the shock front could not account significantly to the observed enhancement.



The results have also been compared with those obtained at other frequencies for comets Halley and Wilson.

Since a large number of observational parameters like plasma velocities in the tail, magnetic fields and densities are as yet unavailable, a detailed hydrodynamic model of the observed scale sizes is not possible at this juncture. Spacecraft data are available close to the coma for different comets and these will be used to discuss the various possibilities for further work.

The sixth chapter very briefly describes the future scope and possibilities of exploiting the large dipole array at Thaltej together with the the three station network for long term studies of the IPM. A considerable amount of preliminary work has been carried out using the data obtained at the Thaltej telescope to study the solar wind velocity structure by making velocity maps or "V- Maps" by a method proposed by (Kojima *et al.*, 1987). The solar wind velocities were calculated using single station data by the method of Fresnel knee fitting (Manoharan and Ananthakrishnan, 1990). These maps are essentially made by tracing a large number of measured velocities back on to the source surface close to the sun. Preliminary work towards studying the IPM by making "g - Maps" has also been carried out according to the method of (Tappin *et al.*, 1983). In this method, rather than just mapping the scintillation index  $m$ , the long term trends in the average scintillating flux are mapped by measuring an enhancement factor  $g = \frac{\Delta S(\epsilon)}{\langle \Delta S(\epsilon) \rangle}$  for a large number of scintillating sources - typically 1000 to 1500. When these  $g$  values are plotted as seen on the sky, large-scale

transient disturbances can be seen from day-to-day changes in the g-maps.. Since transient disturbances are three dimensional and we see only the projection of these on the sky, it is necessary to fit models to the observations. The work mentioned above has not been included as a part of the present thesis as it is still an on-going project, but when the scintillation data on a very large number of sources become available, the results of the scattering studies carried out using 14 radio sources can be further verified. The ability to see a large number of faint sources will also enhance the possibilities of observing many more cometary occultations at Thaltej. It is hoped that simultaneous three station observations of cometary occultations can also be carried out using the three station network. This can lead to an accurate determination of the plasma velocity field in cometary tails at various distances downstream of the nucleus and hence help in modelling the structure and dynamics of the plasma content of comet tails.

# Chapter - I

## INTRODUCTION

Radio scintillation is a diffraction phenomenon in which coherent electromagnetic radiation, from a distant radio source, passes through a turbulent refracting medium and suffers scattering. This results in random temporal variations of the signal intensity (scintillation) at a distant point of observation. The most familiar example of scintillation is the twinkling of starlight caused by turbulence in the earth's neutral atmosphere. Radio scintillation, the phenomenon exploited for the work in this thesis, is caused by random refractive index variations in one of the regions of the earth's vast plasma environment viz. the interplanetary medium (IPM). Radio scintillation can also be caused by the ionosphere and the interstellar medium, the two other regions of the earth's plasma environment. Since the theory behind it is well understood, the phenomenon can be used as a tool to infer the properties of both the radio sources themselves and the turbulent intervening medium along the line

of sight to the source. In this thesis scintillation caused by the plasma content of the IPM has been used to infer the source size structure of a number of compact radio sources. This has then been used, as we shall see in Chapter four, to study the contribution of interstellar scattering (ISS) towards source broadening at our operational wavelength of 2.91 m.

Figure 1.1 is a pictorial representation of the phenomenon of IPS for a typical observation. Coherent electromagnetic radiation from a distant radio source is shown encountering interplanetary plasma. This plasma which is continuously streaming radially outwards from the Sun in all directions, contains density irregularities which can diffract the incoming radiation (plane waves). The plane waves on emerging from the plasma medium are seen to be phase-modulated. These phase modulations then, by mutual interference, develop on passage through interplanetary space into amplitude variations which sweep past the observer on the earth and can be detected by a radio telescope as fluctuations in the observed flux density of the source. A more detailed description of the IPS theory will be taken up in the next chapter.

The IPS methodology has, in recent times, been used to study the plasma content of cometary ion tails too. In such studies the tail of the comet is assumed to provide the turbulent refracting medium which presumably causes scintillation. This occurs when the comet tail sweeps across a compact radio source during the time when the source is passing through the telescope beam. Since the radio telescope at Thaltej, which was used for the observations presented in this thesis, is a transit

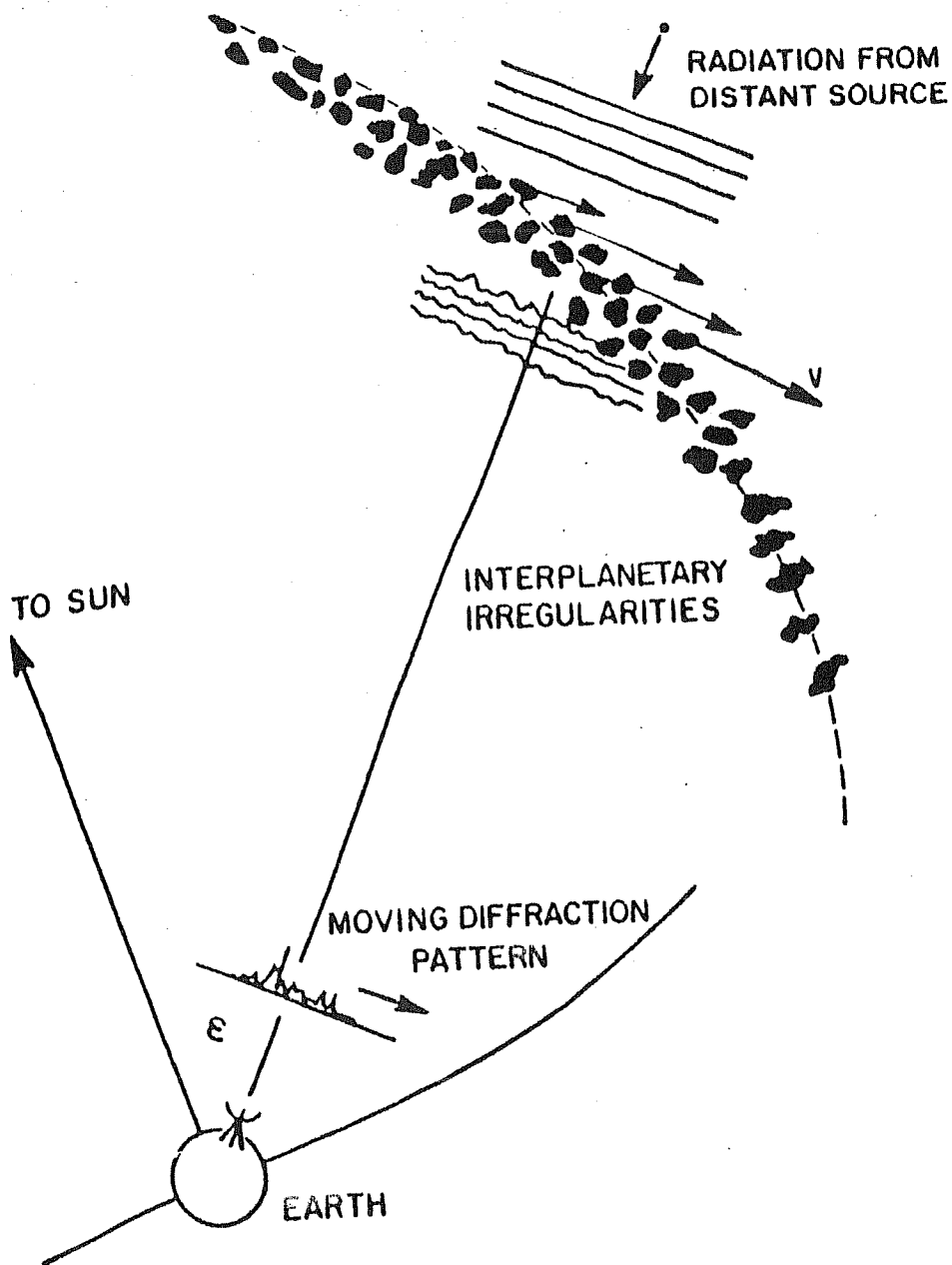


**Figure 1.1** Pictorial representation of the phenomenon of interplanetary scintillation (IPS) for a typical observation.

instrument capable of observing sources only at meridian transit, it is easy to understand that such events do not occur often. But when they do they can provide interesting insights into the structure and dynamics of cometary ion tails. In the latter half of this thesis the results of two sets of observations of Comet Halley and Comet Austin (1989 c1) are presented. However, before really going into the theory underlying IPS and the work carried out, a very brief review of some of the facts that make radio astronomy possible, the salient properties and features of the IPM, ISS and comets, as we understand them today is necessary. In the rest of this Chapter therefore, an attempt has been made to set these in perspective so that the work to follow can be fully appreciated.

## 1.1 The Visible and Radio Windows.

The development of radio astronomy has seen, over the years, an interplay between studies of radio sources (radio galaxies, quasars and pulsars) and the manner in which radiation from these sources is scattered by the ionosphere, the IPM and the interstellar medium along the line of sight. Since we are buried under nearly 500 km of atmosphere, photons cannot easily reach down to the earth's surface. It would thus be interesting to ask how one can study the effects of an intervening medium upon electromagnetic (E.M.) radiation emanating from compact radio sources. In other words, how are we able to "see" radiation whose energy falls in the radio band corresponding to a wavelength range of approximately 1 mm to 100 m ?

Basically, the sort of particle interaction that a photon undergoes, on passage through the atmosphere, is dependent upon the energy of the incoming photons. For photons having an energy greater than 1 MeV the dominant process according to the laws of quantum mechanics, will be annihilation of the photons into electron-positron pairs. For photons with energy in the range 50 KeV to 1 MeV, the dominant process will be Compton scattering off electrons in atoms. The photon may Compton-scatter several times until it drops to an energy of  $\leq 50$  KeV. At this stage, the probability of photoelectric ionization is very high and the photon annihilates leaving behind an electron and an ion and hence an ionosphere.

For photons lying in the energy range 1.7 eV to 3 eV, though, a small miracle takes place. The gap between the ground state energy levels of atoms and the point where the electrons will be free is more than 3 eV. Photons with energies less than 3 eV cannot therefore ionize atoms and so pass through the atmosphere undisturbed. Thus the region lying between 1.7 eV and 3 eV or 7200 Å and 4000 Å is called an energy window or the visible window. Below 1.7 eV and down to about  $10^{-3}$  eV the window is only partially open because the small molecular binding energies take over the annihilation. Between  $10^{-3}$  eV and  $10^{-8}$  eV, corresponding to wavelengths between 1 mm and 100 m, photons can again pass undisturbed through the atmosphere. This is called the radio window and its existence enables us to detect radiation from distant radio sources and hence makes radio astronomy possible.

## 1.2 The Interplanetary Medium.

Interplanetary space is completely filled with a tenuous and almost fully ionized gas which streams radially outwards from the sun at supersonic speeds. This material is known as the solar wind and its existence was first inferred from the motion of comet tails (Biermann, 1951), by the continued presence of aurora in terrestrial auroral zones and by the appearance of zodiacal light. Recent methods, though, involve the use of radio techniques such as interplanetary scintillation (IPS) and space probes to study and sample the solar wind.

The most successful theoretical model of the solar wind was proposed by (Parker, 1958 a, b) who showed that there was no hydrostatic equilibrium solution for coronal gas, with vanishing pressure at infinity. He showed that a high coronal temperature of about  $\sim 10^6$  °K was needed and this would result in a continuous supersonic expansion of the corona as the solar wind. In this model the solar wind close to the sun ( $\leq 0.2$  AU) undergoes acceleration, after which it attains a constant velocity. Observations show that this velocity can lie in the range between  $350 \text{ km sec}^{-1}$  and  $900 \text{ km sec}^{-1}$  with normal velocities, between  $300 \text{ km sec}^{-1}$  and  $400 \text{ km sec}^{-1}$ , being observed when quiet or undisturbed conditions exist. The solar wind in such a "quiet" or undisturbed state is referred to as the 'quiet solar wind'. In this thesis all observations refer to the quiet solar wind, unless otherwise stated.



The density of the solar wind varies approximately as  $r^{-2}$  and is found to have a value at about 1 AU of  $N_p = N_e \sim 10 \text{ cm}^{-3}$ , with an associated rms variation of about 1%. Due to these very low densities, as is the case in most space plasmas, the conductivity is very high. Thus if any large field gradients exist, the high conductivity permits charge to move to areas of lower field and cancel the gradient. The magnetic field of the sun, which is embedded in the solar plasma and along whose field lines charged particles spiral outwards, is thus frozen into the plasma and corotates with the sun giving it the form of an Archimedian spiral. Studies of the interplanetary magnetic field (IMF) have revealed (Smith, 1964; Davis *et al.*, 1966) a general agreement of observations with the Archimedian spiral model (Parker, 1963). A radial and transverse gradient to the interplanetary magnetic field has also been detected (Burlaga and Ness, 1968). While the radial component, which has a value at the earth of about  $3 \times 10^{-5}$  Gauss, is also found to vary as  $r^{-2}$  the transverse component varies as  $r^{-1}$  and has a value at the earth of about  $4 \times 10^{-5}$  Gauss. These measurements were made by Pioneer 6 between 0.81 AU and 0.98 AU from the sun and are found to be consistent with Parker's model (See Fig. 1 Burlaga and Ness 1968) which predicts the variations in the radial and transverse components of the IMF as in the foregoing discussion. It was discovered (Wilcox and Ness, 1965) that the magnetic field reverses polarity as the sun rotated, indicating an azimuthal magnetic field sector structure near the equatorial plane at 1 AU. Later it was noted (Rosenberg and Coleman, Jr., 1970; Schulz, 1973) that these observations could also be explained by a three dimensional field structure, in which the interplanetary field was divided into a North and South polar field separated by an inclined,

neutral current sheet extending far into the outer heliosphere. In each sector the magnetic field polarity remains unchanged, with sharp reversals from sector to sector. Experimental proof of this came from measurements of Pioneer 11 (Smith *et al.*, 1978). It has also been observed at the earth (Wilcox and Colburn, 1970) recurring with a period of 27 days, the synodic rotation period of the sun. These are typically long-lived structures and could last for as many as 12 solar rotations. Table 1.1 summarizes some relevant properties of the solar wind.

The scale sizes in the solar wind show a very large range and the larger scale sizes, typically greater than  $10^4$  km are seen to follow a power-law spectrum (Intriligator and Wolfe, 1970). As will be seen in the next Chapter, IPS observations are sensitive only to scale sizes of less than about 1000 km, but satellite observations show variations on length scales from  $10^2$  km to  $10^7$  km. Structures larger than  $10^7$  km also occur but these are due to stream structure in the solar wind and are not a part of the turbulence spectrum. The form of the spectrum for finer scales according to a few authors (Jokipii and Hollweg 1970; Lovelace *et al.*, 1970; Cronyn, 1970) is determined by extrapolating the power-law spectrum down to finer scales and by yet others (Hewish, 1971; Little, 1971; Buckley, 1971; Matheson and Little, 1971; Rickett, 1973) assuming a Gaussian spectrum with a unique scale size for the finer scales and a power-law spectrum for scales  $\geq 10^4$  km. Spacecraft observations when compared with ground-based data show (Neugebauer, 1975; Unti and Russell, 1976) that there is a marked flattening of the spectrum at spatial frequencies corresponding to scale lengths of about 200 km. The scintillation index (rms/mean source flux) has been

**Table - 1.1:      SOME RELEVANT PROPERTIES OF THE SOLAR-  
WIND**

PROPERTY	DISTANCE	
	0.1 AU	1.0 AU
$N_e \text{ cm}^{-3}$	1000	10
$\Delta N_e \text{ cm}^{-3}$	40	0.1
$v \text{ km sec}^{-1}$	400	400
$v_{\text{Alfvén}} \text{ km sec}^{-1}$	500	50
B Gauss	$10^{-2}$	$10^{-4}$
$T_e \text{ }^\circ\text{K}$	$10^5$	$10^5$
$\nu_{\text{Plasma}} \text{ MHz.}$	0.1	0.01
$\nu_{\text{Scint.}} \text{ Hz.}$	$\sim 10$	0.5

found to be proportional to the wavelength ( $\lambda$ ) and to explain this wavelength dependence it is necessary to adopt a spectrum which is considerably flatter than the extrapolated spacecraft spectrum at temporal frequencies below about 1 Hz. It has also been shown (Readhead *et al.*, 1978) that a simple Gaussian model of the wavenumber spectrum of electron density fluctuations in the range  $5 \times 10^{-3} < k < 3 \times 10^{-1} \text{ km}^{-1}$ , where  $k = \frac{2\pi}{\lambda}$ ; can explain a broad variety of IPS observations while a simple power-law model exhibits serious inconsistencies (see Table 2: Readhead *et al.*, 1978). Combined with the fact that the IPS technique is insensitive to large-scale structure it seems that the single-scale-size Gaussian model is a better approximation to the true spectrum for IPS studies than is a power-law model. In this thesis therefore the form of the irregularity spectrum will be taken to be a Gaussian.

### 1.3 IPS As a Probe to the Interplanetary and Interstellar Media.

The earliest studies (Smith, 1950; Little and Lovell, 1950) led to the identification of the ionosphere as the cause of fluctuations in the intensity of radio signals from galactic radio sources. Hewish (1975) has shown how his early studies led to ionospheric scintillation, then to angular scattering in the outer corona of the sun, and finally to IPS. The fact that only very small diameter radio sources could show IPS was then turned around and IPS was used as a probe to determine radio source size

structure in the range 0.1 to 2.0 arc seconds at meter wavelengths. The angular diameters of a large number of radio sources have been determined by this technique (Cohen *et al.*, 1967; Little and Hewish, 1968; Bhandari *et al.*, 1974; Duffett-Smith, 1976). IPS also provides a powerful technique for probing the irregular structure of the interplanetary electron density by measuring the angular scattering and intensity scintillations of radio sources (Hewish, 1955; Hewish and Wyndham, 1963; Erickson, 1964; Hewish, Scott and Wills, 1964; Okoye and Hewish, 1967; Hewish and Symonds, 1969). Further the method can be used to study the interstellar medium via the intensity scintillation of pulsars. The extreme regularity of the pulse period contrasts with the erratic variations in the intensities, and the slow component of these intensity variations was identified (Scheuer, 1968; Rickett, 1969, 1977) as interstellar scattering (ISS). An important consequence of ISS is that small diameter radio sources appear broadened. Thus at a given wavelength this effect can set a limit to high resolution radio studies due to a limit being set on the minimum diameter of radio sources. At meter wavelengths this broadening amounts to about 0.1 second of arc and the distribution of angular scattering in our galaxy (Readhead and Hewish, 1972) by measuring the angular diameters of a number of radio sources by the IPS technique is one of the aims of the present work.

The main advantages of the IPS method are that high resolution between 0.1 and 2.0 arc seconds, is obtainable. To achieve similar resolutions by interferometry would require baselines between  $\sim 500$  km and 10,000 km at meter wavelengths. Using this method, the IPM can be

sampled at all helio latitudes as compared to spacecraft which so far have been confined to the ecliptic. Also spacecraft measurements are essentially high precision local measurements of the IPM in the ecliptic while IPS observations measure its large scale features. This is due to the fact that the measured quantities are obtained as an integrated effect all along the line of sight to the source. It is clear however that for any sort of modelling study, it is the large scale features that are needed, and IPS is the only observational method available that can provide this. The method is also fast and cheap. The principal drawback, though, is that the structural information about the source is very limited in that it can give only information regarding the angular diameter of the source in the range 0.1 to 2 seconds of arc.

#### **1.4 Comets - Their Origin and Relevance to Astronomy.**

Comets, due in part to their small masses, have undergone virtually no internal evolution and very little external evolution during their approximately 5 billion year history. Comets thus represent the purest samples of the primordial solar nebula and can provide tantalizing clues to the early history of the solar system. The study of comets is thus a very important part of astronomy. Opportunities to observe bright comets ( $V \leq 5$  mag.) close to the earth ( $\leq 1$  AU) arise only rarely, typically every few years and have been observed out to 12 AU from the sun and as close as 0.02 AU. Their periods of revolution have been conventionally classified as short period ( $P \leq 200$  years) and long period ( $P \geq 200$  years).

Comets are also classified as "Old" and "New" depending upon the number of solar passages, as a greater number of these would imply a greater degree of evolution. This classification though is based entirely upon orbital characteristics rather than observational evidences.

Oort (1950) showed that a plot of number of comets versus  $\frac{1}{a}$ , the inverse of the semi-major axis of the comet orbit, for 19 comets, gave a conspicuous peak around  $\frac{1}{a} \sim 10^{-5} (\text{AU})^{-1}$ . It was shown that this peak could not be due to chance. Oort called comets belonging to this peak as "new" comets, or in other words those which have come into the solar-system for the first time. The inclination of the orbits of these comets was found to be randomly distributed in accordance with observations of long period comets. All this appears to show the existence of a vast cloud of comets, called the Oort cloud, situated at the periphery of the solar-system at approximately  $10^5$  AU from the sun. The long period comets are believed to originate from this cloud and enter the solar system due to stellar perturbations. A small fraction of the comets which enter the solar-system, in their encounter with the large planets (notably Jupiter), are perturbed violently enough to leave the solar-system after their first encounter. Some remain in the solar-system and are seen as long period comets. Repeated encounters with giant planets cause some of them to be transformed into intermediate and short period comets.

### 1.4.1 Present Day Concepts.

Our present conception of a comet is based on the icy conglomerate model proposed by (Whipple 1950; 1951). According to this model the nucleus is a fragile ice-dust mixture of diameter 0.1 km to 10 km. Images of comet Halley taken by the camera on board the Giotto spacecraft in March 1986 have shown (Keller *et al.*, 1987) that the nucleus had typical dimensions of  $8.2 \text{ km} \times 8.5 \text{ km} \times 16 \text{ km}$  and a surface area of  $400 \text{ km}^2$ . As this so called dirty snowball, in its orbit around the sun, approaches perihelion its surface is subjected to a variety of erosive processes, the most prolonged of these being cosmic rays, solar wind ions and surface photo-electron currents. At distances, from the sun, of about 3 AU, volatiles sublime from the surface due to solar radiation from an expanding envelope of dust and gas called the coma. The formation of a tail may or may not follow this stage. Cometary tails too are classified into Type-I or Type -II tails. The Type-II tail is made up of dust which was formerly embedded in the nucleus and released as the surface ices vaporize in the solar radiation field. The Type-I plasma or ion tail is formed by the interaction of ions in the coma with the solar wind magnetic field which folds onto the comet ionosphere and is presumed to accelerate ions from the coma in the anti-solar direction to form the plasma tail (Alfvén, 1957).

### 1.4.2 Optical and IPS Observations Of Comets.

Most of the observations of comets, principally their comae,



over the past century have been devoted to optical spectroscopy in the band 3000 Å to 8000 Å. This has led to the identification of a large number of atomic and molecular emission features which appear at distances  $\leq 3$  AU. Over the last decade however, improved detectors, observations in ultraviolet (UV) together with radio and satellite studies have significantly increased the number of identified species. A list of atomic and molecular species can be found in Table 1 of "Comets" (Edited by L.L. Wilkening - Univ. of Arizona Press ). Nearly all photographic studies of comets have been done on blue sensitive emulsions in the band 3500 Å to 5000 Å and since  $\text{CO}^+$  emission is known to dominate this band, the distribution of  $\text{CO}^+$  ions in comet tails is well studied. The photographs also show up a vast variety of forms, structures, condensations and inhomogeneities (Rahe *et al.*, 1969). These structures in the form of knots, kinks, and helices distort the tail and vary in brightness as they move outwards along the tail on time scales of hours (Jockers *et al.*, 1972; Brandt and Mendis 1979; Brandt *et al.*, 1980). The velocities inferred from these motions range from 20 to 250 km sec<sup>-1</sup> but it is not yet known if these observed motions represent hydrodynamic waves propagating down the tail (Alfvén, 1957; Ness and Donn, 1965), or mass motions of cometary ions (Brandt and Mendis, 1979). The axis of the plasma tail has also been observed to lag the comet's orbital radius vector. This tail-lag which can be as much as  $\sim 5^\circ$  (Belton and Brandt, 1966) is caused by the interaction of the radially directed solar wind with the comets velocity. Whether or not the plasma tail lies in the comet's orbital plane is yet to be established.

In the latter half of this thesis, the observations of two comets viz.

Comet Halley and Comet Austin have been discussed. The observations exploited the phenomenon of IPS to probe the plasma tail of the comets at distances greater than 0.1 AU downstream of the nucleus. In this study the tail of the comet provided the thin, random phase-changing screen while a compact radio source provided the coherent illumination during the time when the tail swept in front of it. The tail-lag and plasma velocities play, as we shall see in Chapter 5, a crucial role in the analysis and interpretation of the data and since plasma velocities, as seen in the foregoing discussion, are not known accurately the interpretation of the data is uncertain to a large extent. Nevertheless IPS studies of cometary plasma tails (Alurkar *et al.*, 1986; Slee *et al.*, 1987, 1990; Janardhan *et al.*, 1991a,b) have provided very interesting insights into the structure and dynamics of cometary ion tails.

## 1.5 Summary.

The work presented in this thesis is essentially divided into two parts. The first part concerns studies of compact radio source size structure using IPS and related studies of ISS at 103 MHz. The second part describes the use of the IPS technique to study the plasma contained in the cometary ion tails. The entire work was carried out using the large filled-aperture dipole array at Thaltej, Ahmedabad. This telescope, operating at 103 MHz, is one of a network of three similar spaced telescopes of the Radio Astronomy Group at the Physical Research Laboratory and is used to study the interplanetary medium (IPM) by the method of IPS. Since it began operating in mid-1984, a large amount of data has been gathered and since

then the physical area of the telescope has been enhanced from 5,000 m<sup>2</sup> in early 1984 to 10,000 m<sup>2</sup> in 1985 and finally 20,000 m<sup>2</sup> in 1990. A detailed explanation of the antenna array and associated instrumentation used for the work presented in this thesis will be taken up in Chapter three.

The long term aims of the network are essentially to study the solar wind velocity structure by making V - Maps by the method of (Kojima *et al.*, 1987), using the 3 stations simultaneously and to study large-scale interplanetary transients by the method of g - Maps according to (Gapper *et al.*, 1982), using the single large telescope at Thaltej. The velocity maps are made by tracing a large number of measured velocities back to the source surface near the sun, while in the method of g - Maps, rather than just mapping the scintillation index (rms/mean source flux), day-to-day variations in the scintillating flux from the long-term trends in the average scintillation indices are mapped by measuring an enhancement factor  $g$  given by  $g = \frac{\Delta S(\epsilon)}{\langle \Delta S(\epsilon) \rangle}$ ; where  $\Delta S(\epsilon)$  is the scintillating flux at a given elongation, for a large number of scintillating sources -typically 600 to 1000. When these  $g$  values are plotted as seen on the sky, large-scale transient disturbances can be easily identified and their movement studied, from the day-to-day changes in the  $g$ -maps.

Small components in radio sources may be measured by high resolution techniques other than IPS, the most important method being Very Long Baseline Interferometry (VLBI), which is impractical at meter wavelengths. Few experiments have been carried out using inter-

continental baselines and milliarc second resolutions have been achieved. Such measurements, due to their high resolutions, restrict attention to the compact cores of radio sources which are typically in the range 0.1 to 1.0 seconds of arc. Now, the interplanetary scale sizes that cause IPS are such that resolutions obtainable by IPS are also between 0.1 and 1.0 arc seconds. Thus, until more VLBI measurements are available, IPS can provide preliminary and limited information on compact structures in radio sources. Our motivation in the present work was thus two-fold with the first being to study the angular sizes of all scintillating sources detected by our telescope and to see if the measurements could yield the latitudinal variation of ISS in our Galaxy. The second motivation was essentially to analyze the long-term behavior of the telescope so that future work involving studies of large-scale interplanetary transients by the method of g-maps and V-maps can be carried out.

The motivation to take up the second part of the work presented in this thesis was the question - can cometary plasma contain a higher level of turbulence than the normal solar wind and give rise to IPS and whether there are any special circumstances under which such scintillations can be observed? Comet Halley which appeared in Dec.1985 and Comet Austin in May 1990 were both studied and spectral analysis of the scintillation data obtained has thrown light upon the scale sizes and rms electron density deviations  $\Delta N$  in the tail more than 0.1 AU downstream of the nucleus. The study has also brought out the importance of the occulting geometry and the tail-lag in carrying out such observations. The work and results obtained from this study have been described in detail in the fifth Chapter.

# Chapter - II

## INTERPLANETARY SCINTILLATION AND RELEVANT THEORY

### 2.1 Introduction.

Scintillation, both optical and radio, is of interest to observational astronomy. While optical scintillation can be exploited to gain information about the earth's neutral atmosphere, radio scintillation can be used to study the ionosphere, the interplanetary medium (IPM), the interstellar medium and the source of electromagnetic radiation itself. Both optical and radio scintillation share a common set of characteristics and can be explained by a single theory. Extensive and rigorous treatment of the theory underlying radio star and satellite scintillation can be found in several papers (Ratcliffe, 1956; Booker, 1958; Chernov, 1960; Tatarski, 1961; Salpeter, 1967; Readhead, 1971; Marians, 1975 a, b; Rumsey, 1975).

In understanding the phenomenon of scintillation one has to deal with the propagation of a radio wave through a region containing irregularities in electron density and hence in refractive index. There are several ways of doing this, the most direct and rigorous being to treat the problem as one of scattering. Here the wave at the receiver is regarded as the sum of the original wave and waves scattered from each element of volume of the irregularity medium. This method becomes difficult to apply when the scattering is strong or in other words when multiple scattering prevails. Yet another method uses diffraction theory wherein the properties of the wavefront, on emergence from the scattering medium, are first related to the properties of the irregularities themselves. Subsequent propagation through free space beyond the medium is then treated as a diffraction problem. Generally it is found that absorption in the irregular medium is negligible and the medium can be treated as a thin layer of thickness  $L$  with  $L \ll z$  where  $z$  is the distance between the observer and the screen. The wavefront that emerges from the thin screen is modulated in phase only and the rms phase deviation ( $\phi_{rms}$ ) across the wavefront can be calculated in terms of the typical scale size  $a$  of the density irregularities in the medium, the thickness of the screen and the rms variation in electron density  $\Delta N$ . The assumption of a thin 'phase-changing screen' is valid because the scattering power  $\beta(r)$  is proportional to  $r^{-4}$  (Readhead, Kemp and Hewish, 1978) and therefore for small solar elongations ( $\epsilon$ ) the dominant contribution to the scattering will occur at a point on the line of sight that is closest to the sun. This is known as the thin-screen approximation (Salpeter, 1967) and is valid in the weak scattering regime when the total imposed phase deviation  $\phi$  is  $\ll 1$  rad. For

large solar elongations ( $\epsilon$ ) this approximation breaks down as the earth becomes embedded in the scattering region. In other words, the scattering region is thick and diffraction can start within the region itself. The emerging wavefront will be modulated in both amplitude and phase. Both approaches give identical results, if properly applied, within the range of validity of each. Figure 2.1 is a representation of the IPS geometry for the thin screen approximation. The thin phase-changing screen is assumed to stretch in the  $x$  direction, being negligibly thin compared to the distance  $z$  and containing density irregularities of characteristic scale size  $a$ . The scattering power  $\beta(r)$  is also shown for small elongations.

In the rest of the chapter the important aspects of IPS theory will be discussed with an aim to gain an insight into the physical processes at work during IPS observations.

## 2.2 Arcsecond Resolution.

It was mentioned in the previous chapter that with the IPS technique one can obtain resolutions in the range 0.1 to 2.0 seconds of arc. It is known that arc second resolution requires information on spatial coherence of the source radiation over a million wavelengths and it is difficult to imagine how IPS, a phenomenon most pronounced at meter wavelengths, provides this. In the case of IPS, radiation becomes deflected by the scattering medium by an angle given by  $\text{Sin } \theta = \frac{\lambda}{a}$ , which for small  $\theta$

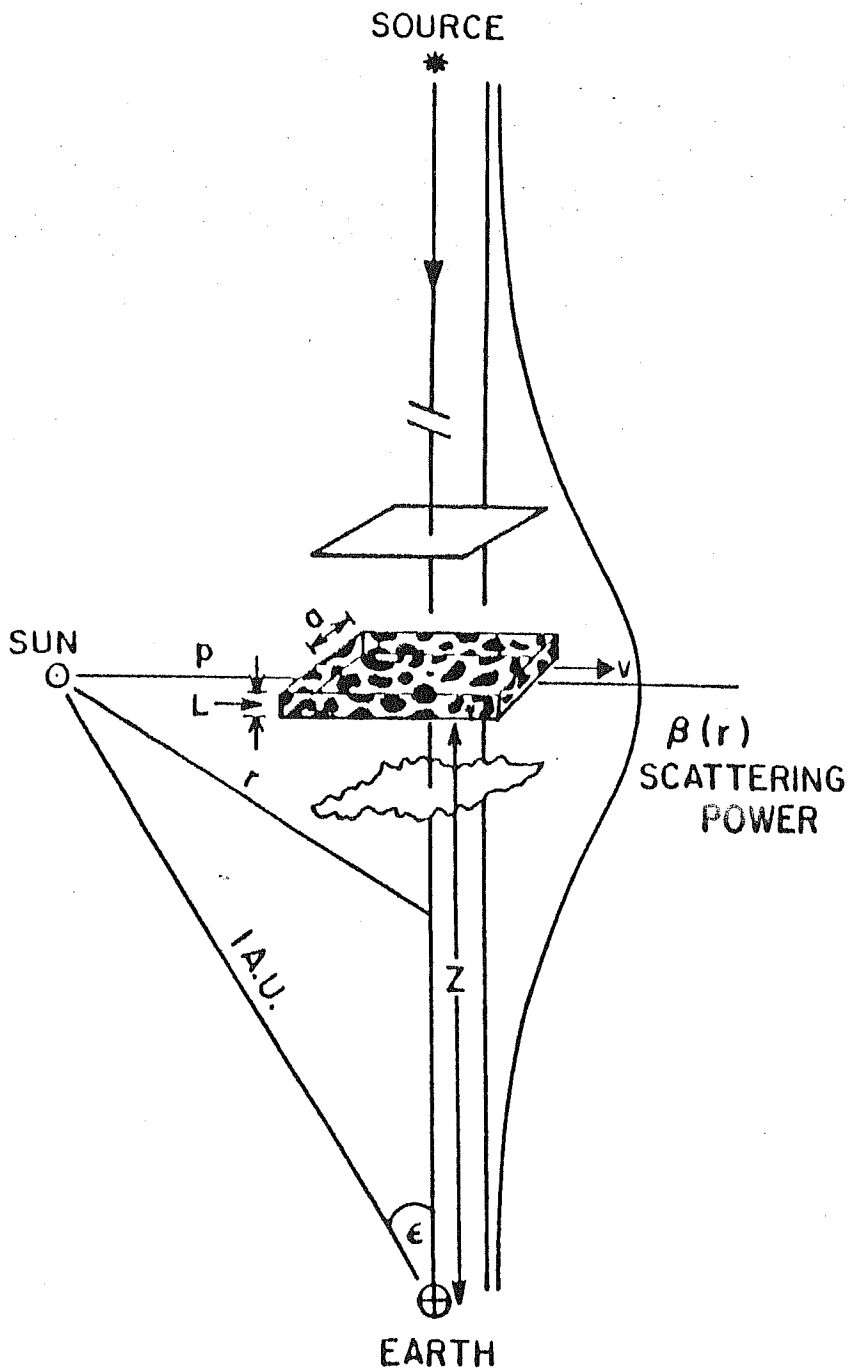


Figure 2.1

Shows the typical IPS geometry for the thin screen approximation. Also shown is the scattering power  $\beta(r)$ . The density irregularities of size  $(a)$  are confined to a thin slab of thickness  $(L)$ , extending in the  $x$ -direction and moving with a velocity  $(v)$ .



(as is the case in IPS) is equal to  $\frac{\lambda}{a}$ ; where  $\lambda$  is the wavelength and  $a$  is the scale size of density irregularities. This means that at a distance  $z$  from the scattering medium (thin screen), it is possible to collect radiation that has been incident over an extent  $D$  of the plasma where  $D = \frac{z\lambda}{a}$ . Thus, a resolution of  $\theta \approx \frac{\lambda}{D}$  or  $\frac{a}{z}$  is provided. This in fact is just the angle subtended by a typical irregularity in the screen on the earth, a quantity which is of the order of 1 arc second. If  $a$  is taken to be 100 km and  $z$  to be half an AU then the quantity  $\frac{a}{z}$  works out to be about 1.0 second of arc.

### 2.3 Phase Modulation of a plane Wave Due to the IPM.

Consider the case of a plane wavefront passing through a thin slab of density irregularities of thickness ( $L$ ) at a distance ( $z$ ) from the earth as depicted in Figure 2.1. To further simplify the problem we also assume that the electron density varies only in the plane of the diagram and not in a direction perpendicular to it. On emerging from the thin slab of density irregularities the formerly plane wave will have random perturbations imposed on it. These perturbations will be of phase only and can be calculated by integration through the medium along straight line paths.

The refractive index of a fully ionized gas, such as is present in interplanetary space, depends upon the electron density ( $N$ ) and the wave

frequency  $\left(f = \frac{\omega}{2\pi}\right)$ . In its simplest form, ignoring collisions and the earth's magnetic field the refractive index is given by the expression:

$$n = \left[ 1 - \frac{N e^2}{\epsilon_0 m_e \omega^2} \right]^{\frac{1}{2}}$$

Where:

$m_e$  = electron mass

$e$  = electron charge

$N$  = electron density

$\epsilon_0$  = permittivity

$\omega$  = angular frequency =  $2 \pi f$

To the first order this can be written as :

$$n \simeq \left[ 1 - \frac{1}{2} \frac{N e^2}{\epsilon_0 m_e \omega^2} \right]$$

$$n \simeq \left[ 1 - \frac{1}{2} \frac{N e^2 \lambda^2}{4 \pi^2 \epsilon_0 m_e c^2} \right]$$

$$\simeq \left[ 1 - \frac{1}{2} \frac{N r_e \lambda^2}{\pi} \right]$$

where :

$$r_e = \frac{e^2}{4 \pi \epsilon_0 m_e c^2} \quad \text{is the classical electron radius.}$$

Now if there is a fluctuation of electron density of magnitude  $\Delta N$  about the mean then the associated fluctuation in refractive index would be :

$$\Delta n = - \frac{1}{2} \frac{\lambda^2 r_e}{\pi} \Delta N$$

The phase on emergence of the wavefront at any point  $x$ , at the bottom of the screen, relative to what it would have been in the absence of the medium is given by :

$$\phi(x) = - \frac{2\pi}{\lambda} \int \Delta n \, dz$$

$$\phi(x) = - \frac{2\pi}{\lambda} \int \frac{\lambda^2 r_e}{2\pi} \Delta N \, dz$$

$$\phi(x) = - \lambda r_e \int \Delta N \, dz$$

The result of the above integration will be:

$$\phi_{rms} = \pi^{\frac{1}{4}} \lambda r_e (aL)^{\frac{1}{2}} \left[ \langle \Delta N^2 \rangle \right]^{\frac{1}{2}}$$

(2.1)

The significant factors in this equation have a simple physical interpretation. The phase deviation introduced by a single irregularity is given by :

$$\phi = \frac{2\pi}{\lambda} (\text{optical path})$$

$$\phi = \frac{2\pi}{\lambda} (\Delta n a)$$

$$\phi = -\lambda r_e a \Delta N$$

In a distance  $L$  there are  $\left(\frac{L}{a}\right)$  such irregularities, but since the process is random we multiply by the number that are effective, giving

$$\phi = -\lambda r_e a \left(\frac{L}{a}\right)^{\frac{1}{2}} \Delta N$$

$$\phi_{\text{rms}} = \lambda r_e (aL)^{\frac{1}{2}} \left[ \langle \Delta N^2 \rangle \right]^{\frac{1}{2}}$$

We see that except for the constant factor  $(\pi)^{\frac{1}{4}}$  we can account for the other terms.

## 2.4 The Fresnel Filter.

Consider a plane wave incident on a thin slab of density irregularities, having a cosinusoidal variation in the  $x$  direction only as shown in Figure 2.2a. This assumption is valid because a realistic screen, varying in an arbitrary fashion, can be Fourier decomposed into its components and then each component can be treated separately summing finally to get the total effect. The cosinusoidal variation would imply that

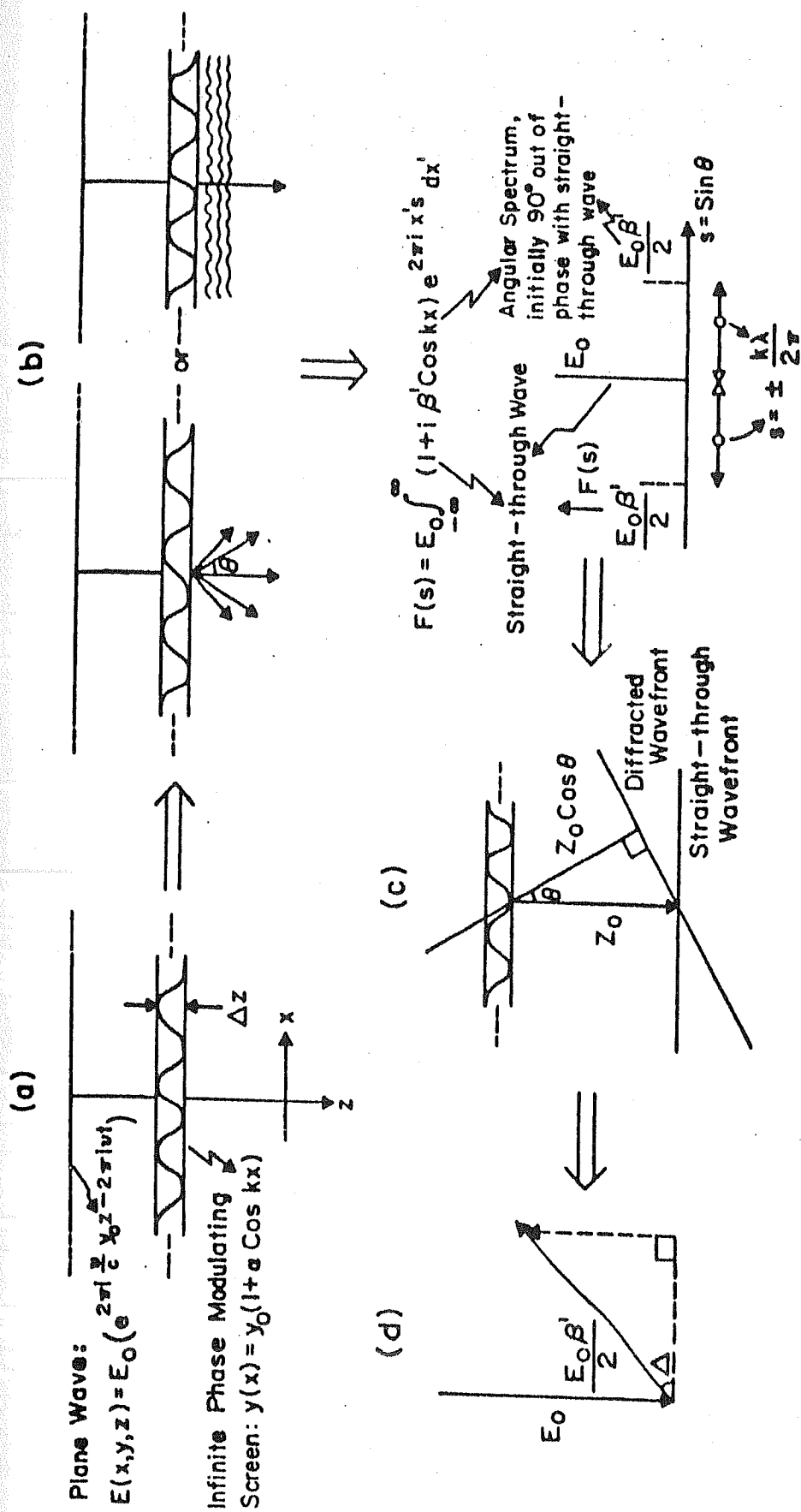


Figure 2.2a - 2.2d Depicts the development of an angular spectrum of waves when a plane wave travels through a phase modulating screen extending in the x-direction (a). The angular spectrum of waves (b), by mutual interference (c) produce intensity variations (d).

$y(x) = y_o (1 + \alpha \cos kx)$  where  $k = \frac{2\pi}{a}$  and  $a$  is the scale-size of the irregularities. The initial plane wave can be represented by :

$$E(x, y, z) = E_o \left( e^{2\pi i \frac{v}{c} y_o z - 2\pi i \nu t} \right)$$

On emerging from the thin screen of density irregularities at  $z = \Delta z$  we have :

$$E(x, y, \Delta z) = E_o \left( e^{2\pi i \frac{v}{c} y(x) \Delta z - 2\pi i \nu t} \right)$$

$$E(x, y, \Delta z) = E_o \left( e^{2\pi i \frac{v}{c} y_o \Delta z + i \beta' \cos kx - 2\pi i \nu t} \right)$$

Where :

$$\beta' = 2\pi \frac{v}{c} \alpha y_o \Delta z$$

Thus on emerging from the thin slab of irregularities, the previously plane wavefront now has a complex amplitude imposed on it. It is well known that complex amplitude and angular spectrum are Fourier transform pairs (see Ratcliffe, 1956). In other words

$$F(s) = \int_{-\infty}^{\infty} e^{i \beta' \cos kx} e^{-2\pi i x' s} dx'$$

Where :

$$x' = \frac{x}{\lambda}$$

$$s = \sin \theta = \frac{k\lambda}{2\pi} = \frac{\lambda}{a}$$

It is to be noted that the Fourier relation is between  $x'$  and  $s$  and not  $x$  and  $\theta$ . In the weak scattering case when the rms phase deviation imposed on the wave  $\Delta\phi \ll 1$  rad,  $e^{i\beta' \cos kx} \simeq (1 + i\beta' \cos kx)$ , since  $\beta' \ll 1$ .

$$F(s) = E_0 \int_{-\infty}^{\infty} (1 + i\beta' \cos kx) e^{-2\pi i x' s} dx'$$

In other words  $F(s)$  represents a spectrum of plane waves, each travelling at an angle  $\theta = \sin^{-1}(s)$  to the  $z$  direction. This means that the emerging wavefront can either be viewed as a set of plane waves each originating from a monochromatic point source emitting at the appropriate phase in the direction  $\theta$ , or as a single wave with a complex amplitude. This is represented in Figure 2.2b. As the waves propagate away from the screen, a progressive phase difference develops between the straight-through wave front and the diffracted wavefront as shown in Figure 2.2c. When this phase difference reaches  $180^\circ$ , the straight-through and diffracted waves cancel out and amplitude fluctuations are fully developed in the wavefront. From the Figure 2.2c we see that phase difference is :

$$\text{Phase difference} = \frac{2\pi}{\lambda} (z_0 - z_0 \cos \theta)$$

$$\text{Phase difference} = \frac{2\pi z_0}{\lambda} (1 - \cos \theta)$$

$$\simeq \frac{\pi z_0 \theta^2}{\lambda} = \frac{\pi z_0 \lambda}{a^2}$$

When this phase difference reaches another  $\frac{\pi}{2}$  the waves cancel, giving a condition that the scale size  $a = \sqrt{2z_0\lambda}$ . This condition implies that the larger the scale sizes, greater is the distance from the screen where amplitude variations are developed. Scales larger than  $a = \sqrt{2z_0\lambda}$  do not contribute to the diffraction pattern. This is called the Fresnel filter. At a distance  $z_0$  the straight-through and diffracted waves have a phase difference  $\Delta$  as shown in Figure 2.2d. The diffracted wave is now in anti-phase with the main wave and has an amplitude given by  $\left(\frac{E_0\beta'}{2} \sin \Delta\right)$ .

$$\therefore \text{The wave amplitude} = E_0 \left\{ 1 - \beta' \sin \left( \frac{k^2 \lambda z}{4\pi} \right) \right\}$$

(the factor of 2 due to two waves).

$$E(x, y, z) = E_0 \left\{ 1 - \beta' \sin \left( \frac{k^2 \lambda z}{4\pi} \right) \cos kx \right\}$$

$$E(x, y, z) = E_0 \left\{ 1 - \phi(x, y, \Delta z) \sin \left( \frac{k^2 \lambda z}{4\pi} \right) \right\}$$

The first term in the brackets represents the straight-through wave, the second term  $(\phi(x, y, \Delta z))$  is the phase imposed by the screen while the term  $\sin \left( \frac{k^2 \lambda z}{4\pi} \right)$  is the Fresnel filter factor. The effect of the Fresnel filter is shown in Figure 2.3a-2.3c, which illustrates how the Fourier spectrum of amplitude fluctuations at a given distance from a phase-changing screen is related to the spectrum of phase fluctuations. The spectrum of the phase fluctuations is taken to be a Gaussian with a characteristic scale size  $a = 100$



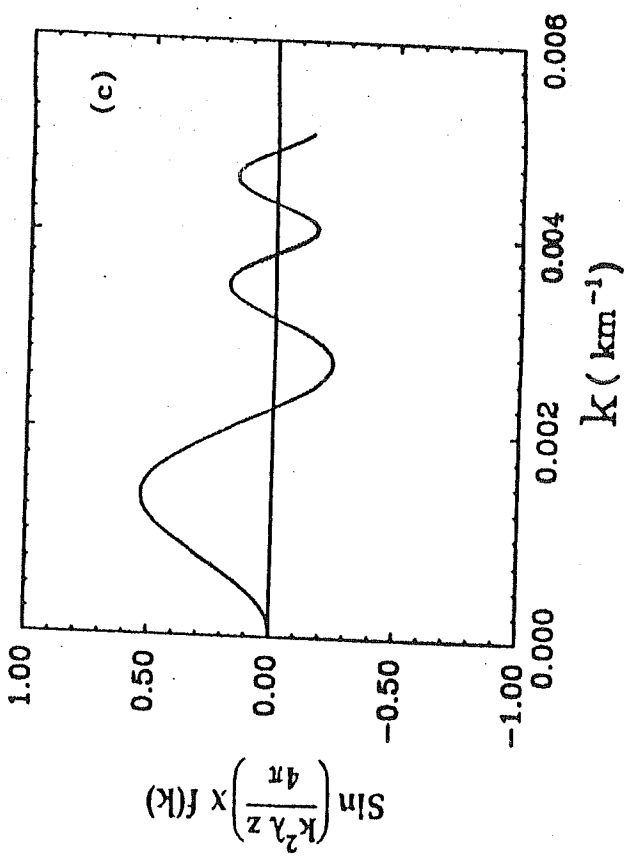
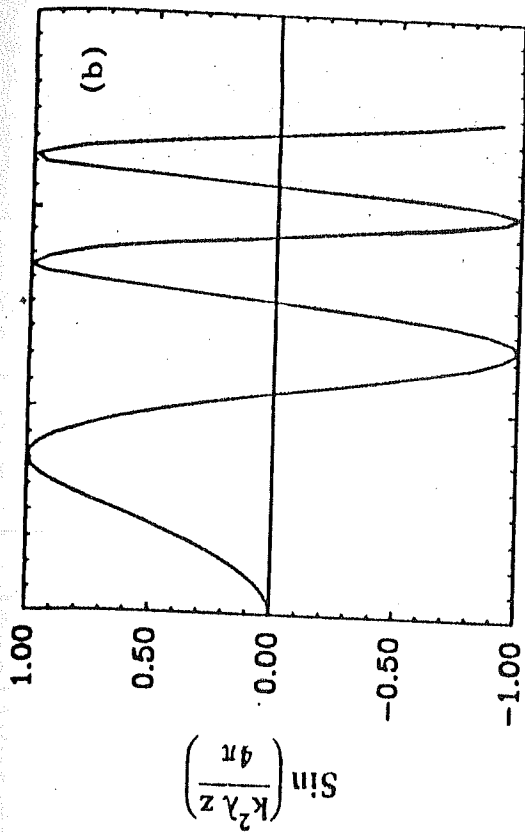
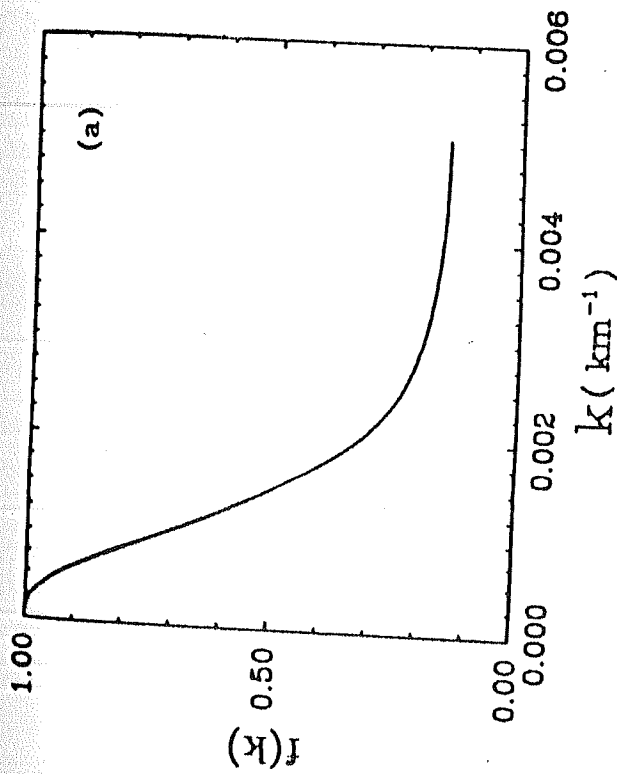


Figure 2.3a - 2.3c Illustrates the effect of the Fresnel filter function (2.3b) on a Gaussian spectrum of phase fluctuations (2.3a) of characteristic scale size of 100 km. The Fresnel filter function is shown for  $\lambda = 2.91\text{m}$  and  $z = 0.5 \text{ AU}$ . The spectrum of amplitude fluctuations is shown in 2.3c. The horizontal axis in all cases is the spatial frequency ( $k$ ), measured in cycles/km.

km as shown in Figure 2.3a. The Fresnel filter function, for  $\lambda = 2.91$  m and  $z = 0.5$  AU, which is a rapidly oscillating function is shown in Figure 2.3b. The resultant product of the two is the spectrum of amplitude fluctuations and is shown in Figure 2.3c. The horizontal axis is the spatial frequency  $k$  measured in cycles per kilometer. The successive zeros of the function occur at values of  $k$  given by  $k_n = \left(\frac{n}{\lambda z}\right)^{\frac{1}{2}}$  and for our operational wavelength of 2.91 m and for  $z = 0.5$  AU,  $k = 0.0021 \text{ km}^{-1}$ ,  $0.0037 \text{ km}^{-1}$ , --- for  $n = 1, 2, \dots$  etc. The Figure 2.3c is essentially conveying that irregularities of the size corresponding to the main peak are most effective in producing amplitude fluctuations at a distance  $z$ . The Fresnel filter thus acts like a high pass filter and is purely a propagation effect. So at a distance  $z$  away from the screen, each component in the irregularity spectrum gets multiplied by the Fresnel factor giving :

$$E(x, y, z) = E_0 \left( 1 - \alpha \int_{-\infty}^{\infty} F(k) \sin\left(\frac{k^2 \lambda z}{4\pi}\right) e^{ikx} dk \right) \dots\dots\dots (2.2)$$

## 2.5 Scintillation Index.

A radio telescope is incapable of measuring phase fluctuations and can only measure the intensity of the incoming radiation. In the case of an IPS telescope, like the 10,000 m<sup>2</sup> dipole array at Thaltej, the

fluctuations in intensity of the source flux are measured in terms of a parameter called the scintillation index (m). This parameter is defined as the ratio of the scintillating flux to the mean source flux ie.  $m = \frac{\Delta s}{\langle s \rangle}$ ,

where  $\Delta s$  is the rms scintillating flux density and  $\langle s \rangle$  is the mean source flux density. To see how the scintillation index is related to the rms phase fluctuations and thereby to the rms electron density and the scale sizes in the irregular medium, we can start by extrapolating expression (2) to two-dimensions to get an expression for  $\Delta E^2(x, y, z)$  as :

$$= E_0^2 \alpha^2 \left[ \int_{-\infty}^{\infty} \int_{-\infty}^{\infty} F(k_x k_y) \sin\left(\frac{(k_x^2 + k_y^2) \lambda z}{4\pi}\right) e^{i(k_x x + k_y y)} dk_x dk_y \right]^2$$

Let  $f(x, y, z)$  be the fourier transform of  $F(k_x k_y) \sin\left(\frac{(k_x^2 + k_y^2) \lambda z}{4\pi}\right)$

$$\text{ie} \quad f(x, y, z) \Leftrightarrow F(k_x k_y) \sin\left(\frac{(k_x^2 + k_y^2) \lambda z}{4\pi}\right)$$

$$\Delta E^2(x, y, z) = E_0^2 \alpha^2 f^2(x, y, z)$$

$$\therefore \langle \Delta E^2(x, y, z) \rangle \propto \int_{-\infty}^{\infty} \int_{-\infty}^{\infty} f^2(x, y, z)$$

By Parseval's theorem.

$$\langle \Delta E^2(x, y, z) \rangle \propto \int_{-\infty}^{\infty} \int_{-\infty}^{\infty} F(k_x, k_y) \sin\left(\frac{(k_x^2 + k_y^2) \lambda z}{4\pi}\right) dk_x dk_y$$

If  $G(k_x, k_y)$  represents the power spectrum of the irregularities in the thin screen then :

$$\langle \Delta E^2(x, y, z) \rangle \propto \int_{-\infty}^{\infty} \int_{-\infty}^{\infty} G(k_x, k_y) \sin\left(\frac{(k_x^2 + k_y^2) \lambda z}{4\pi}\right) dk_x dk_y$$

But as  $z \rightarrow \infty$ , the Fresnel filter factor will simply oscillate more and more rapidly and over any small interval its value will be  $\frac{1}{2}$  giving.

$$\langle \Delta E^2(x, y, z) \rangle \propto \frac{c}{2} \int_{-\infty}^{\infty} \int_{-\infty}^{\infty} G(k_x, k_y) dk_x dk_y \quad \dots\dots\dots(2.3)$$

where  $c$  is a constant. On passing through the screen, the wavefront has phase fluctuations imposed on it by the irregularities in the screen. These fluctuations will match those in the screen exactly.

ie.  $\Delta\phi(x, y, \Delta z) \propto F(k_x, k_y)$

$$\langle \Delta \phi^2 \rangle \propto \int_{-\infty}^{\infty} \int_{-\infty}^{\infty} G(k_x, k_y) dk_x dk_y$$

$$\langle \Delta \phi^2 \rangle = c' \int_{-\infty}^{\infty} \int_{-\infty}^{\infty} G(k_x, k_y) dk_x dk_y \quad \dots\dots\dots (2.4)$$

with  $c'$  being another constant. From equation (3) and (4) :

$$\langle \Delta E^2(x, y, z) \rangle_{\text{far field}} = \frac{1}{2} \Delta \phi^2 \text{ at the screen.} \quad \dots\dots\dots (2.5)$$

We have already defined the scintillation index as the ratio of the rms flux to the mean source flux. This can be written as.

$$m = \frac{\langle \Delta I^2 \rangle^{\frac{1}{2}}}{\langle I \rangle}$$

$$m \simeq 2 \frac{\langle \Delta E^2 \rangle^{\frac{1}{2}}}{\langle E \rangle}$$

$$m \simeq 2 \langle \Delta E^2 \rangle^{\frac{1}{2}}$$

because  $\langle E \rangle$  is usually normalized to unity.

Thus  $m \simeq \sqrt{2} \Delta \phi$  \dots\dots\dots (2.6)

Here  $\Delta\phi$  is the rms phase deviation imposed by the thin screen of density irregularities. We thus see that by measuring the scintillation index ( $m$ ) we can infer the rms phase deviation and hence the rms  $\Delta N$  through equation (2.1).

## 2.6 Bandwidth Effect.

In all the foregoing discussions we have assumed that the radiation incident on the thin slab of density irregularities is monochromatic. Generally such an assumption is valid but while dealing with a phenomenon like IPS of very small diameter radio sources, the scintillation index ( $m$ ) can be modified considerably by the finite receiver bandwidth used (Little, 1968). The effect of the finite bandwidth is such that it can set a limit upon the smallest diameters that can be measured by IPS.

If we consider two points on the thin screen separated by a finite distance, then the diffraction pattern formed on the ground at a point P at a distance  $z$  away from the screen will depend upon the path difference between the waves arriving at P from the two separated points, say A and B. In other words the diffraction pattern at P is composed of the sum of waves from all parts of the screen. In general the envelope of a wave component at an arbitrary angle  $\theta$  is delayed with respect to the primary or straight-through wave by a path difference given by

$$\text{Path difference} = z \left( \frac{1}{\cos \theta} - 1 \right)$$

$$\simeq \frac{z \theta^2}{2} \quad \text{if } \theta \ll 1 \quad (\text{as is usual in IPS})$$

$$\simeq \frac{k \lambda}{2 \pi} \Delta \phi$$

$$\text{Largest } \theta \text{ is given by } \simeq \frac{z k^2 \lambda^2 \Delta \phi^2}{8 \pi^2}$$

$$\therefore \text{Largest path difference} \simeq \frac{z k^2 c^2 \Delta \phi^2}{8 \pi^2 v^2}$$

While observing with a finite bandwidth  $\Delta v \ll v$ , the waves have a coherence length over a distance of about  $\left( \frac{c}{2 \Delta v} \right)$ . If the path difference is greater than this coherence length then the diffraction pattern becomes smeared or in other words the angular spectrum becomes narrower and the scale of the pattern on the ground increases. The components in the pattern of highest spatial frequency have the largest path delays and are therefore removed preferentially due to incoherence. From the previous expression we can get a condition on the bandwidth as

$$\Delta v \leq \frac{4 \pi^2 v^2}{z c k^2 \Delta \phi^2}$$

For example in the IPM at 0.5 AU where  $\langle a \rangle \simeq 100$  km and at 103 MHz using a bandwidth of 4 MHz, smearing will set in when  $\Delta \phi \geq 1.09$  radian.

## 2.7 Effect of Finite Source Size.

A radio source of finite size can be considered to be made up of a collection of point sources. If we thus consider the diffraction pattern caused by a point on a source which is situated at a great distance from the diffracting medium and which lies at a distance  $z$  from the ground, then we will see on the ground in the  $(x, y)$  plane an intensity distribution  $I(x, y)$ . Let this diffraction pattern be represented by :

$$f(x, y) = \frac{I(x, y) - \langle I \rangle}{\langle I \rangle}$$

Here the averages are taken over the  $(x, y)$  plane. Another point on the source situated in a different direction to the first point will also give rise to a diffraction pattern in the  $(x, y)$  plane. The two patterns, though, will be displaced by an amount  $z\theta$  and  $z\phi$  where  $(\theta, \phi)$  are the angular coordinates of the second point with respect to the first point. The resultant diffraction pattern will be

$$g(x, y) = \iint P(\theta, \phi) f(x - z\theta, y - z\phi) d\theta d\phi$$

where  $P(\theta, \phi)$  is the brightness distribution of the source. Introducing two new variables  $\xi = z\theta$  and  $\eta = z\phi$  we can write



$$g(x, y) = \frac{1}{z^2} \iint P\left(\frac{\xi}{z}, \frac{\eta}{z}\right) f(x - \xi, y - \eta) d\xi d\eta$$

$$\text{Writing } P'(\xi, \eta) = \frac{1}{z^2} P\left(\frac{\xi}{z}, \frac{\eta}{z}\right)$$

$$g(x, y) = \iint P'(\xi, \eta) f(x - \xi, y - \eta) d\xi d\eta$$

This is nothing but the convolution of the brightness distribution of the source and the diffraction pattern of a point source as one would expect. Here  $P'(\xi, \eta)$  is the brightness distribution of the source in the changed or reduced coordinates.

From this the intensity spectrum of an extended source can be written in terms of the point source intensity spectrum (Salpeter, 1967) through the Cohen-Salpeter equation given by

$$M_{2I}(q)_{\text{extended}} = M_{2I}(q)_{\text{point}} |V(q, z)|^2$$

and it is the product of the spectrum that would be obtained by a point source and the squared magnitude of the actual source visibility function ( $V$ ), which is simply the Fourier transform of the source brightness distribution. The visibility function is defined, in terms of the measured scintillation index as

$$V = \frac{m(\text{extended source})}{m(\text{point source})}$$

## 2.8 Summary.

In the foregoing discussions the diffraction effects which occur when radiation passes through a medium containing randomly distributed phase-changing irregularities have been outlined. The relevant diffraction theory has been treated in detail by several authors, as already mentioned in the beginning of the chapter, and the reader is referred to reviews by Ratcliffe, 1956 and Salpeter, 1967.

In summary, we can start with, in the weak scattering regime where the total phase deviation imposed on the incoming wave is  $\ll 1$  radian, the three dimensional spectrum of electron density irregularities which can be represented by  $M_{3N}(q_x, q_y, q_z)$  where  $q_x, q_y, q_z$  are the wavenumbers. This spectrum impresses a two-dimensional spectrum of phase fluctuations on the wavefront given by

$$M_{2\phi}(q_x, q_y) = 2\pi r_e^2 \lambda^2 M_{3N}(q_x, q_y, 0)L$$

where  $L$  is the thickness of the scattering region,  $r_e$  is the classical electron radius, and  $\lambda$  is the wavelength. This propagates in the  $z$  direction until it is observed as a two-dimensional spectrum of intensity variations on the earth given by

$$M_{2I}(q_x, q_y) = 4 \sin^2 \left( \frac{q^2 \lambda z}{4\pi} \right) M_{2\phi}(q_x, q_y)$$

where :

$$q = (q_x^2 + q_y^2 + q_z^2)^{\frac{1}{2}}$$

Due to the medium itself moving in the  $x$  - direction with a velocity ( $v$  - the average solar wind velocity), this transforms to a one-dimensional temporal spectrum of intensity variations, as shown in Figure 2.4, given, in the observer's plane, by :

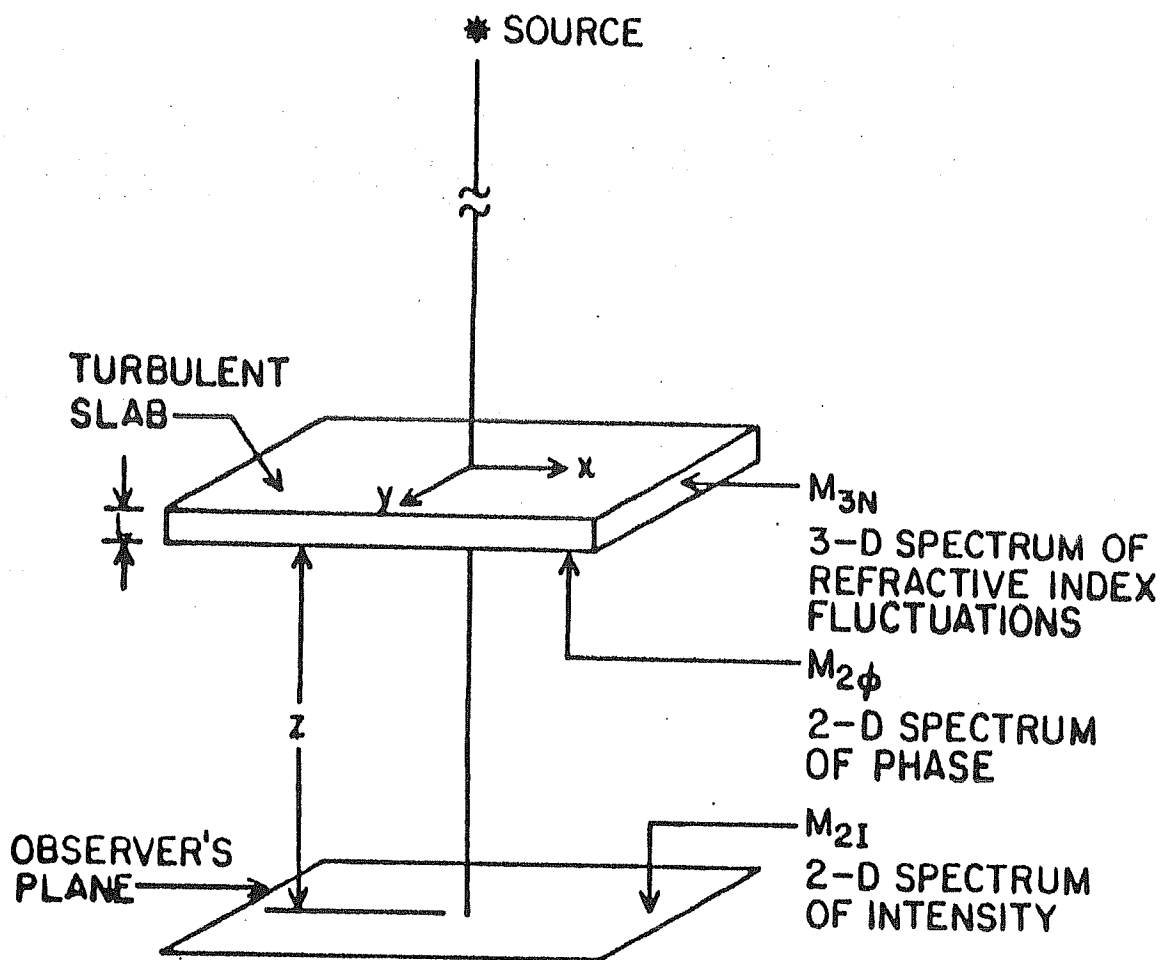
$$P_1(v) = \int_{-\infty}^{\infty} M_{21}\left(\frac{2\pi v}{v} \cdot q_y\right) dq_y$$

In the weak scattering case, the diffraction is actually made up of contributions from scattering slabs all along the line of sight to the source. We can thus approximate the resulting field with a sum of the fields produced by the individual slabs, giving :

$$P_1(v) = \int_0^{\infty} P_1(v, z) dz$$

Thus in the case when the IPS method is used to derive solar wind velocities (Hewish and Symonds, 1969; Coles and Maagoe, 1972; Coles, Rickett and Rumsey, 1974), the measured values do not apply to a unique slab of plasma moving across the observer's line of sight but is rather a weighted average of the velocity components normal to the line of sight from all the slabs. The measured velocity will thus be less than the true value (Jokipii and Lee, 1973).

The effects of finite source size, finite receiver bandwidth, and the Fresnel filter have been derived (Budden and Uscinski, 1970) who have



$$M_{2\phi}(q_x, q_y) = \frac{4\pi^2}{\lambda^2} \cdot L \cdot M_{3N}(q_x, q_y, q_z = 0)$$

$$M_{2I}(q_x, q_y) \approx 4 \sin^2\left(\frac{q^2 \lambda z}{4\pi}\right) M_{2\phi}(q_x, q_y)$$

**Figure 2.4**

Shows how the initial 3-D spectrum of refractive index fluctuations is converted to a 2-D spectrum of phase and then to a 2-D spectrum of intensity in the observers plane.

derived an expression for the reduction factor A due to these effects. In the case of a source with a Gaussian brightness distribution observed with a receiver having a bandpass can be written (Readhead, 1971) as

$$A(f, b, h) = \frac{f^2}{(1 + h^2 + fb) \left[ (1 + h^2 + fb)^2 + f^2 \right]}$$

Where

$$h^2 = 2 \left( \frac{z \theta_0}{a} \right)^2$$

$$f = \frac{4z}{a^2 k}$$

$$2b = \frac{\text{half-power bandwidth}}{\text{frequency}}$$

$$k = \text{the wavenumber}$$

$$2 \theta_0 = \frac{1}{e} \text{ width of the Gaussian brightness distribution}$$

$$z = \text{distance of screen from observer}$$

Thus if S(r) represents the scattering power of the medium at a distance r from the sun we can write the scintillation index in the far-field as :

$$m^2(\epsilon) = \int_{\text{diffracting medium}} S(r) A(f, b, h) dz \dots\dots\dots (2.7)$$

The effect of both the finite source diameter and the finite bandwidth is to

act as low-pass filters on the spatial spectrum and reduce the scintillation index. Unfortunately an analogous treatment, for the strong scattering case, giving similar results is yet to be derived when the medium is extended in the  $z$  direction and under conditions of multiple scattering. The spectrum of intensity fluctuations resulting from the propagation of a plane wave through a thin but arbitrarily strong layer of refractive index variations, though, have been computed (Rumsey, 1975; Mariani, 1975 b) and the results have been found to be in agreement with the results of radio scintillation measurements.

# Chapter - III

## THE THALTEJ RADIO TELESCOPE AND ASSOCIATED INSTRUMENTATION

### 3.1 Introduction.

The successful implementation of any radio astronomical project depends almost entirely upon the instrumentation which at meter wavelengths comprises the following three elements : 1) A dipole array; 2) A radio receiver and 3) A data acquisition system. The work presented in this thesis was carried out mostly with a  $10,000 \text{ m}^2$  filled aperture dipole array operating at 103 MHz. This array, located at Thaltej, Ahmedabad (  $23^\circ 18' \text{ N}$ ;  $72^\circ 29' \text{ E}$  ) and constructed in mid-1984, is one of a network of three similar telescopes, the other two being situated at Rajkot (  $22^\circ 18' \text{ N}$ ;  $70^\circ 44' \text{ E}$  ) and Surat (  $21^\circ 09' \text{ N}$ ;  $72^\circ 47' \text{ E}$  ), and each having a  $5,000 \text{ m}^2$  physical area. Plate 1 is a photograph of the dipole array at Thaltej.

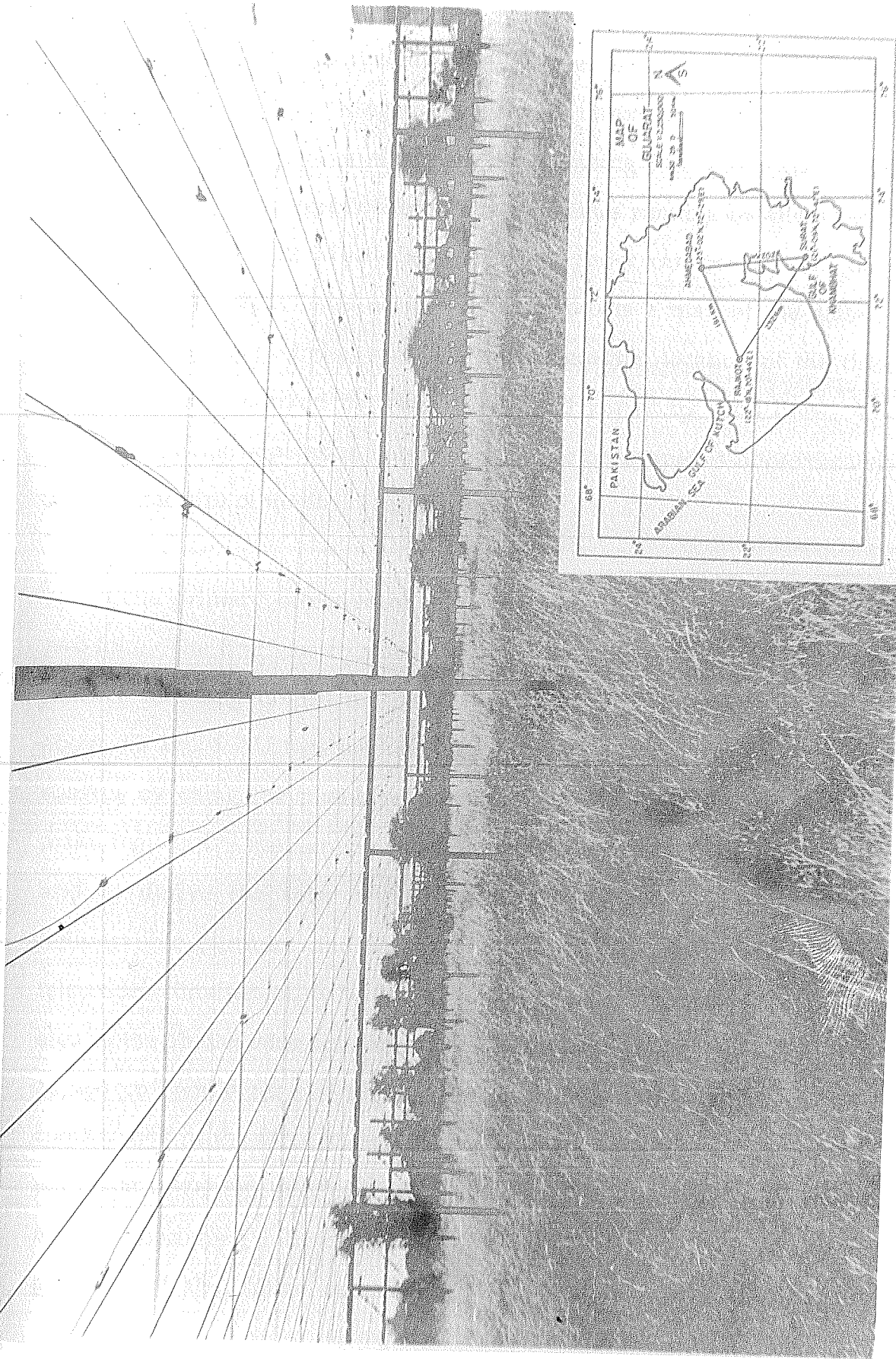


Plate 1 A view of the dipole array at Thaltej showing the reflector, dipoles and transmission lines. Inset is a map of Gujarat showing the geographic location of the three telescopes.



This view shows a portion of the array as seen from below the reflecting plane which is seen running from North to South into the plane of the paper. Individual dipole elements, also running into the plane of the paper and loaded on open wire transmission lines running parallel to each other from left to right (West - East) across the paper, can also be seen. Inset on the bottom right hand corner of the photo is a map of the state of Gujarat, in Western India, showing the geographic location of the three telescopes, here marked by filled circles and joined by solid lines. The average baseline separation between the three telescopes is approximately 200 km, the size of the first Fresnel zone.

The primary objective of this network of three dipole arrays was two-fold. The first was to study the structure and distribution of plasma density inhomogeneities in the interplanetary medium (IPM) between about 0.3 and 1 AU together with the angular structure of compact radio sources by using the phenomenon of IPS. The second objective was to make regular IPS measurements of a number of scintillating radio sources and to derive the solar wind velocity at different radial distances, heliographic latitudes and longitudes around the sun using the three telescopes simultaneously with good relative time accuracy. The physical area of the Thaltej telescope, during the period mid-1984 to end of 1987 was  $10,000 \text{ m}^2$ , while that at Rajkot and Surat was  $5,000 \text{ m}^2$  each. The construction of the three telescopes was taken up in stages with the Thaltej telescope becoming fully operational in mid-1984 and the three telescope network becoming fully operational in early 1987. Figure 3.1 is a block diagram of the entire experimental setup at Thaltej comprising the

## BLOCK DIAGRAM OF IPS TELESCOPE-THALTEJ

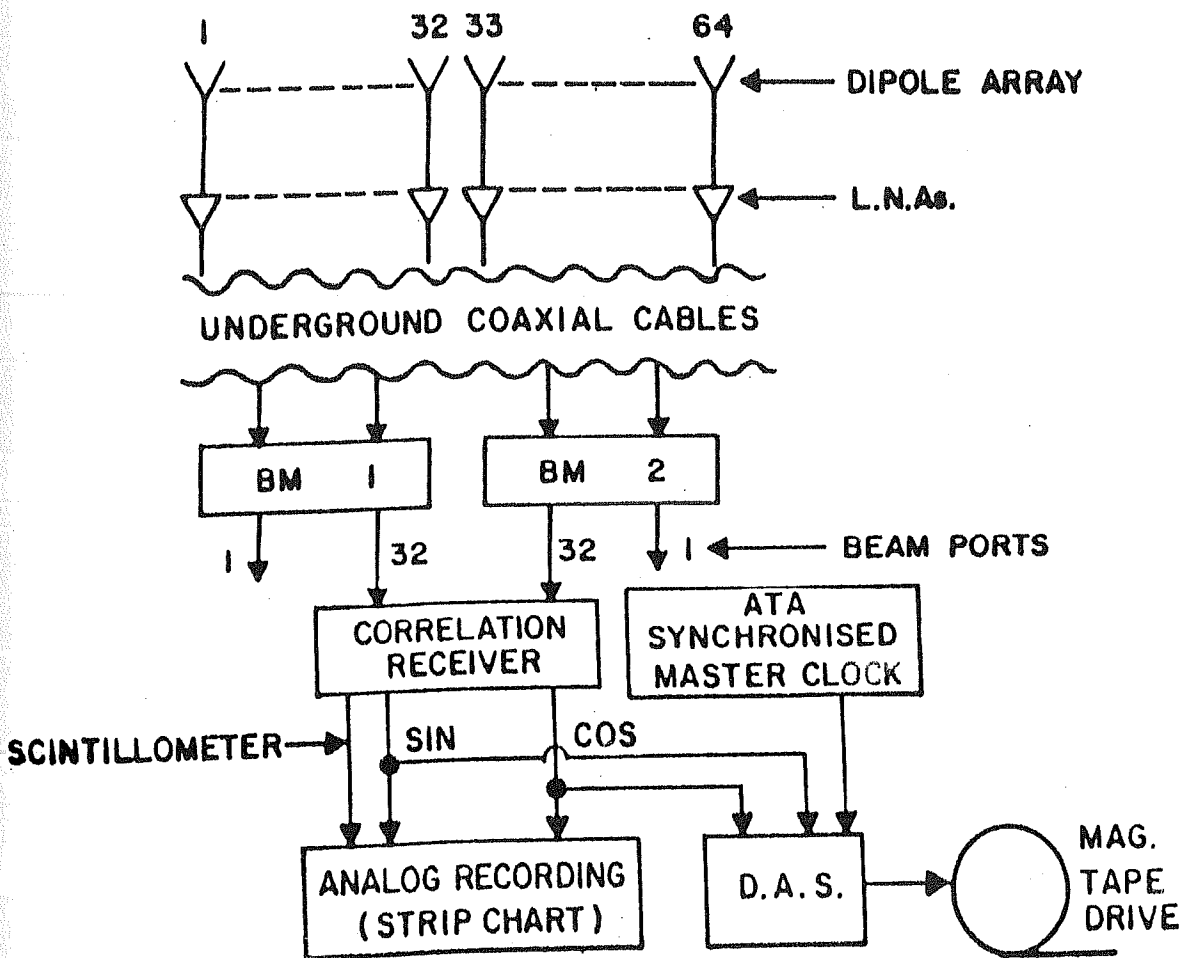


**Figure 3.1** Block diagram of the IPS telescope at Thaltej showing all the subsystems.

antenna array, preamplifiers and RF cables on the field and the receiving and data acquisition systems in the receiver building.

### 3.2 The Thaltej Antenna Array.

The antenna array at Thaltej (see plate 1), in its  $10,000 \text{ m}^2$  configuration, consists of 2048 fullwave dipoles deployed in 64 East-West rows of open wire transmission lines, each loaded with 32 North-South dipoles. The array forms a rectangular aperture measuring about 200 m in North-South by 50 m in East-West and is divided into two sections of 32 rows each. The array is operated as a phase-switching interferometer observing sources at meridian transit using a correlation receiver. The array is followed by low-noise preamplifiers on each of the 64 rows to compensate for the RF coaxial cable attenuation and insertion losses due to the rest of the receiving system ahead of them. Figure 3.2 is a schematic representation of the dipole array at Thaltej.

The sixty four transmission lines and their dipoles are each supported by 2" diameter Mild Steel (M.S.) pipes which are each supported by a guy wire and embedded in the earth in  $2\frac{1}{2}$  feet of cement concrete. The dipoles and transmission lines themselves are made of 3.2 mm diameter (10 SWG) copper-clad steel wire and are mounted approximately  $0.22\lambda$  (60 cm) above a well-stretched horizontal ground plane which is also made of the same copper-clad steel wire. The dipoles, having been cut from large round bundles of wire, retain a slight curvature. The resulting height

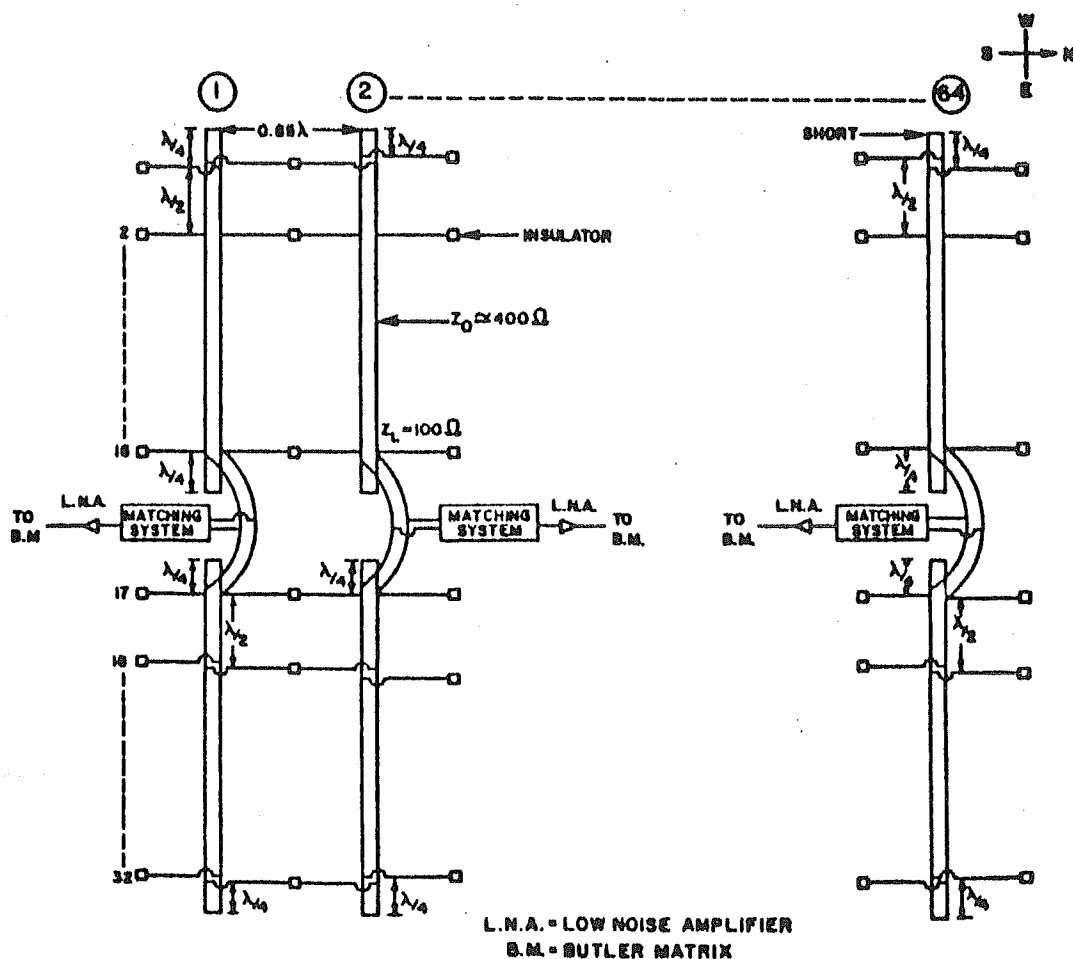


**Figure 3.2** Shows a schematic representation of the 10,000 m<sup>2</sup> dipole array indicating the layout of the open wire transmission lines and the individual dipoles. Also indicated is the jumper one wavelength ( $\lambda$ ) long, joining the two 5,000 m<sup>2</sup> halves and tapped at its center.

variation due to this, between the dipole plane and the reflector plane is  $\pm 5$  cm or  $0.0172\lambda$ . This results in a phase error of about  $2\pi \times 0.0172$  radians (0.108 rad). Taking this value as the rms variation and assuming distortions to be large in number, Gaussian in shape and uniformly distributed, the antenna directivity becomes smaller by a factor of  $e^{-0.108} = 0.899$ . The corresponding changes in the antenna pattern are a reduction in magnitude of the main lobe and an increase in the side lobe level.

The transmission lines are stretched between the 2" M.S. pipes and the tension on each line can be adjusted using turn-buckles. The line is also supported in the middle by an insulator fixed on a wooden strut to reduce the sag in the line. A separation of about 5 cm between the parallel wires of the transmission line is maintained by two M.S. pulleys at the end of each transmission line. Hylem spacers are also used at regular intervals along each transmission line to maintain the spacing. This spacing of 5 cm corresponds to a characteristic impedance of about  $400\Omega$ . As can be seen from Figure 3.2, each transmission line is shorted on both ends at a distance of  $\frac{1}{4}\lambda$  (72.5 cm) from the last dipole, thus creating a cavity feeder. The dipoles themselves are spaced out at intervals of  $\frac{1}{2}\lambda$  (145.5 cm) and alternate dipoles are transposed to achieve proper phasing. Insulating sleeves of Hylem are inserted on each transposed dipole to prevent it from touching the other conductor of the transmission line. The actual length of each fullwave dipole is 247.4 cm ( $0.85\lambda$ ). This length is determined experimentally so that the dipole presents a purely resistive impedance to the transmission line at 103 MHz. All the dipoles are crimped on to the transmission lines with the help of copper T-joints. As the array was built

in two stages of  $5,000\text{ m}^2$  each, with the expansion extending the dimensions of the array in the Eastward direction, the two halves are joined together by an open wire transmission line one wavelength long having a characteristic impedance of approximately  $400\ \Omega$ . The feed point is taken from the center of this transmission line through a bazooka type balun to the input of a low noise preamplifier. The reflector plane which is made up of 80 wires spaced roughly  $\frac{1}{10}\lambda$  (30 cm) apart, is stretched between two rows of standard P & T terminals and supported by several equally spaced  $1\frac{1}{2}$ " diameter M.S. pipe welded support structures.

### 3.2.1 The Balun and Low Noise Preamplifier.

The antenna has got a balanced output, while the input and output terminals of the preamplifiers are unbalanced. Stated broadly, the unbalance is caused because the outer conductor of the coaxial cable is not coupled to the antenna in the same way as the inner conductor. This causes current to flow on the outside of the outer conductor leading to a loss in power at the outputs of the receiver. The system must thus be detuned for currents on the outside of the line. This can be achieved by either making the current either cancel itself or by choking it off. Devices that achieve this fall in the category of circuits called baluns, a contraction for 'balanced to unbalanced'. In the Thaltej array a 'Bazooka' type balun is used and it consists of a copper sleeve  $\frac{1}{2}$ " in diameter and a quarter of a wavelength in length. Through this sleeve is passed a  $75\ \Omega$ , RG11/U coaxial cable of length 1.5 m. The bottom end of the sleeve is shorted with

the outer conductor of the coaxial cable thus causing a very high impedance at the open end of the outer conductor of the coaxial cable. Thus the sleeve acts like a choke coil in isolating the remainder of the line from the antenna and ensuring that the current flows only in the inner conductor of the coaxial cable.

The antenna impedance can also be matched to that of the low noise preamplifier by making use of the impedance transforming properties of the quarter-wave transmission line. The input impedance of a quarter-wave line terminated in a resistive impedance  $Z_R$  is given by  $Z_0 = \sqrt{Z_R Z_S}$ . This equation simply means that any value of load impedance  $Z_R$  can be transformed to any desired value of impedance  $Z_S$  provided the line can be constructed to have a characteristic impedance  $Z_0$ . Each dipole presents a resistive impedance of about  $2500\ \Omega$  across the transmission line which has a characteristic impedance of about  $400\ \Omega$ . Each dipole is thus tightly coupled to the line and sees a low impedance at its center. The resultant impedance of all the 32 dipoles at the transmission line is  $65\ \Omega$  to  $75\ \Omega \pm 3\ \text{pF}$  typically. The balun converts this into the coaxial line. Table 3.1 gives the characteristics of the balun.

The RF signal from each row of 32 dipoles is enhanced by a 3 stage cascade type low noise preamplifier (LNA). The circuit diagram of the LNA is shown in Figure 3.3. Underground coaxial cables laid 3 ft deep in the earth carry the signals from each line to the receiver room. The cables used are  $50\ \Omega$ , RG8/U, each cut just long enough to cover the required distance between the preamplifiers on the field and the receiver room. The

**Table 3.1: BALUN CHARACTERISTICS**

Total Length	1.5 m
Cable Used	RG11/U
Phase Difference	182.5°
Insertion Loss	0.25 db
Calculated Value of Loss	0.15 db



# 103 MHz LOW NOISE PRE-AMPLIFIER CASCADE CONFIGURATION

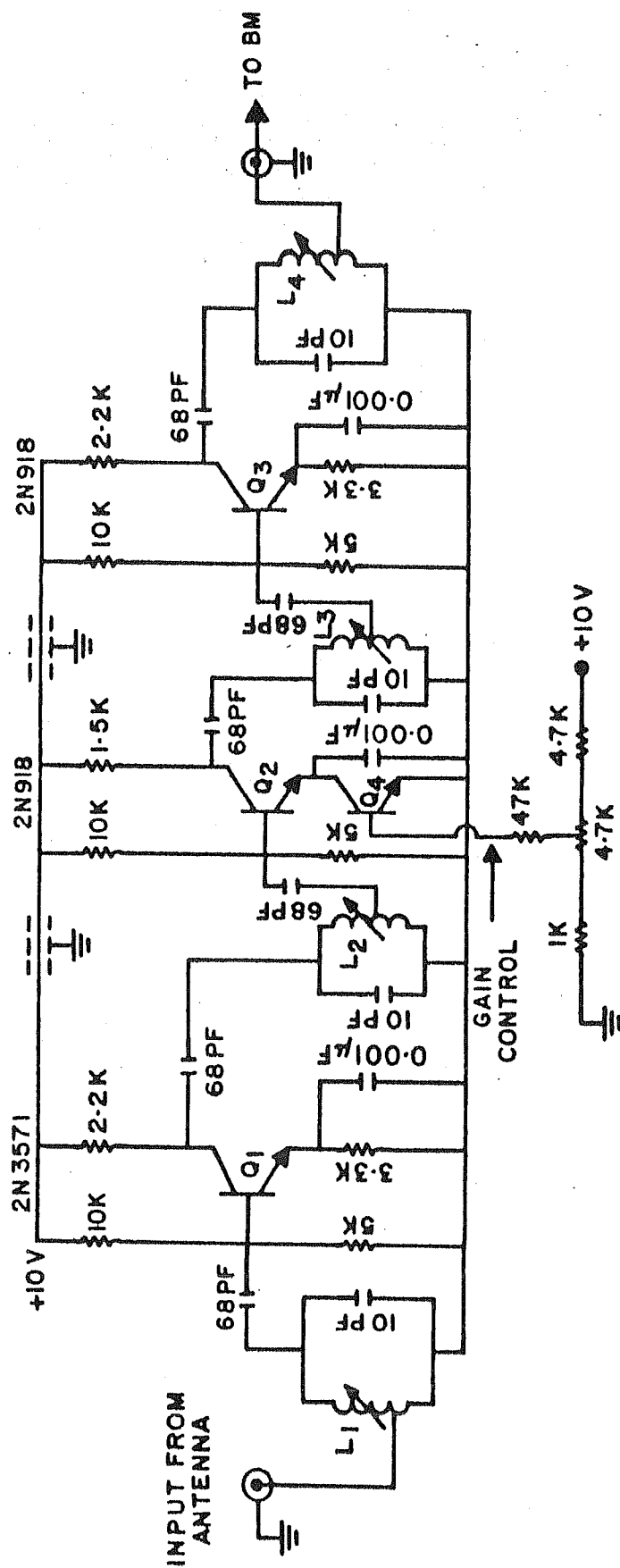


Figure 3.3 Circuit diagram of the Low Noise Preamplifier (LNA) used with the 10,000 m<sup>2</sup> array.

**Table 3.2 : CHARACTERISTICS OF THE LOW NOISE  
PREAMPLIFIER**

Center Frequency	103 MHz
Bandwidth (-3db)	7 MHz average
Gain	30 db to 40 db
Noise Figure	3 db average
Input and Output Impedance	55 to 60 $\Omega \pm 3$ pF

preamplifiers, designed so as to selectively amplify the 103 MHz signals, have a gain control in the second stage to compensate for the attenuation along the paths to the receiver. Good long-term phase stability is achieved by having a sufficiently large bandwidth (10% or more of the operating frequency typically). The preamplifier bandwidth at the Thaltej array is 7 MHz. The characteristics of the LNA are given in Table 3.2.

### 3.2.2 The Butler Matrix.

After amplification the RF signal is carried through underground coaxial cables to the receiver room, where a precision vector voltmeter was used together with a signal generator at 103 MHz to ensure that the signals arrived at the cable ends with very small relative amplitudes ( $\pm 0.5$  db ) and phase ( $\pm 1.5^\circ$ ). The antenna as described in the foregoing section was designed to be a meridian transit instrument with no steering in declination. If the signals from each row are combined with different increments of phase, the antenna beam will point to a different declination. The Butler matrix (Butler and Lowe, 1961; Shelton and Kelleher, 1961; Delaney, 1962, Butler, 1966) achieves this in the most efficient manner by combining the signals from each of the lines in an equal number of different ways to create a set of beams which cover the whole range of declinations available to the antenna. In the Thaltej array the 32-beam Northern and the 32-beam Southern patterns are combined separately in 32 different ways, in two independent Butler matrices, (BM's) to create 32 beams deployed in declination: This action of the BM is

**Table 3.3: CHARACTERISTICS OF THE BUTLER MATRIX**

Insertion Loss	1 db
Phase Error	1.5 ° average
Port Impedance	54 $\Omega \pm 2$ pF
Isolation Between Ports	35 db typical
Transmission Linearity	0.3 db

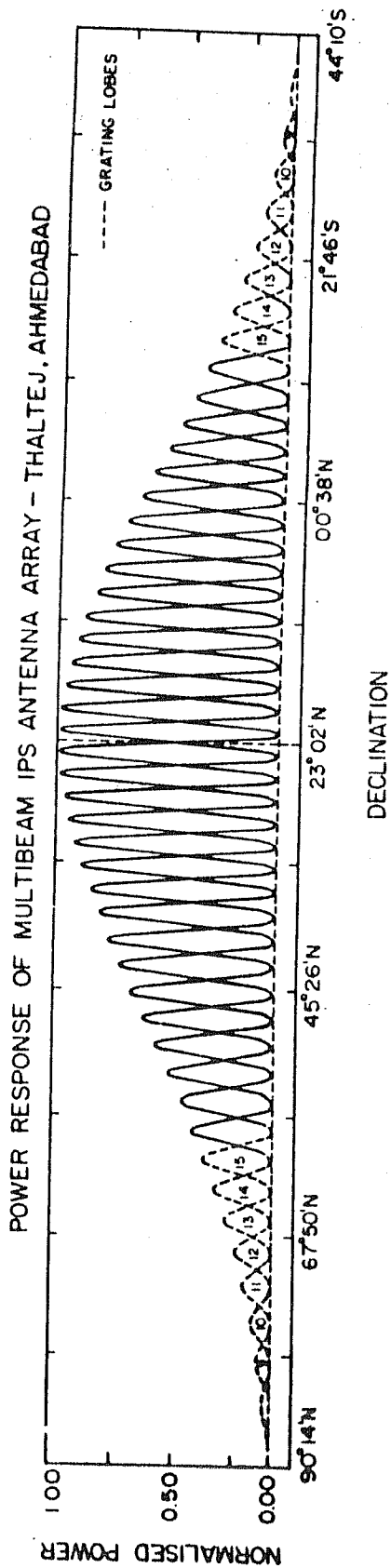


Figure 3.4 Shows the normalized declination power response of the Thaltej array, formed by each of the two 32 element Butler Matrices.

analogous to the Fast Fourier Transform algorithm used in digital computers. The 32 beams together cover a declination range from  $5^{\circ}$  S to  $55^{\circ}$  N with each beam having a width to half power of  $1.8^{\circ}$  NS  $\times$   $3.6^{\circ}$  EW and crossing the adjacent beams on either side at -4 db points. Since the projected area of the antenna varies as  $\cos z$ , where  $z$  is the angle from the zenith, the overall declination pattern has a Cosine taper. The inter-element spacing of  $0.85 \lambda$  and a foreshortening effect due to the apparent change in inter-element spacing for a source as it passes through the beam cause the array to have grating lobe responses (Kraus, 1966). Figure 3.4 is a computer plot of the declination response of the Thaltej array showing the 32 beams and the grating lobes, here marked by broken lines. It can be seen that the grating responses become significant beyond the 12th beam on either side. Table 3.3 gives the characteristics of the Butler matrix.

### 3.3 The Correlation Receiver.

The correlation receiver at Thaltej is a dual channel (Sin and Cos) receiver which is connected to the two halves of the antenna array to form a phase-switched interferometer in declination. The receiver has a common crystal-controlled local oscillator operating at 73 MHz, giving an IF of 30 MHz for each channel with a bandwidth of about 4.5 MHz. A discrete source will thus produce correlated signal-noise powers  $(k \Delta T B)$  at the receiver inputs and corresponding IF output voltages with amplitude proportional to  $(k \Delta T B)^{\frac{1}{2}}$ . If the input and output are in phase then the multiplier output DC voltage is proportional to  $(k \Delta T B)$ , while if they have

a phase angle ( $\phi$ ) between them the d-c output voltage is proportional to  $(k \Delta T B \cos \phi)$ . Here  $k$  is the Boltzmann constant  $= 1.38 \times 10^{-23}$  Joules /  $^{\circ}\text{K}$ .  $\Delta T$  is the minimum detectable equivalent noise temperature and  $B$  is the overall halfpower bandwidth of the receiver.

Signals from the two halves of the antenna are brought to the two identical beam-forming networks described above and for a given source, transiting through a particular declination beam, signals of the corresponding beam ports of the two Butler matrices are given to the inputs of the two channels. Figure 3.5 is a block diagram of the correlation receiver showing the various components. A common local oscillator (73 MHz) feeds two balanced mixers through a phase switch. The outputs of the two mixers are divided into two parts using coaxial hybrid rings, marked in the figure as A and B. One output signal each from A and B are combined in phase in a third hybrid D to produce 'COS' signals, while the second output from A and B is combined in a fourth hybrid C after a delay of  $90^{\circ}$  to form 'SIN' signals. Each of the two receiver channels thus formed from the hybrids C and D are fed through two 30 MHz intermediate frequency (IF) amplifiers with an average half power bandwidth of 4.5 MHz. The outputs of these high gain (80 db) IF amplifiers are maintained at a constant level within about 1 db using an automatic gain control (AGC) having a time constant of about 3 seconds. The characteristics of the square-law detector are such that the AGC becomes effective without even the antenna being connected. The square-law detector diodes are selected for similarity and are connected so that the voltage remains within the square-law range of about 10 mV to 70 mV. The AGC is so adjusted that

# CORRELATION RECEIVER FOR IPS TELESCOPE - THALTEJ

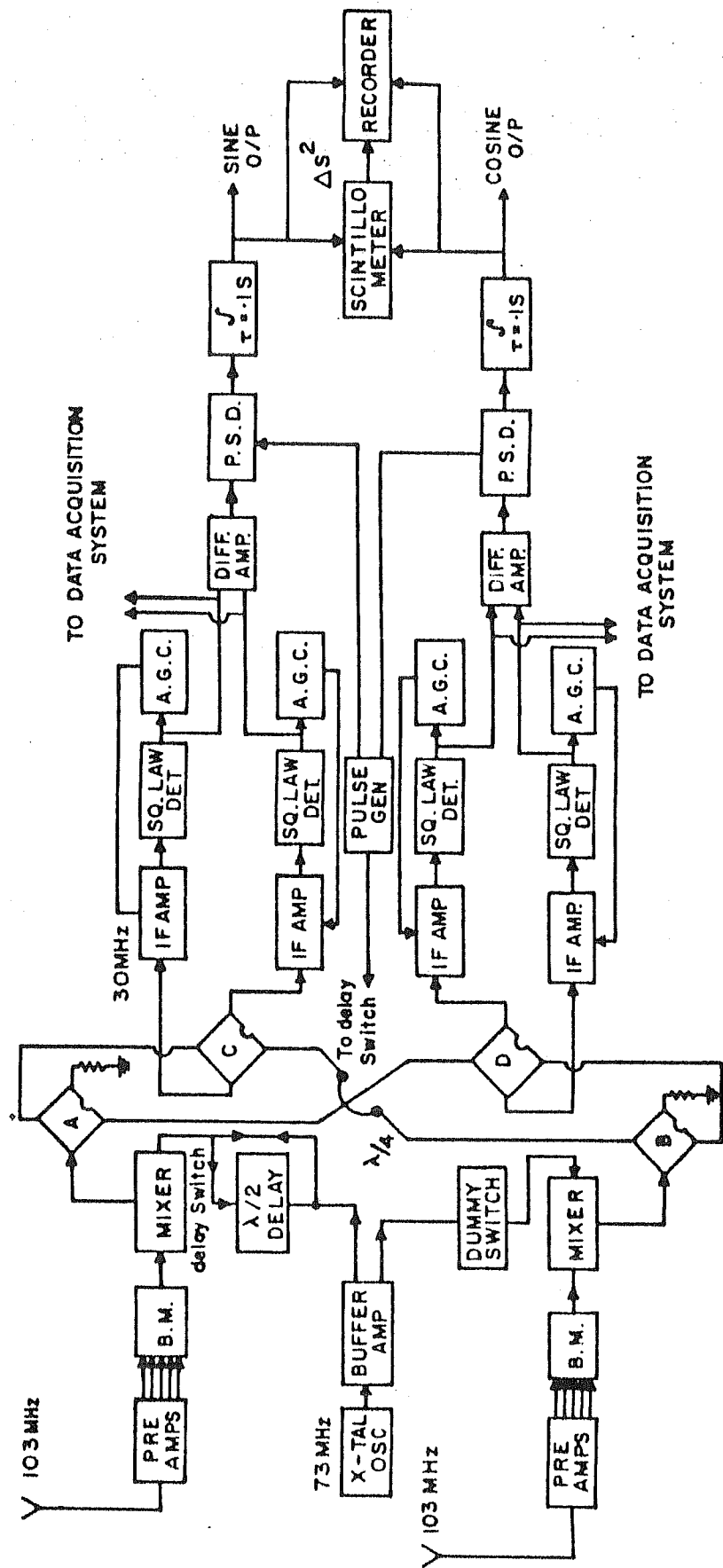


Figure 3.5 Shows the block diagram of the dual channel correlation receiver used at Thaltej.



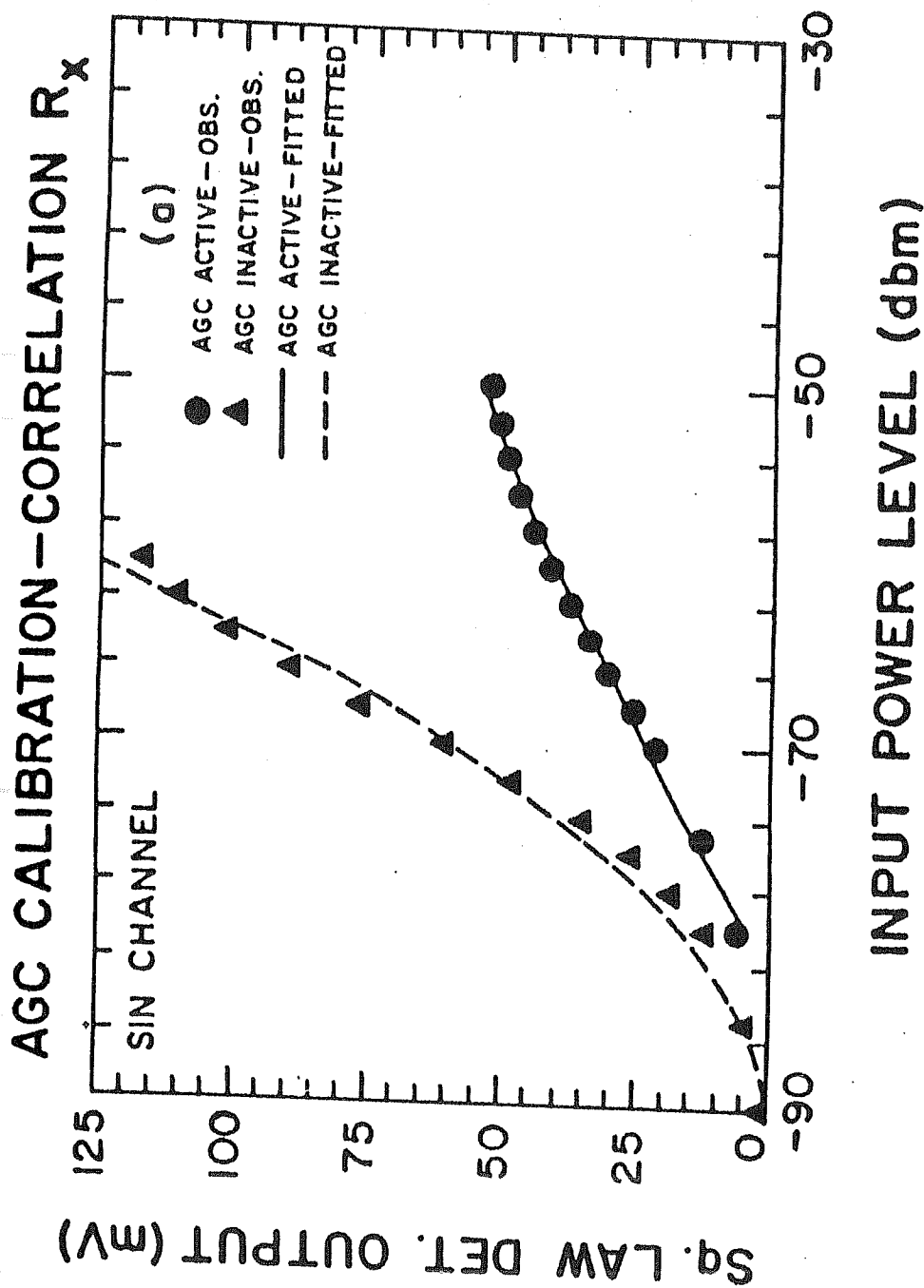
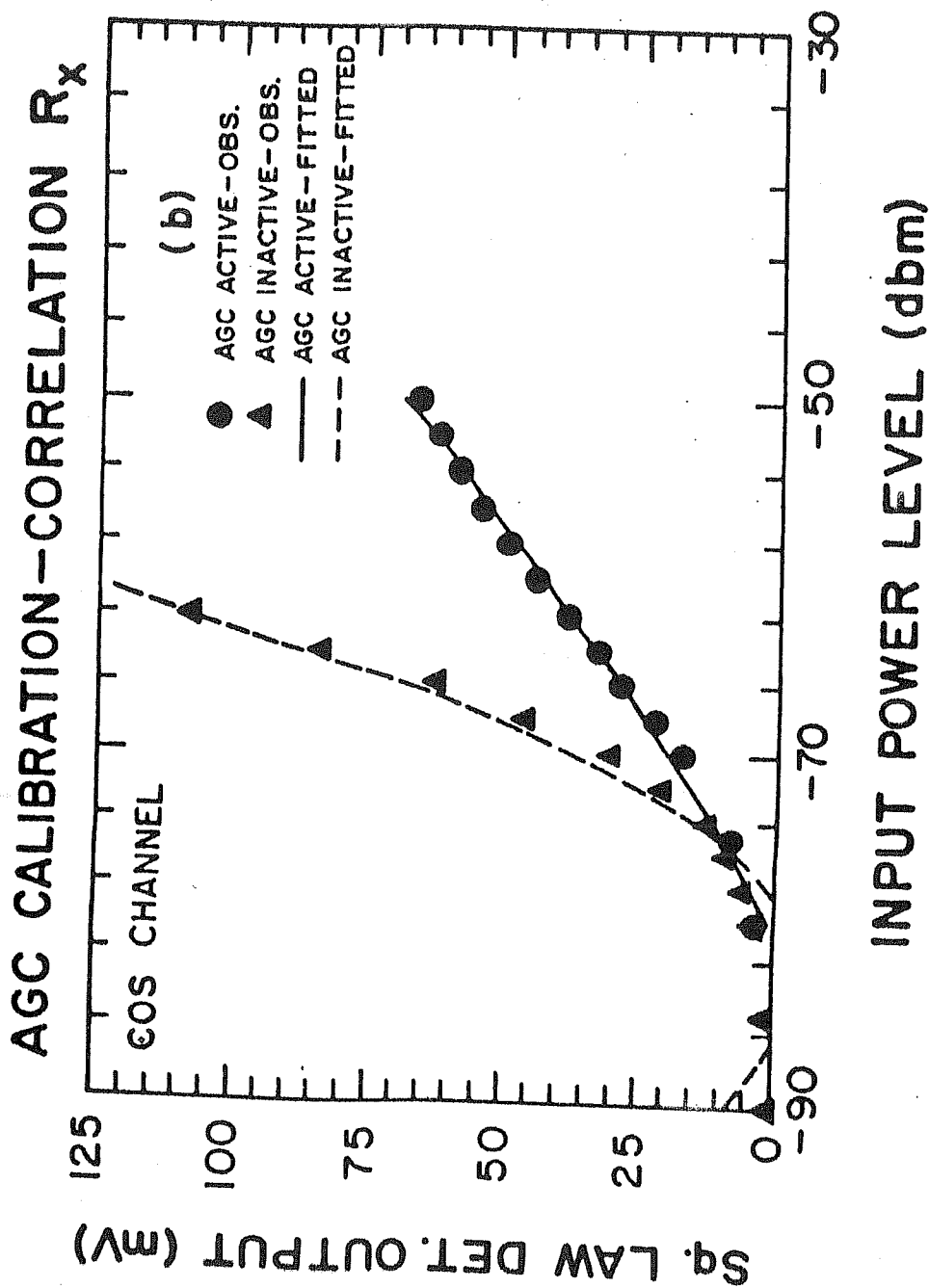


Figure 3.6a Shows the behaviour of the square law detector output for the Sin channel with and without the automatic gain control (AGC) active, for changing input power levels. The filled triangles and circles are the measurements while the solid and broken lines are 2nd order polynomial fits.



**Figure 3.6b** Shows the behaviour of the square law detector output for the Cos channel with and without the automatic gain control (AGC) active, for changing input power levels. The filled triangles and circles are the measurements while the solid and broken lines are 2nd order polynomial fits.

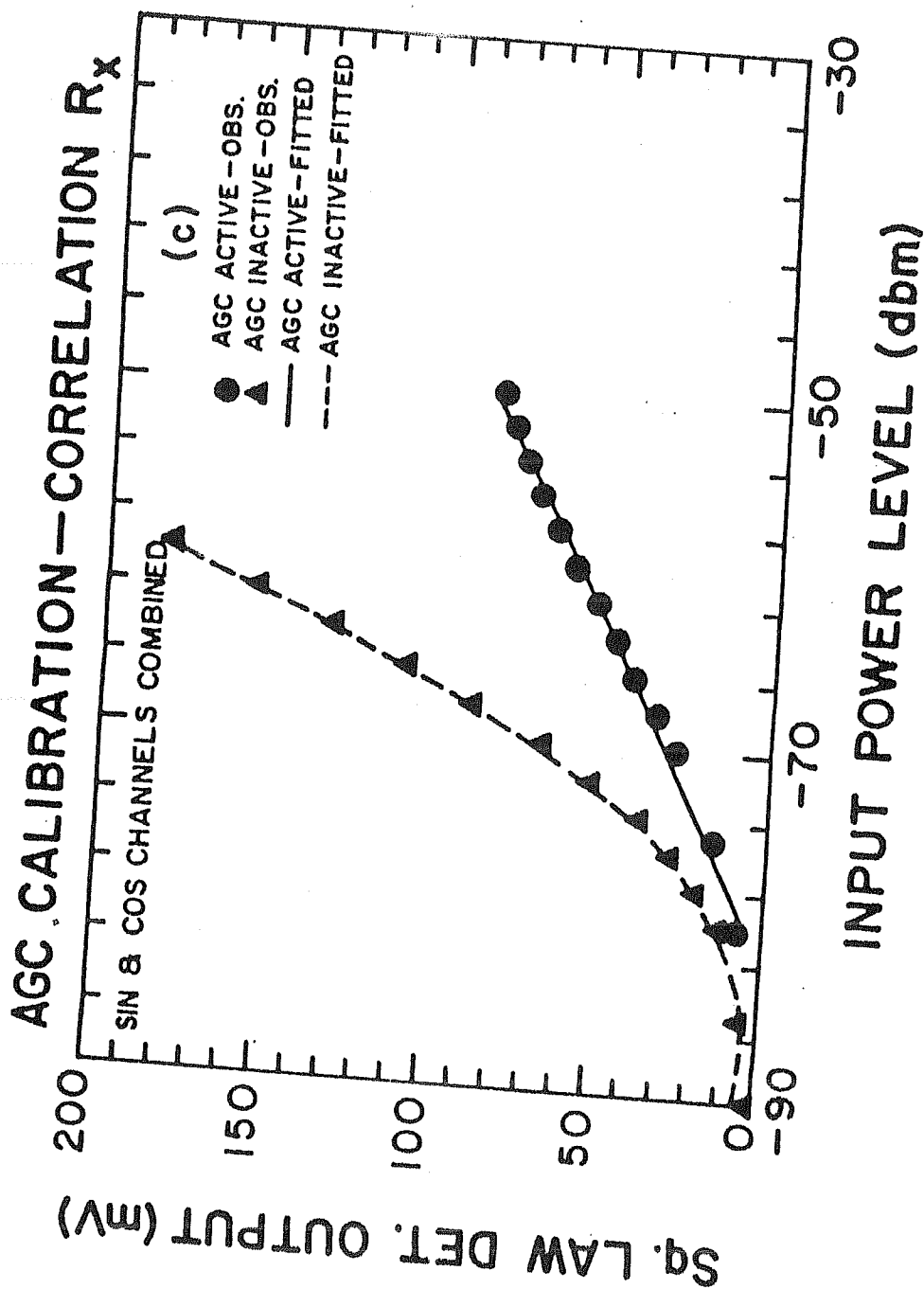


Figure 3.6c Is similar to Figure 3.6a and Figure 3.6b with the square law detector output representing the effective output given by  $\sqrt{\sin^2(\text{def.}) + \cos^2(\text{def.})}$ .

with the antenna array connected and a source in the beam the square-law output remains below 45 mV. Figure 3.6a-3.6b shows the behaviour of the Sin and Cos channels with and without the AGC in operation while Figure 3.6c plots the same outputs using the effective output given by  $(\text{Sin}^2 + \text{Cos}^2)^{\frac{1}{2}}$ .

For uncorrelated signals the outputs of the difference amplifiers remain zero while correlated signals produce output voltages at the Sin or Cos channel or at both depending on the relative phase of the input signals. This is because in a correlation receiver, the time-averaged product of the voltages in the two IF branches of the Sin and Cos channels becomes zero for uncorrelated signals and greater than zero for correlated signals. The square-law modulated signal at the switching frequency is converted to sine-wave by an active filter circuit and phase-detected in synchronization with the phase-switch. The Cos and Sin channels are then recorded on a strip chart and also on a digital magnetic tape after analogue to digital conversion.

### 3.3.1 The Scintillometer.

When a scintillating radio source is observed by a phase-switching interferometer, its output consists of three main components. The first is a broadband system noise voltage covering a frequency range from zero to a higher cut-off determined by the receiver time constant. The second is a slowly varying voltage due to the passage of the source

# BLOCK DIAGRAM OF TOTAL-POWER SQUARING SCINTILLOMETER

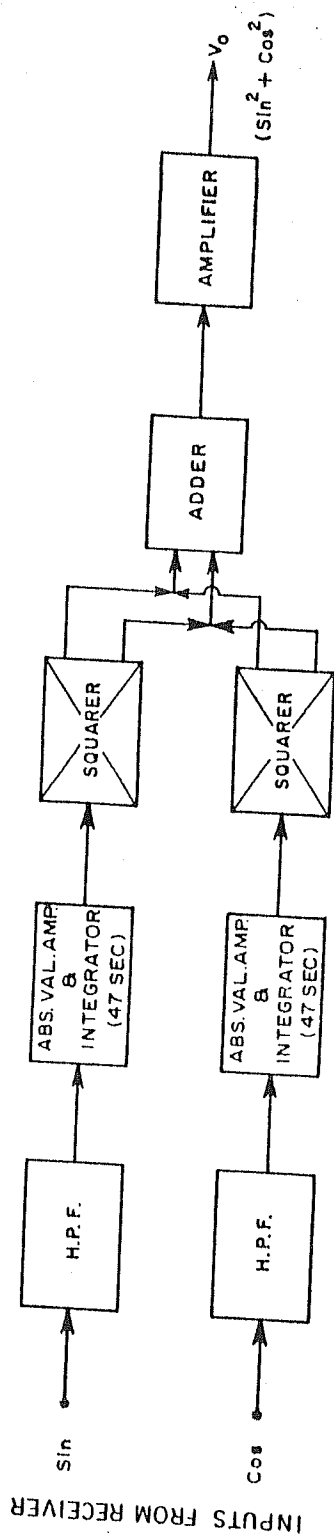


Figure 3.7 Shows a block diagram of the total power squaring scintillometer unit.

through the interference pattern of the telescope. Its frequency spectrum depends upon the dimensions and spacings of the antenna elements, the operating wavelength  $\lambda$  and the declination  $\delta$  of the source (Duffett-Smith, 1976). The third component is a rapidly changing voltage due to scintillations. It has a noise-like character and its frequency spectrum depends on existing conditions in the solar-wind, the apparent angular diameter of the source, the solar elongation and parameters of the receiver like bandwidth and time constant.

This rapidly varying signal is of interest in an IPS study and is detected using a unit called the scintillometer. Figure 3.7 is a block diagram of the scintillometer. The Sin and Cos signals are fed to the inputs of the scintillometer where the fluctuating signals are filtered by a bandpass filter, averaged over a long time constant of 47 seconds, squared and added to produce a deflection proportional to the square of the scintillating flux modulated by the square of the antenna pattern. The output is recorded on a third channel, on the strip chart recorder.

### 3.3.2 Sensitivity of the Telescope.

The system noise temperature is the sum of two parts and is given by

$$T_{\text{sys}} = T_{\text{sky}} + T_{\text{R}}$$

where

$T_{\text{sky}}$  = Equivalent noise temperature of the galactic background.

$T_{\text{R}}$  = The noise temperature of the receiver.

$T_{\text{R}}$  is, in turn, given by the expression

$$T_{\text{R}} = (N-1) T_{\text{o}}$$

where

$N$  = Noise factor of the preamplifier.

$T_{\text{o}}$  = Ambient temperature.

At VHF frequencies the equivalent noise temperature of the galactic background is a few thousand degrees Kelvin depending on the position of the source with respect to the galactic plane and the galactic center. This is generally much larger than the noise temperature of the receiver at VHF. The sensitivity of the receiver thus becomes sky noise limited. Thus at VHF frequencies optimizing aperture efficiency is of utmost importance. Large dipole arrays made of open wire transmission lines are generally almost 70% efficient, with the losses being mainly due to having an incompletely filled aperture, end effects, decorrelation of signals over long rows of dipoles and mismatch.

The sensitivity or minimum detectable flux of a radio telescope is given (Kraus 1966) by

$$\Delta S_{\min} = \frac{2 k \Delta T_{\min}}{A_{\text{eff}}}$$

where

$\Delta T_{\min}$  = Minimum detectable noise temperature of the receiver.

$k$  = Boltzmann Constant.

$A_{\text{eff}}$  = Physical area of the telescope multiplied by the aperture efficiency.

$\Delta T_{\min}$  for a correlation type receiver is given by

$$\Delta T_{\min} = \frac{1}{\sqrt{2} \cos \phi} \frac{T_{\text{sys}}}{\sqrt{B \tau}}$$

where

$T_{\text{sys}}$  = System noise temperature of each receiver.

$B$  = Bandwidth.

$\tau$  = Integration time constant.

$\phi$  = Phase angle between the receiver inputs and IF output signals.

For  $\phi = 0$ ,  $\tau = 0.1$  sec,  $B = 4.5$  MHz and taking  $T_{\text{sys}}$  to be about  $2000^\circ \text{K}$  at 103 MHz we get

$$\Delta T_{\min} \approx 2^\circ \text{K}.$$

If we now assume an ideal situation where the aperture efficiency ( $\eta$ ) is 0.8 then the sensitivity  $\Delta S_{\min}$  turns out to be  $\approx 3.6$  Jy at a signal-to-noise ratio of five.



A rough estimate of the signal-to-noise ratio and the sensitivity of the system can be made by studying the chart recordings of a strongly scintillating radio source. Plate 2 shows some typical chart recordings of the source 3C48 in March 1988, just prior to the expansion of the aperture to 20,000 m<sup>2</sup>. The three recordings shown indicate how the scintillation can vary from day to day. The first two recordings from the left show how the scintillation is reduced at large solar elongations ( $\epsilon$ ) with both Sin and Cos channels showing reduced levels of scintillation for larger elongations. The third recording shows scintillation on only the Cos channel indicating that the apparent position of the source in the beam has changed. This phenomenon is well understood (Okoye & Hewish, 1967) and is caused by large scale ( $\geq 10^3$  km) density inhomogeneities in the ionosphere, which produce large phase-gradients across the wavefront of an incoming radio signal. This causes the distortion of the scintillating pattern itself. In the present case, since only the Cos channel has shown scintillation, the source has been shifted by refraction to the peak of the Cos fringe within the beam. Hence the entire flux of the source is realized in the Cos channel itself giving no deflection on the Sin channel.

Each large square grid on the photo represents 5 mm on the actual chart. The peak-to-peak variation in the background trace of the Cos channel is thus about 2.5 mm giving an rms variation of  $\frac{2.5}{2\sqrt{2}} = 0.88$ . The mean DC shift in the Cos channel is about 17 mm. If this deflection is corrected for the effect of the AGC it will correspond to a deflection of 32.5 mm. Thus the signal to noise ratio will be  $\frac{32.5}{0.88} = 36.93$ . The source 3C48 has a flux at 103 MHz of 61.4 Jy. Thus the minimum detectable flux in this case

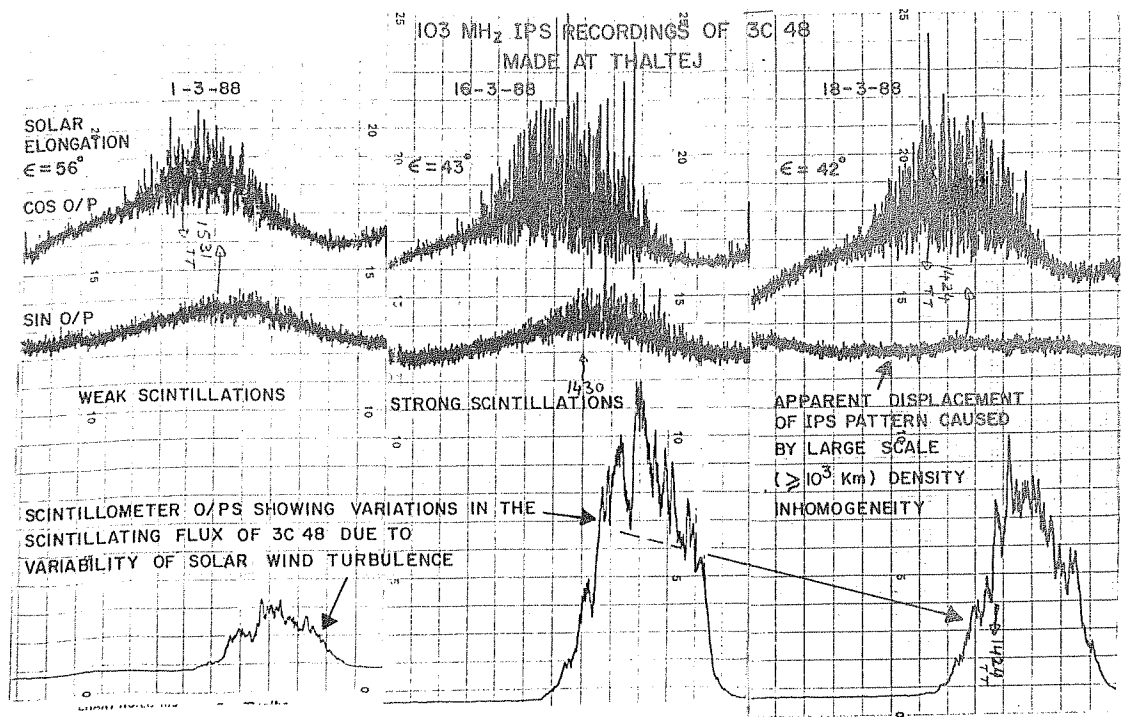


Plate 2 Shows some typical chart recordings of the source 3C48 in March 1988. The three recordings shown are the sin, cos and scintillometer channels of the chart recorder and they indicate how the scintillation varies with solar elongation and from day-to day.

would be  $\frac{61.4}{36.93} = 1.66$  Jy. Using this value in the formula for the minimum detectable flux, the value of the aperture efficiency ( $\eta$ ) can be determined. The efficiency turns out to be  $\approx 0.49$ . This aperture efficiency is far below what is expected for dipole arrays which can normally be made around 65 to 75% efficient. Using this value of aperture efficiency the sensitivity of the Thaltej telescope turns out to be around 6 Jy at a signal to noise ratio of five.

The sensitivity of the scintillometer unit to scintillations (Duffett-Smith, 1976) is given by

$$\Delta S_{\min} = 4 \frac{K T_N}{\eta A} \left( \frac{1}{\tau_1 \tau_2 (\Delta \nu)^2} \right)^{\frac{1}{4}}$$

where

$\Delta S_{\min}$  = rms value of scintillating flux density.

$T_N$  = System noise temperature.

$\eta$  = Aperture efficiency.

$A$  = Physical area of antenna array.

$\tau_1$  = 0.1 sec - time constant of SIN and COS integrators.

$\tau_2$  = 47 secs - scintillometer time constant.

$\Delta \nu$  = Overall (-3 db) bandwidth of IF amplifiers.

Using the above expression the sensitivity of the scintillometer works out to be about 0.71 Jy.

With a  $10,000 \text{ m}^2$  dipole array similar to the one at Thaltej one would expect to see between 30 and 40 scintillating radio sources on a regular basis. In reality, observations carried out with the antenna between mid-1984 and end of 1987 showed only around 18 scintillating radio sources on a regular basis. Figure 3.8 is a plot of the positions of the various scintillating sources seen by the Thaltej telescope in ecliptic coordinates. One of the reasons for the discrepancy is the effect of the AGC. Figure 3.9 shows a plot of the effective deflection  $(\sin^2 + \cos^2)^{\frac{1}{2}}$  for several scintillating sources seen by the telescope as a function of the flux at 103 MHz. The effective deflection for each source was calculated by averaging the DC deflections of a large number of observations for each source, and Table 3.4 gives a list of the sources with their flux and the number of observations averaged for each source. An attempt was made to select as many weakly and non-scintillating sources as possible because the deflections would then be easier to measure accurately. The empty circles in Figure 3.9 represent data for which the AGC is active while the empty triangles represent the same data with the AGC inactive. The lines through the data points are straight line fits. It can be seen that the AGC can reduce the signal to noise ratio drastically and all the recordings must be corrected for the effects of the AGC, as not doing so would lead to an overestimation of the scintillation index.

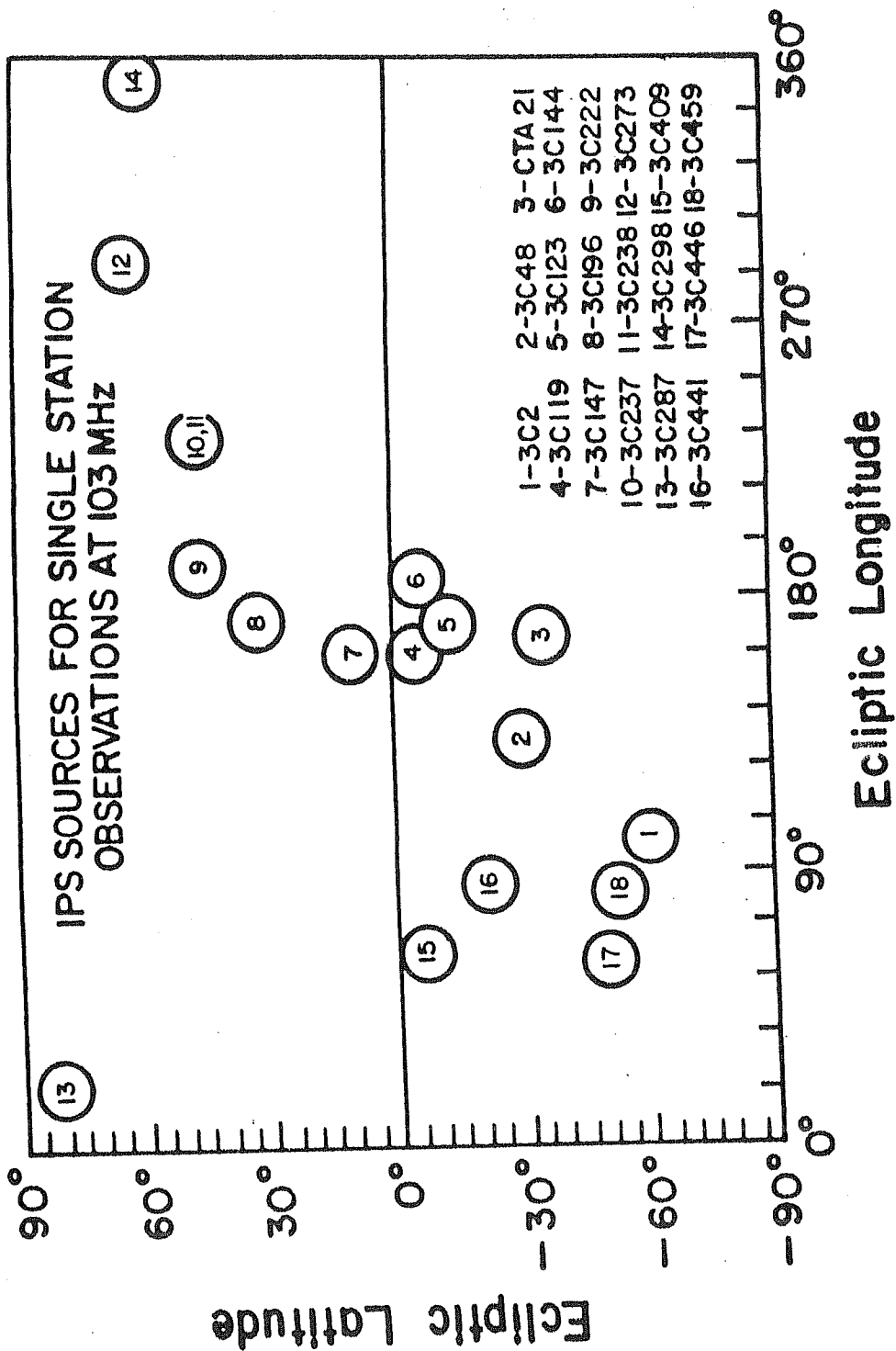


Figure 3.8 Shows the positions, in ecliptic coordinates, of the sources observed from Thaltej.

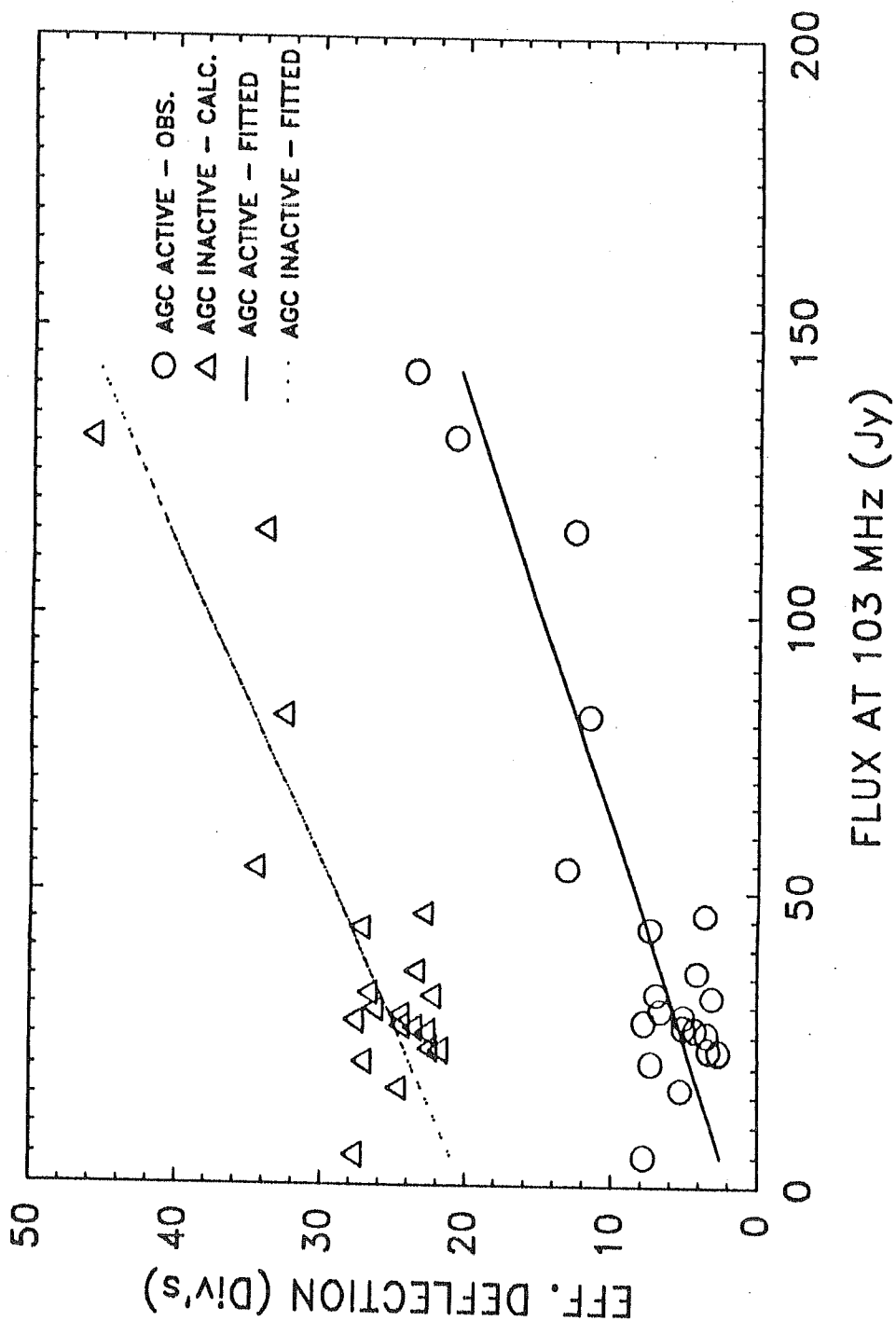


Figure 3.9 Shows a plot of the effective deflection  $\{ \sin^2(\text{def}) + \cos^2(\text{def}) \}^{\frac{1}{2}}$  Vs. Flux, as seen with and without the Automatic Gain Control (AGC) in operation.

**Table 3.4:** SOURCES USED TO MEASURE THE DEFLECTION AS A  
FUNCTION OF FLUX 103 MHz

Source	Flux 103 MHz.(Jy)	No. of Obs.	Source	Flux 103 MHz.(Jy)	No. of Obs.
3C2	28.40	22	3C237	36.10	41
3C47	54.20	5	3C238	32.20	11
3C71	26.30	2	3C270.1	27.40	7
3C84	130.90	2	3C273	142.30	73
CTA21	10.00	54	3C286	29.40	2
3C119	20.80	19	3C287	26.60	10
3C153	25.60	7	3C298	81.40	85
3C175	46.10	3	3C324	23.00	8
3C196	114.90	84	3C368	31.70	4
3C222	16.30	43	3C459	43.60	86

### 3.3.3 Decorrelation.

The Butler matrix requires RF signals from the antenna array to arrive at its inputs with equal phase and gain. Since the underground cables from each line section of the antenna array were of unequal lengths, equal gain at the input ports of the Butler matrix was attained by having different preamplifier gains for each line, using a gain control in the LNA's (See Figure 3.3), and the phases were equalized by trimming or adding on required cable lengths.

The fact that the antenna was not realizing its optimum sensitivity led to a complete check of all the subsystems and the cause was finally narrowed down to bandwidth decorrelation due to the unequal lengths of RF cables used. The experimental setup used to confirm this consisted of a simple interferometer formed by a single dipole cut to 103 MHz and a single line section of the antenna array. The separation between the two elements of the interferometer was around 50 m. The setup was such that the cable from the single dipole to the receiver was equal in length to the underground cable length of the central 32nd (shortest) line of the array.

With such a setup, the transit of a strong source like 3C461(Cas A) would be expected to give the same output voltage, measured as deflections on the Sin and Cos channels of the correlation receiver, irrespective of the particular line section of the antenna used. It was found that the effective deflection  $(\text{Sin}^2 + \text{Cos}^2)^{\frac{1}{2}}$  measured was less by a factor of five when the line



**Table 3.5: INTERFEROMETRIC OBSERVATIONS OF 3C461 (Cas A) WITH EQUAL AND UNEQUAL PATH LENGTHS FOR RF SIGNALS**

Interferometer Cable Lengths in Meters Between		Array Section Number	Deflection in Arbitrary units
Array Section and $R_X$	Single Dipole and $R_X$		
135	50	1	1.8
50	50	32	8.94
135	135	32	8.74

line section used in the interferometer was the Northernmost (longest) line as compared to the deflections produced by the central (shortest) line. Table 3.5 summarizes the results of this experiment.

It is clear from Table 3.5 that the cause of the loss in sensitivity was the decorrelation of the signals at the correlation receiver. For signals to be efficiently detected by a correlation receiver they should arrive at the receiver within a time  $T = \frac{1}{\Delta\nu}$  of the first signal arriving. Here  $\Delta\nu$  is the IF bandwidth and is equal to 4.5 MHz. The correlation time for the receiver is thus 0.22  $\mu$  sec. The travel time of an RF signal along the longest cable length (135 m) is 0.68  $\mu$  sec using a velocity factor of 66% for RG8/U cables. Thus, within the correlation time of 0.22  $\mu$  sec the RF signals would have only covered a distance of approximately 44 m corresponding to about 17 lines on either side of the central line. Thus almost half the antenna array was not contributing to the receiver output thereby severely affecting the sensitivity of the array. This problem could only be rectified at all the three sites in mid-1988 when the Thaltej array was being expanded to 20,000 m<sup>2</sup>.

### 3.4 The 20,000 m<sup>2</sup> Array.

The objectives of the telescope were expanded at the end of 1987 to include the study of large-scale travelling interplanetary disturbances (Gapper *et al.*, 1982). In this method, the scintillation index ( $m$ ) of a large number of scintillating radio sources (typically 1000 to 1500), in all directions around the sun, are continuously monitored and since  $m$

depends on the scattering power of the medium along the line of sight to the source, interplanetary disturbances appear as unusually high or low values of  $m$  compared to the mean. Using this method daily "weather" maps of the interplanetary medium, called g-maps, may be made. Such g-maps enable one to track large regions of enhanced turbulence moving out from the sun and provide a ground-based technique to detect such disturbances at least five days before they reach the earth. This is a predictive ability which remains unattainable in any other technique. To facilitate such a study, the physical area of the Thaltej array was enhanced to  $20,000 \text{ m}^2$ . The expanded array began limited operation in early 1990, and the observations of enhanced scintillations due to comet Austin (Janardhan *et al.*, 1991 a) in May 1990 were carried out with it. While the  $10,000 \text{ m}^2$  array was operated using only one receiver connected to a single beam during a given observation, it was planned to make use of all 32 beams of the array simultaneously in the  $20,000 \text{ m}^2$  configuration. This can be achieved by having 32 receivers connected at all times to the 32 independent beams, thus scanning the whole sky available to the telescope everyday. The receivers used are to be total power receivers with a bandwidth of 1.5 MHz. At the time of the observations of comet Austin, though, none of the receivers were ready thus the observations were made with the correlation receiver. The cable lengths had all been equalized but the entire work of matching the impedances of the enlarged lines to the preamplifiers by using a single 'Christmas-tree' branch to tap the outputs of each line was still underway. Figure 3.10 is a block diagram of the system after expansion to  $20,000 \text{ m}^2$ .

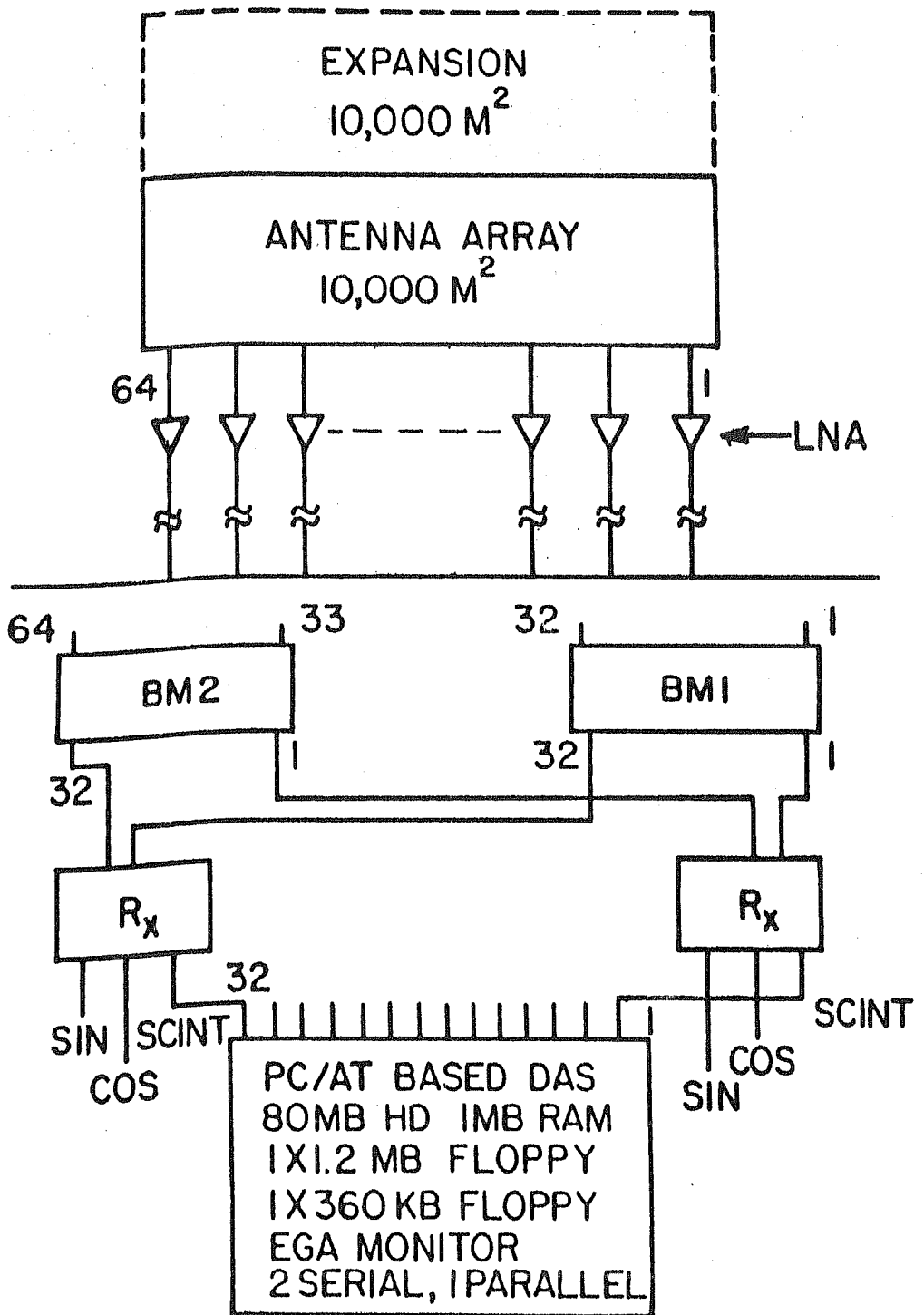


Figure 3.10 Block diagram of the IPS telescope at Thaltej after expansion of the collecting area of the array to 20,000 m<sup>2</sup>.

The data acquisition system was also changed to a 32 channel PC/XT based DAS with the control circuits replaced by a Z-80 microprocessor. This would facilitate simultaneous observations of sources in the entire sky available to the telescope. The observations of scintillations due to comet Austin (1989 c1), though carried out at reduced sensitivity, were successful as will be seen in the fifth chapter.

### 3.5 The Digital Data Acquisition System

The two inputs Viz. the Sin and the Cos derived from the correlation receiver are recorded on a strip-chart along with the scintillometer output. But in order to analyze the data it must be available in digital form. This is achieved by using an Analogue-to-Digital Converter (A/D C) and then recording the digital information on magnetic tape using a digital magnetic tape recorder. The tapes can then be analyzed on a computer as required. The data from the correlation receiver has a band limited output upto 10 Hz (IPS typically lies in the range 0.1 to 10 Hz). The simple integrator serves as a low pass filter and hence no special digital filter is used. The magnitudes of the signals on the two channels depend upon the position of the source on the receiver fringes of the interferometer formed by the North and South halves of the antenna array.

Figure 3.11 shows a block diagram of the data acquisition system indicating most of the input/output (I/O) signals (Bobra *et al.*, 1981;

# BLOCK DIAGRAM OF AUTOMATIC DATA ACQUISITION SYSTEM

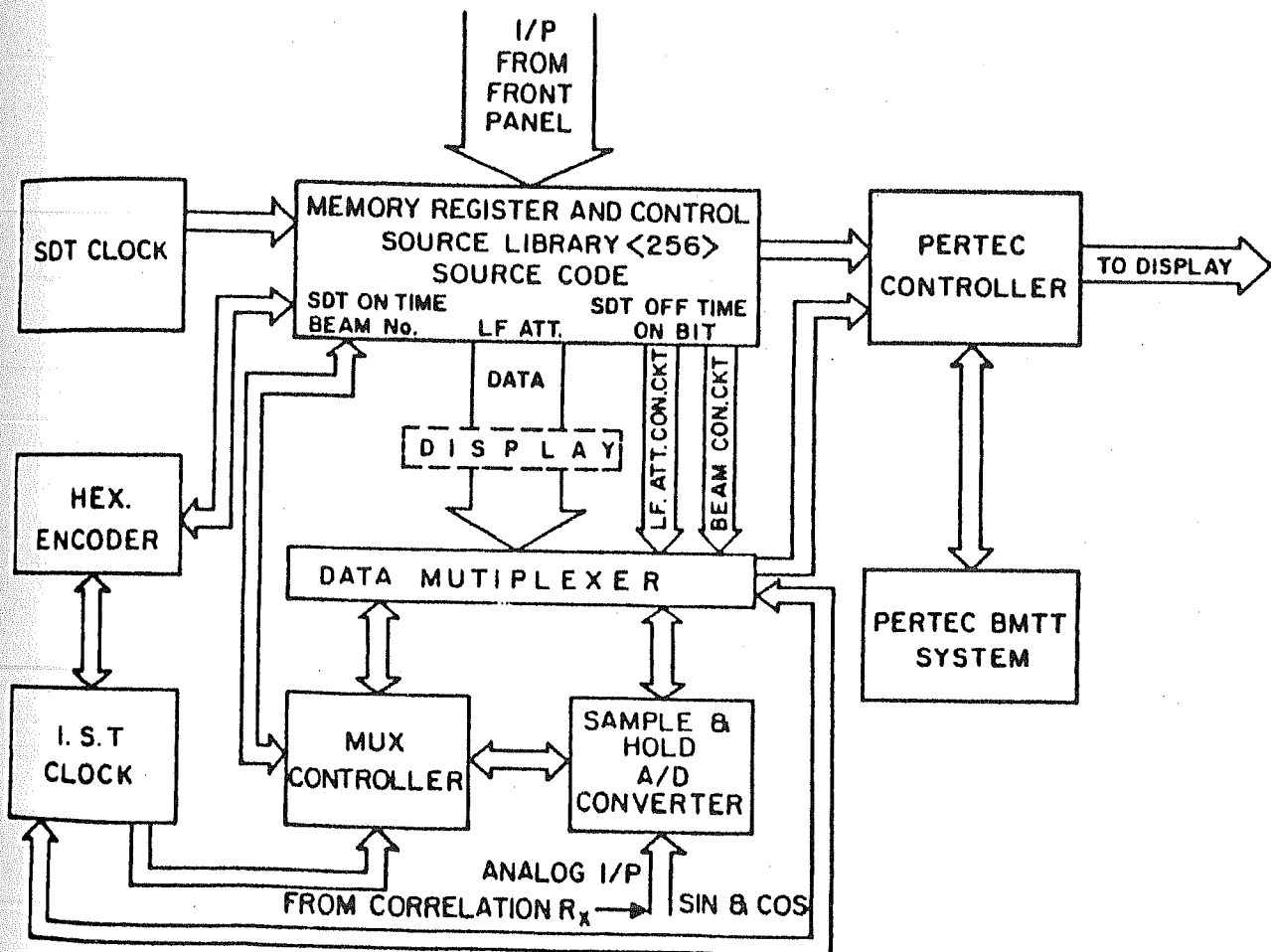
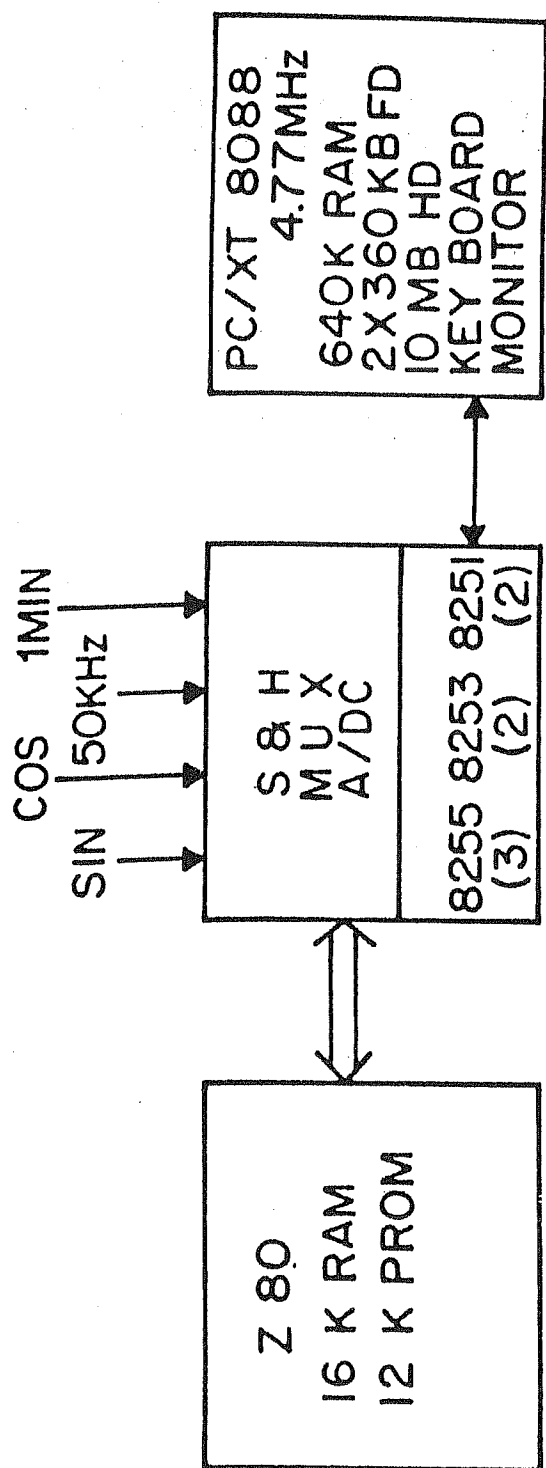


Figure 3.11 Shows a block diagram of the automatic data acquisition system used with the 10,000 m<sup>2</sup> array indicating most of the input/output (I/O) signals.



## Z 80 + PC / XT BASED DAS

- 8255 – PROGRAMMABLE PERIPHERAL INTERFACE
- 8253 – PROGRAMMABLE INTERVAL TIMER
- 8251 – PROGRAMMABLE COMMUNICATION INTERFACE

Figure 3.12 Block diagram of the new PC/XT based Data Acquisition System (DAS) for future g-map work.

Alurkar *et al.*, 1982 ). This system comprises a source library, hex encoder, control circuit, analogue to digital converter, data multiplexer, mux controller and a pertec controller.

Figure 3.12 shows a block diagram of the new PC/XT based DAS which has been recently developed. It has a Z-80 microprocessor board with a 16 K RAM and a 12K PROM with the DAS card having the sample and hold analogue to digital converter and other circuits. The PC/XT has a 8088 CPU, a 640 K RAM, a 10 MB hard disk and floppy drive. The Z-80 and PC/XT are connected by an RS-232 interface. The IST clock is connected to the Z-80 CPU board which in turn synchronizes the internal clock of the Z-80.

### 3.5.1 Source Library.

A source library is provided in the system, and stored in RAM. Each source has a 40-bit information Viz. SDT ON TIME (Siderial on time) SDT OFF TIME, BEAM CODE, LOW FREQUENCY (LF) ATTENUATION and ON-BIT. Each source is given a source code starting with  $00_H$   $FF_H$ . This provides flexibility of observing time and can be programmed on either a daily, weekly or monthly basis as per the requirements of the observer. The ON-bit decides which of the sources from the stored memory are to be observed (For sources to be observed this bit has a value 1). This could be changed in the MODIFY mode in which



only the ON-bit is changed; all the other information remains the same. The 40-bit data available on RAM output is displayed on the DISPLAY.

### 3.5.2 Hex Encoder.

This sub-system provides the necessary decoded data from the Hex keyboard to the memory address circuit for storing the information to the RAM library in the MANUAL/WRITE/NOT MODIFY/NOT RUN mode (called WRITE-mode) of operation of the DAS. In the AUTO/READ/NOT MODIFY/RUN mode (called the RUN mode) the HEX ENCODER provides data for scanning the RAM address at the rate of 100 Hz. The basic input is derived from the 1 KHz pulse of an Indian Standard Time (IST) clock which is stable to  $\pm 5 \times 10^{-10}$ . This is achieved by using a highly stable oven-controlled crystal oscillator whose output is about 200 mV rms (sinusoidal) at a frequency of 10 MHz. The output is first converted to TTL compatible levels and then fed to a chain of decade counters and a programmable synchronous counter.

### 3.5.3 Control Circuit.

This circuit converts the SDT serial data to parallel data and provides 'Hours and Minutes' information to the comparators as one output (say A input). The other input (say B input) is from the RAM output. The comparators compare the two inputs A and B (each being

equal to 16 bits) and when SDT clock equals RAM SDT ON time output, it generates various pulses. These pulses in turn lock the Hex encoder output to the source and the data is then displayed. The SDT clock input (i.e. A input) is then up-dated. It generates another set of pulses, when the SDT clock equals the SDT off-time output of the RAM, using another set of comparators. The Hex encoder then starts again in the search or scanning mode to look for the next source to be observed.

### **3.5.4 The Analogue-to-Digital (A/D) Converter.**

The Sin and Cos receiver outputs, each in the range of  $\pm 5$  volts, need to be recorded on a magnetic tape after analogue to digital conversion. To satisfy the Nyquist criterion, the data is sampled at a frequency of 20 Hz. Since the data is contained in both the Sin and Cos channels it is necessary to sample both the Sin and Cos outputs simultaneously. A sample-and-hold circuit along with an analog multiplexer is used for this purpose.

Once the data is sampled, it is supplied to an A/D converter (DATEL model EH12B1) one after another using an analogue multiplexer. Necessary control pulses are generated by the multiplexer (MUX) Controller. Although the time available to record the data on tape is about 50 msec, this operation should be completed in as short a time as possible. The data selection and recording is completed in less than 16 msec. The 12-bit data are split into bins of 6 bits in order to make the data-recording

symmetric and to have ease of data-retrieving in the computer. The 12-bit data of SIN and COS outputs are available on the 6-bit output bus one after another.

### 3.5.5 Mux-controller.

This sub-system provides all the necessary pulses required for analogue signal processing and digital data recording. It provides, on receipt of a command from the control circuit, various pulses for operations like sample hold, selecting the analogue multiplexer A or B, selecting SIN or COS bytes (6-bit a byte) recording SIN or COS bytes (6-bit a byte) to the other sub-system. It also provides the address to the data multiplexer.

### 3.5.6 Data Multiplexer.

This is a digital multiplexer which first converts the serial IST time to parallel time data bits. Other system status is also available along with the station code and the synchronizing word (00 0F 0F<sub>H</sub>). The parallel data are first converted into 8-bit parallel bytes and then into a 1-bit serial data. This 1-bit serial status information is the least significant bit in the 8-bit-byte data being recorded on to a magnetic tape. The total length of the status information is 128-bit and, therefore, with every 128 bytes (8-bit a byte) recorded on tape, we get complete status information.

### 3.5.7 Pertec Controller.

This provides the necessary input/output to a PERTEC Buffered Magnetic Tape Transport (BMTT) system. The 6-bit of SIN/COS data from the A/D converter are placed as most significant bits (MSB) combined with 1-bit of status information as Least Significant Bit (LSB) to form 8-bit-a-byte data. The remaining bit is always zero. This arrangement also helps in decoding the status information. If the byte value is odd, the status bit is one, or else it is zero. Within the byte the 4 MSB bits represent unit digit.

The status information is recorded as follows:

- 6 bytes - msec first - IST time
- 1 byte - station code - C1 - Ahmedabad  
D2 - Rajkot  
CD - Surat
- 1 byte - source code
- 1 byte - low frequency attenuation
- 1 byte - beam code
- 2 byte - SDT ON time
- 4 byte - sync word 00FF 0F0F

The controller generates various commands viz. FEN, GO, etc.. necessary to initiate the operation of the BMTT system. It also displays various tape transport and formatter status (Bobra *et al.*, 1981; Alurkar *et*

*al.*, 1982). The BMTT is operated in a split buffer mode. Data is sent to the buffer (say A) byte by byte (4 bytes for each data sample) and when the buffer is full, the data is recorded on tape. While the data is being recorded on tape, the data from the DAS is sent to another buffer (say B). Usually each buffer length is about 1024 bytes and therefore it takes about 12.288 seconds to switch the buffer. Necessary logic conversion is also done by this sub-system to match with the BMTT logics.

During operation of the system the source library is first entered in the WRITE mode. The on bit at this stage is zero. Once the library is entered, the system is put in the MODIFY mode (MANUAL-WRITE-MODIFY-NOTRUN).. The on bit is now stored as Logical one (High), only for the sources to be observed. Now the system is ready for observation and the system is kept in the RUN mode. The system now scans the RAM data while the DAS is waiting for the Sidereal on time (SDT ON) of the clock to become equal to the stored SDT time of the sources to be observed. The system disregards sources which are not to be observed. When the stored SDT time of an observation matches the the time on the SDT clock, an ON pulse is generated which locks the source data on to the display. The system then generates 20 Hz sampling pulses together with pulses required for sample-and-hold, analogue multiplexer, start conversion and 1st and 2nd byte of Sin and Cos. The status data multiplexer pulses are also generated to convert the data into 1-bit serial form which finally are recorded on a magnetic tape. The system, while in operation, also keeps track of the SDT OFF time and a sequence of pulses are generated to close the operating session when the stored SDT off time matches the SDT time

on the clock. The system also generates the necessary command to the BMTT and puts a file mark on the tape. The system now gets back to the search mode looking for the SDT ON time of the next observation.

Due to the expanded  $10,000 \text{ m}^2$  array and the two  $5,000 \text{ m}^2$  working at reduced sensitivity as already discussed, the number of scintillating radio sources that could be monitored by the three site network was limited by the sensitivity of the two outstations. Fourteen strongly scintillating radio sources were regularly monitored between mid-1984 and end of 1987 using the Thaltej array and the results of the study will be taken up in the next chapter.

# Chapter - IV

## MEASUREMENTS OF ANGULAR SOURCE SIZE AND INTERSTELLAR SCATTERING AT 103 MHz

### 4.1 Introduction.

The best technique available for measuring the angular diameters of compact radio sources is interferometry. It is also the most widely used technique. The angular resolutions achieved by this method simply depend upon the ratio  $\lambda/d$  where  $d$  is the baseline separation and  $\lambda$  is the operating wavelength. Radio telescopes generally being very large physically, have very large mechanical support structures and the baselines are usually fixed. Thus to achieve higher and higher angular resolutions one has to observe at shorter and shorter wavelengths. It is thus only natural that measurements of angular diameters of compact radio sources at meter wavelengths (Resch, 1974; Vandenberg, 1974) have been limited,

with most of the measurements being carried out at centimeter wavelengths (Spangler *et al.*, 1986; Fey *et al.*, 1991).

IPS observations at meter wavelengths offer an ideal method of studying the angular diameters of compact radio sources. Ideally information about the squared magnitude of the visibility function can be determined from a complete set of IPS spectra obtained in strong scattering, with each observation being a cut across the visibility function in the direction of the solar wind velocity vector. A large number of such observations could thus be used to get a complete picture of the source with only the phase information being absent in the complex visibility function. The reason why such a method is not feasible is because many sources, due to their positions, do not approach close enough to the sun to be in the strong scattering regime and many sources which do pass close to the sun, do so for very short periods. Also the scintillation index (rms flux/mean source flux) decreases rapidly as the source visibility function begins to cut off the IPS spectrum, causing many sources to be unobservable in this period. Radio interference from the sun can also effectively wipe out meaningful observations in a large number of cases. Moreover the source visibility function depends upon the intrinsic character of the source and the scattering properties of the plasma along the line of sight to the source and it is in general difficult to separate the two effects. Only in the case of very compact sources like pulsars which can be taken to be ideal "point sources", the observed angular diameter will be completely dominated by scattering only and the form of the visibility function can be determined by the shape of the spectrum of electron density irregularities in the



interstellar medium. The bulk of previous scattering experiments in the Galaxy have been made mostly by pulsar pulse broadening and decorrelation measurements (Cordes, Weisberg and Boriakoff 1985; Alurkar, Slee and Bobra, 1986).

One method of measuring angular diameters using IPS would be to compare the width of the power spectrum in weak scattering (Cohen, Gundermann, and Harris, 1967; Rao, Bhandari and Ananthakrishnan, 1974) or strong scattering (Kaufman, 1976) with that of a point source. The recent method of fitting model IPS power spectra (Manoharan and Ananthakrishnan, 1990) to determine solar wind velocities can also be used to estimate angular diameters of radio sources.

Due to its simplicity, the Gaussian model visibility function has been widely used in determining radio source structure. But in this case the true visibility function is severely limited causing both low frequency VLBI and IPS techniques to suffer from this. Hence the absence of an *a priori* knowledge of the true brightness distribution causes one to assume circular symmetry and approximate the real source profile by a Gaussian having a characteristic width to  $1/e$ , leading to the calculation of the source diameter. In the present study too the angular diameters of fourteen radio sources were calculated using the assumption of a Gaussian brightness distribution and observations of the variation of scintillation index ( $m$ ) with solar elongation ( $\epsilon$ ).

The assumption of a circularly symmetric Gaussian model for the compact component of a radio source is valid and it has been shown (Little and Hewish, 1966) that provided the source model does not contain more than one component or is not greatly elongated in a particular direction the method yields the same result and is insensitive to the type of model used. The angular size measurements, though, are all subject to errors due to broadening by interstellar scattering (ISS) which, in general, causes the true source brightness distribution to tend towards a symmetrical Gaussian model. Recent scattering observations (Dennison *et al.*, 1984; Cordes, Weisberg, and Boriakoff, 1985; Alurkar, Slee, and Bobra, 1986; Cordes *et al.*, 1988; Fey, Spangler and Mutel, 1989) have shown that the electron density turbulence in the interstellar medium (ISM) consists of a smooth component with a uniform Galactic distribution and a clumped component confined mainly to the Galactic plane. The scattering has also been shown to peak towards the Galactic center. IPS measurements of angular diameters based on the Gaussian model have been carried out (Harris, Zeissig and Lovelace, 1970; Readhead and Hewish, 1972; Cohen and Cronyn, 1974; Duffett-Smith and Readhead, 1976) and used to derive an approximate formula for the interstellar scattering angle ( $\Theta_s$ ) at a given frequency.

In the present study, using the 10,000 m<sup>2</sup> array described in chapter 3 an attempt was made to determine the value of  $\Theta_s$  at 103 MHz, based on the measurements of angular diameters of fourteen compact radio sources. Since the telescope was operating with reduced sensitivity, due to problems of decorrelation across the receiver bandwidth, the number of scintillating

radio sources observable was small. Moreover, there was a bias towards choosing the strongest scintillators for the study because it is for these sources that diameters are determined with the best accuracy. Unfortunately, the strongest scintillators are the most compact sources and this selection effect would reduce the measured interstellar scattering especially when dealing with a small sample of sources. Nevertheless, the regular measurements of scintillation index of different sources over several years have led to measurements of angular sizes of fourteen radio sources and to the measurement of ISS at 103 MHz. It has also brought out the long term behaviour of the Thaltej array.

## 4.2 The Method of Source Diameter Measurements Using IPS.

Essentially the method of determining source sizes by using IPS is based on the systematic variation of scintillation index ( $m$ ) of a compact radio source with solar elongation ( $\epsilon$ ). At large  $\epsilon$  the scattering is weak and  $m$  is small, but as one approaches the sun the scintillation index gradually increases reaching a peak value at 103 MHz at approximately  $30^\circ$  and then falling off again due to blurring across the finite receiver bandwidth and finite source size. Although the scintillation index varies from day-to-day, depending upon the conditions prevailing in the interplanetary medium (IPM), a large number of observations of a given radio source over a range of elongations from about  $10^\circ$  to  $90^\circ$  can be used to determine the mean behaviour of scintillation index as a function of elongation by fitting the data points by a polynomial.

The scintillation index depends upon the observing frequency ( $f$ ), the solar elongation ( $\epsilon$ ), the brightness distribution of the source  $B(\theta, \phi)$ , and as already mentioned above, the prevailing conditions in the IPM. If one assumes a model for the IPM (Readhead, 1971; Marians, 1975 b) the scintillation index can be calculated in either the weak scattering regime where  $m$  increases with decreasing  $\epsilon$  or the strong scattering regime where  $m$  decreases with decreasing  $\epsilon$ . Close to the turnover, however, the scintillation index is calculated by interpolation since no analytical formulation is valid in this region. The model used in this study assumes a Gaussian spectrum of electron density irregularities given by (Readhead, Kemp and Hewish, 1978, henceforth referred to as RKH) to calculate the variation of scintillation index with solar elongation. There exists a disagreement though as to whether the irregularity spectrum is best approximated by a Gaussian (RKH, 1978) or a powerlaw (Armstrong and Coles, 1978).

In the present study the expected values of scintillation index over a range of elongations, confined to the weak scattering regime ( $\epsilon \geq 30^\circ$ ), were calculated using the RKH model for the IPM and integrating equation (2.7) from 0 to 5 AU. The assumptions made in the model were the following :

- 1) The parameters of the medium vary only with  $r$ , the radial distance and
- 2) The autocorrelation function of the electron density variations is a Gaussian with a characteristic width to  $1/e$  and an rms magnitude  $\Delta N_e(r)$ .

Equation (2.7) applies only to the weak scattering case and Table 4.1 shows the values of scintillation index ( $m$ ) obtained for different source sizes over a range of elongations from  $30^\circ$  to  $100^\circ$ . These values were obtained by integrating (2.7) from 0 to 5 AU and have been rounded off to two decimal places in the table. Figure 4.1 shows the calculated curves of  $m$  Vs  $\epsilon$  based on a composite IPM model by (Kemp 1979).

Under the assumption that the true source profile is a Gaussian with circular symmetry, the brightness distribution  $B(\theta, \phi)$ , loses its  $\phi$  dependence and can simply be written as  $B(\Theta)$  where  $\Theta$  is the equivalent Gaussian diameter of the source. A single value of the scintillating flux  $\Delta S$  cannot be used to determine  $\Theta$ . Current models of the IPM cannot pinpoint the turnover in the  $m$  Vs  $\epsilon$  curves and at the same time provide a good fit to data at large elongations (Purvis 1981), the best estimate to the source size is obtained by the slope of the  $m$  Vs  $\epsilon$  curve (Readhead 1971), which is a unique indicator of  $\Theta$ . In practice, the scintillation index is measured for a given source over a wide range of elongations and the ratio of the scintillation index at two widely separated elongations is found. The ratio,  $\mathcal{R}$ , for known elongations is a function of  $\Theta$  only and there now exists a one-to-one correspondence between  $\Theta$  and  $\mathcal{R}$  and once the ratio  $\mathcal{R}$  is determined by observations,  $\Theta$  can be determined easily.

**Table 4.1:** CALCULATED VALUES OF SCINTILLATION INDEX (m)  
 AT 103 MHz FOR DIFFERENT SOURCE SIZES OVER A  
 RANGE OF ELONGATIONS ( $\epsilon$ )

Source Size	Scintillation Index (m) at Different Solar Elongations ( $\epsilon$ ).							
( $\Theta''$ )	30°	40°	50°	60°	70°	80°	90°	100°
0.1	0.66	0.48	0.37	0.31	0.26	0.24	0.22	0.17
0.2	0.50	0.39	0.32	0.28	0.24	0.22	0.21	0.14
0.3	0.40	0.32	0.28	0.24	0.22	0.21	0.20	0.13
0.4	0.33	0.28	0.25	0.22	0.21	0.20	0.19	0.11
0.5	0.29	0.25	0.22	0.21	0.19	0.19	0.18	0.10
0.6	0.25	0.22	0.20	0.19	0.18	0.17	0.17	0.09
0.7	0.22	0.20	0.19	0.18	0.17	0.17	0.17	0.08
0.8	0.20	0.18	0.17	0.17	0.16	0.16	0.16	0.07
0.9	0.13	0.17	0.16	0.15	0.15	0.15	0.15	0.06
1.0	0.17	0.15	0.15	0.15	0.14	0.14	0.14	0.05

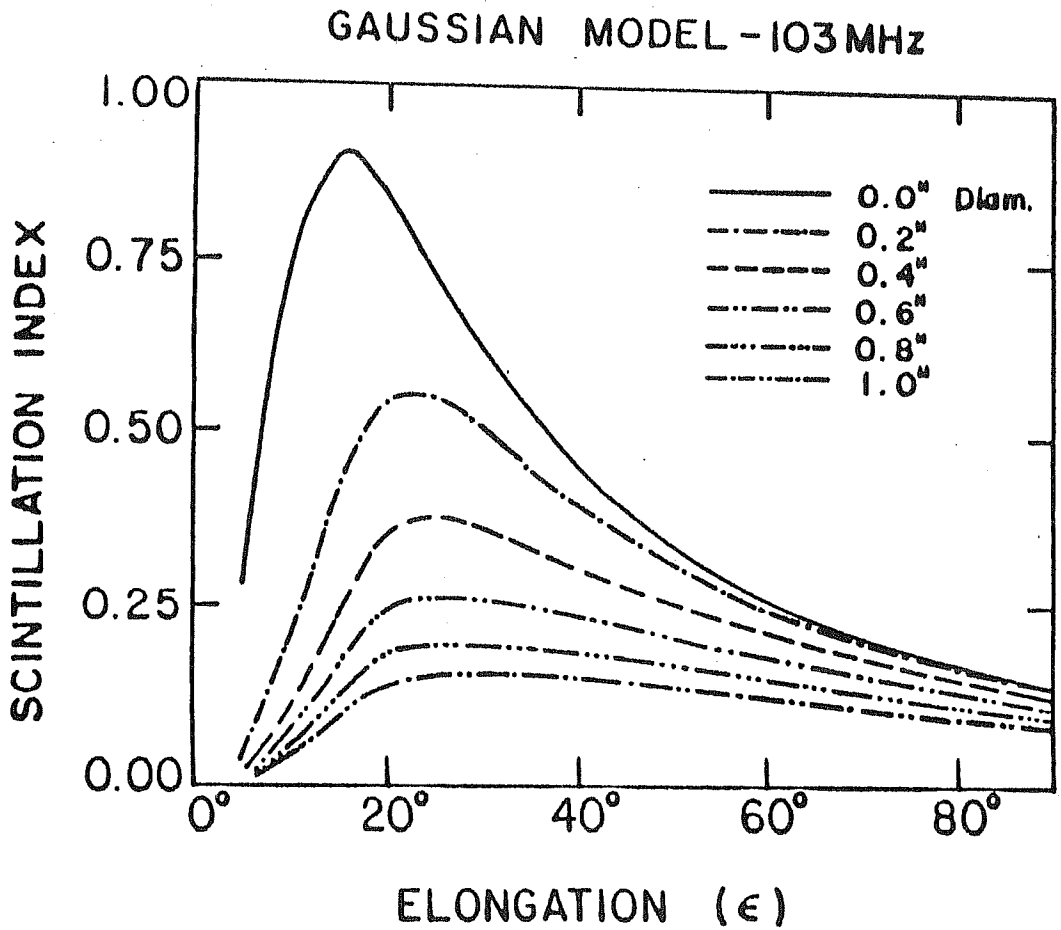


**Figure 4.1**

Shows the calculated curves of scintillation index ( $m$ ) Vs solar elongation ( $\epsilon$ ) using a composite model of the interplanetary medium (M.C.Kemp). Each curve is unique for a given source size.

Essentially,

$$\mathcal{R} = \frac{\Delta S_1}{\Delta S_2} = \frac{m(\Theta \varepsilon_1)}{m(\Theta \varepsilon_2)} = F(\Theta).$$

Figures 4.2a and 4.2b show plots of  $\Theta$  Vs the ratio  $\mathcal{R}$ . The curve was obtained using the calculated values of scintillation index at 103 MHz, some of which are shown in Table 4.1. Thus, all that is now required is to observe a given source over a wide range of elongations and determine the ratio  $\mathcal{R}$  after fitting the observed data points with a 3rd order polynomial. Knowing the ratio ( $\mathcal{R}$ ), the value of  $\Theta$  can easily be found. Since many of the sources were not observed at Thaltej much beyond  $60^\circ$ , it was necessary to use both the curves 4.2a and 4.2b for determining  $\Theta$  depending on whether the observations extended beyond  $60^\circ$  or  $70^\circ$  elongation.

### 4.3 Measurement of Scintillation Index.

The scintillation indices were derived from the measured deflection on the sin, cos and scintillometer channels of the chart recorder after appropriate calibration. A typical set of recordings for the source 3C48 is shown in Plate 2. If  $v_1$  denotes the output voltage of the receiver and  $v_2$  the output voltage of the scintillometer then we know that  $v_1$  is given by

$$v_1 = C T_1 \overline{S},$$

where  $C$  is some constant of proportionality,  $T_1$  is the antenna temperature and  $\overline{S}$  is the mean source flux. Similarly, since the scintillometer is a



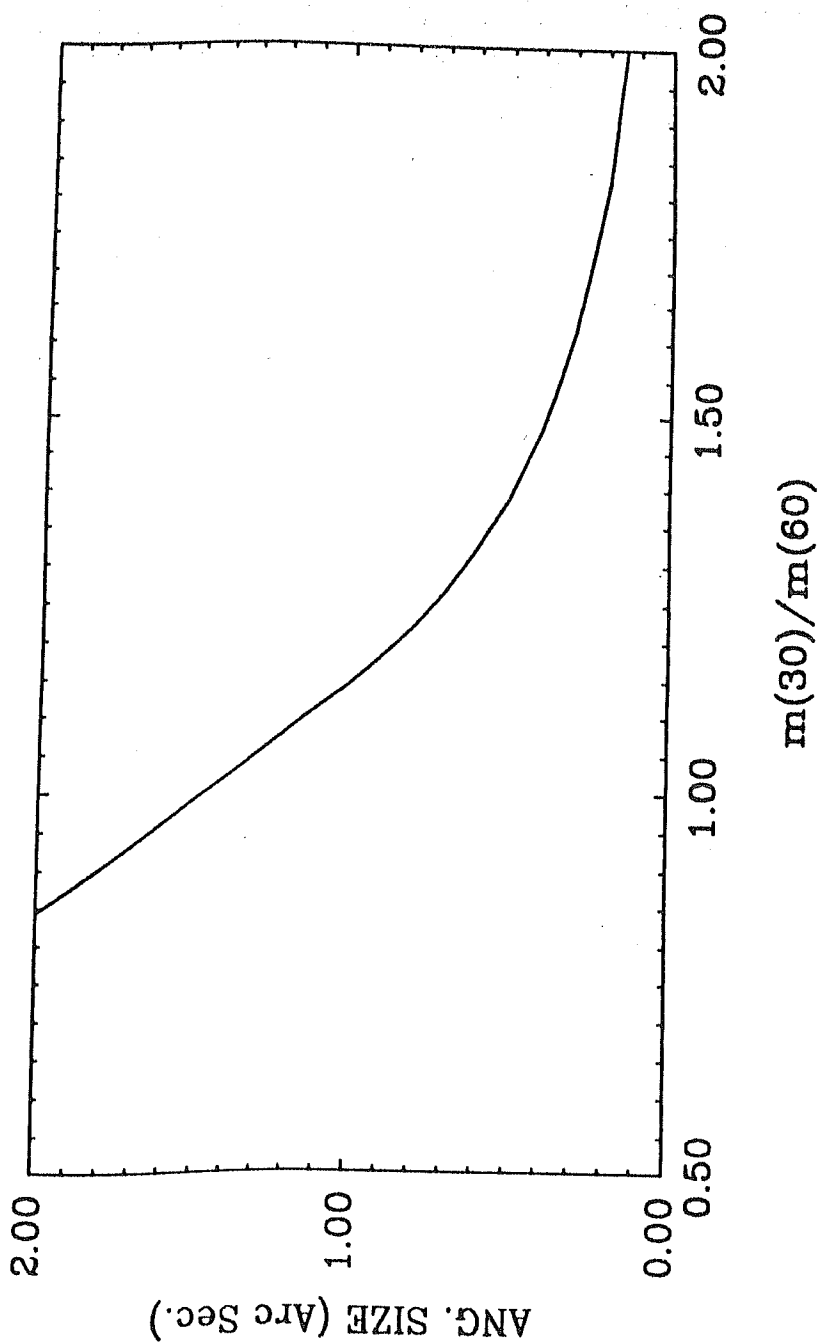


Figure 4.2 a Shows the variation of angular size ( $\Theta$ ) with changing scintillation index ratio ( $\mathcal{R}$ ). The ratio is taken at  $\epsilon_1 = 30^\circ$  and  $\epsilon_2 = 60^\circ$ .

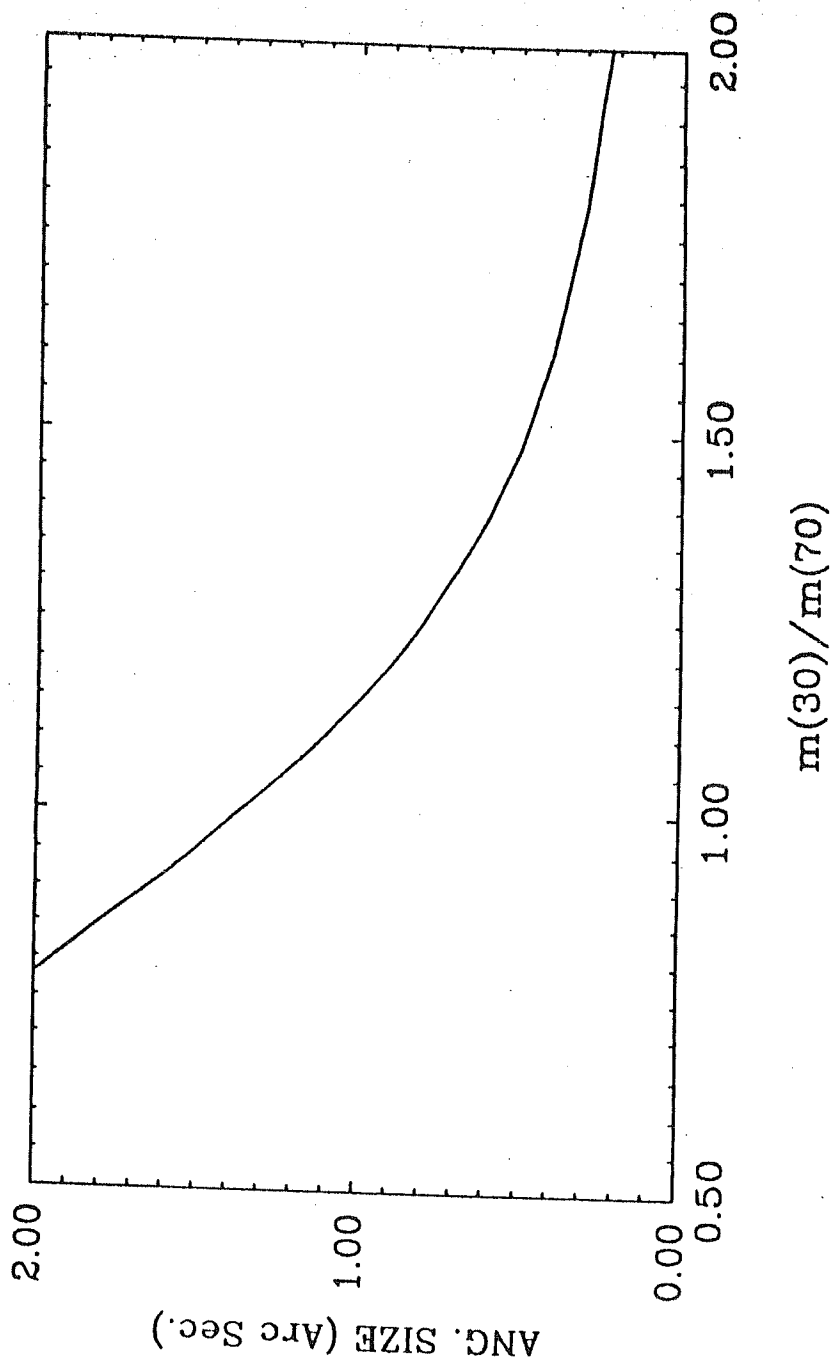


Figure 4.2 b

Shows the variation of angular size ( $\Theta$ ) with changing scintillation index ratio ( $\mathcal{R}$ ). The ratio is taken at  $\epsilon_1 = 30^\circ$  and  $\epsilon_2 = 70^\circ$ .

square-law device and is sensitive only to the scintillating flux  $\Delta S$ ,

$$v_2 = K(C T_1)^2 (\overline{\Delta S})^2,$$

where  $K$  is another constant. Using these two relations we get,

$$\Delta S^2 = \frac{v_2 \overline{S}^2}{K v_1^2}$$

Here the only quantity that has to be determined is the constant  $K$ . The mean source flux  $\overline{S}$  was taken from the 81.5 MHz catalogue (Readhead and Hewish, 1974) and scaled to 103 MHz using the relation  $S_f = f^{0.75}$ , (Readhead and Hewish, 1974) where  $S_f$  is the flux at a frequency  $f$ . The constant  $K$  was determined by calibrating the scintillometer in the following manner. A noise generator was used to produce an input signal at 8 Hz. This input was fed to the sin and cos channels simultaneously using an Iso-T. The input was increased in steps of 0.1 V and the corresponding outputs were noted. The scintillometer has an adjustable gain setting where it can be set to a gain factor of  $\times 3$  for weakly scintillating sources. The process was thus carried out for both scintillometer settings of  $\times 1$  and  $\times 3$  and a log-log plot of input Vs output was made for each set of data. The data points were then fitted by a straight line. The slope of the line obtained in all cases was 2 within experimental error, thus verifying the square-law behaviour of the scintillometer. The anti-log of the y-intercept was associated with the constant  $K$ . The scintillometer calibration was carried out at regular intervals and Figure 4.3a-4.3c shows two sets of scintillometer calibration data for each of the years 1985 to 1987. These data

sets were chosen randomly from the available data sets, obtained by the calibration procedure which was repeated at intervals of 3 months.

Using the value of  $K$  obtained from the scintillometer calibration procedure and the measured deflections of the sin, cos and scintillometer channels the scintillation index can be determined after correcting the deflections for the effects of the AGC using the curves in Fig. 3.6a - 3.6c. Figure 4.4a - 4.4g shows the scintillation indices obtained for various sources plotted as a function of solar elongation. The data available from all the years between mid-1984 and end of 1987 were used and the data points were then fitted by a 3rd order polynomial. Each open circle in the figure represents the mean value of all data falling within a  $1^\circ$  bin of elongation. The solid line, shown separately below each set of observations, represents a third order polynomial fit with the filled circles representing the mean values in each  $10^\circ$  bin. Shown also is a standard error bar in each  $10^\circ$  bin. Now, using the coefficients of the polynomial fit, the ratio,  $\mathcal{R}$ , of scintillation index at  $30^\circ$  to that at  $70^\circ$  or  $30^\circ$  to that at  $60^\circ$ , as the case may be depending upon the observations, was determined and from these ratios the angular diameter  $\Theta$  of each of the fourteen sources observed was determined. Table 4.2 shows the values of source sizes determined at 103 MHz. The source 3C196 was the weakest scintillator observed and as can be seen from Table 4.2 it was measured with the least accuracy. Due to the extended period of observations of each source, each set of observations was subject to different observing conditions, signal to noise ratios, interference, solar activity, and varying conditions in the interplanetary medium. Hence all the sources could not be measured with

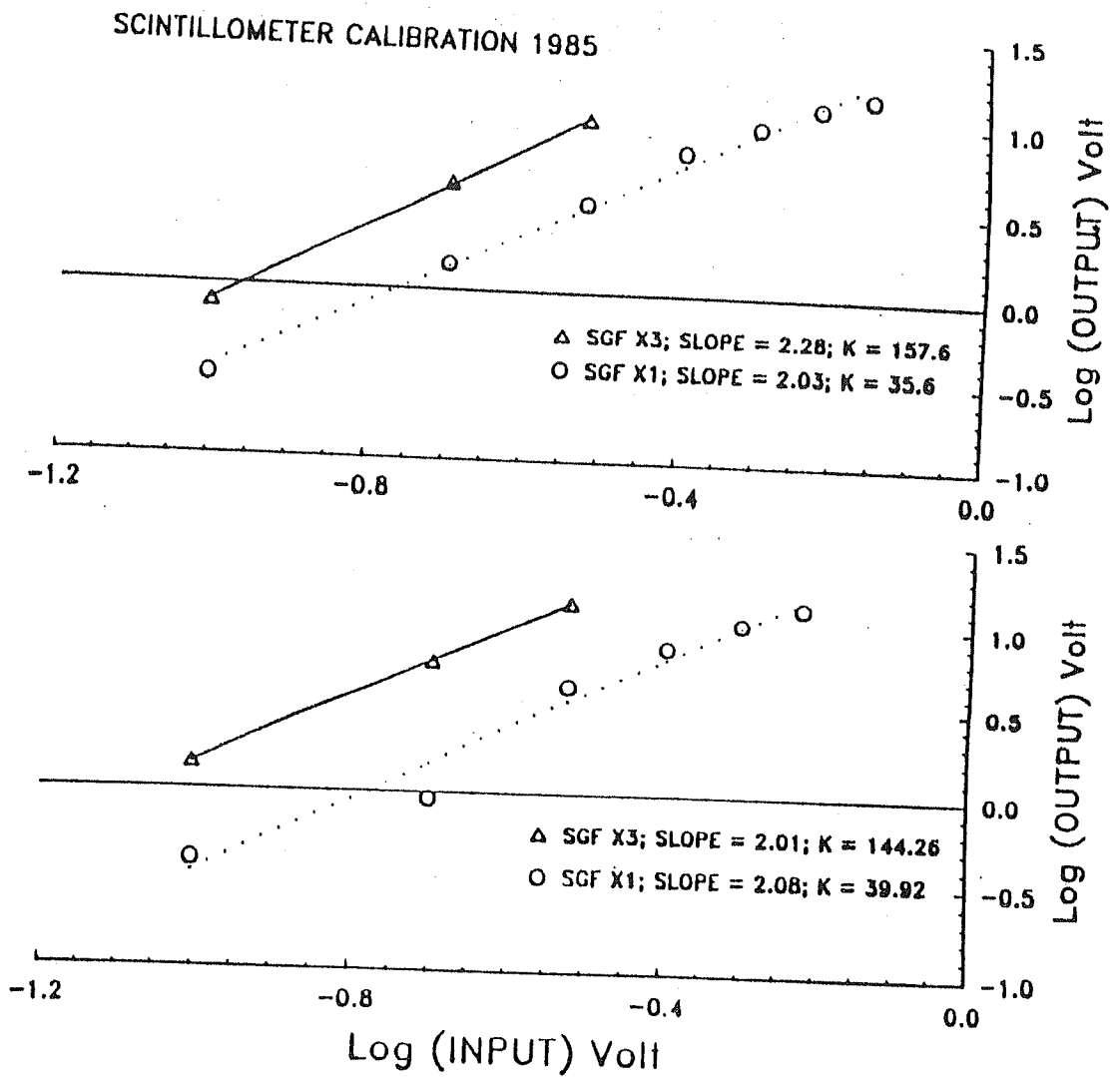
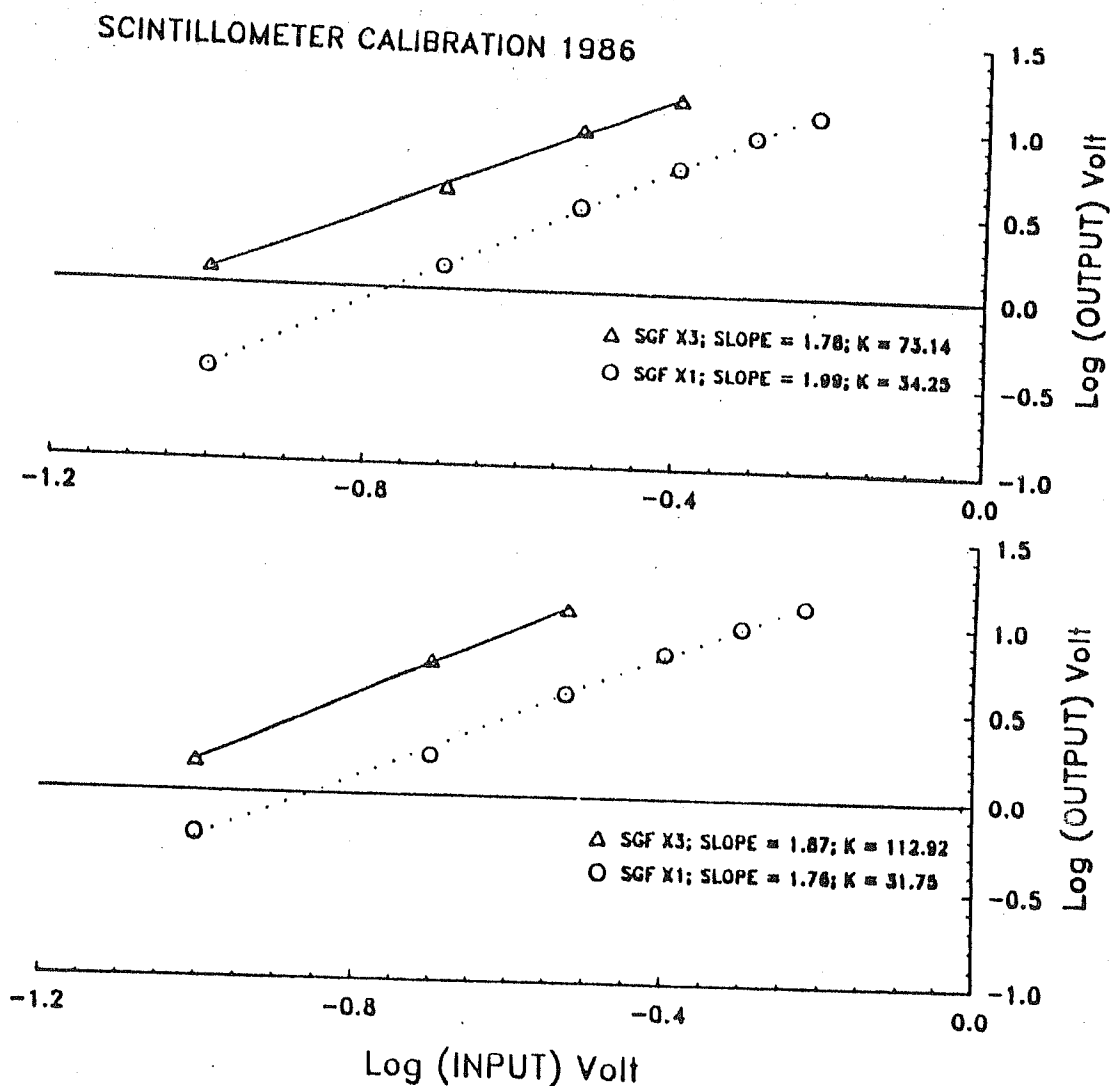


Figure 4.3 a

Shows a log-log plot of input voltage of a noise source at 8 Hz Vs output voltage for the scintillometer. The open triangles and circles represent the two available gain settings of  $\times 3$  and  $\times 1$  respectively with the solid and dotted lines being straight line fits.  $K$  is the antilog of the  $y$ -intercept. The two data sets were chosen at random from the available data sets in 1985.



**Figure 4.3 b**

Shows a log-log plot of input voltage of a noise source at 8 Hz Vs output voltage for the scintillometer. The open triangles and circles represent the two available gain settings of  $\times 3$  and  $\times 1$  respectively with the solid and dotted lines being straight line fits.  $K$  is the antilog of the  $y$ -intercept. The two data sets were chosen at random from the available data sets in 1986.

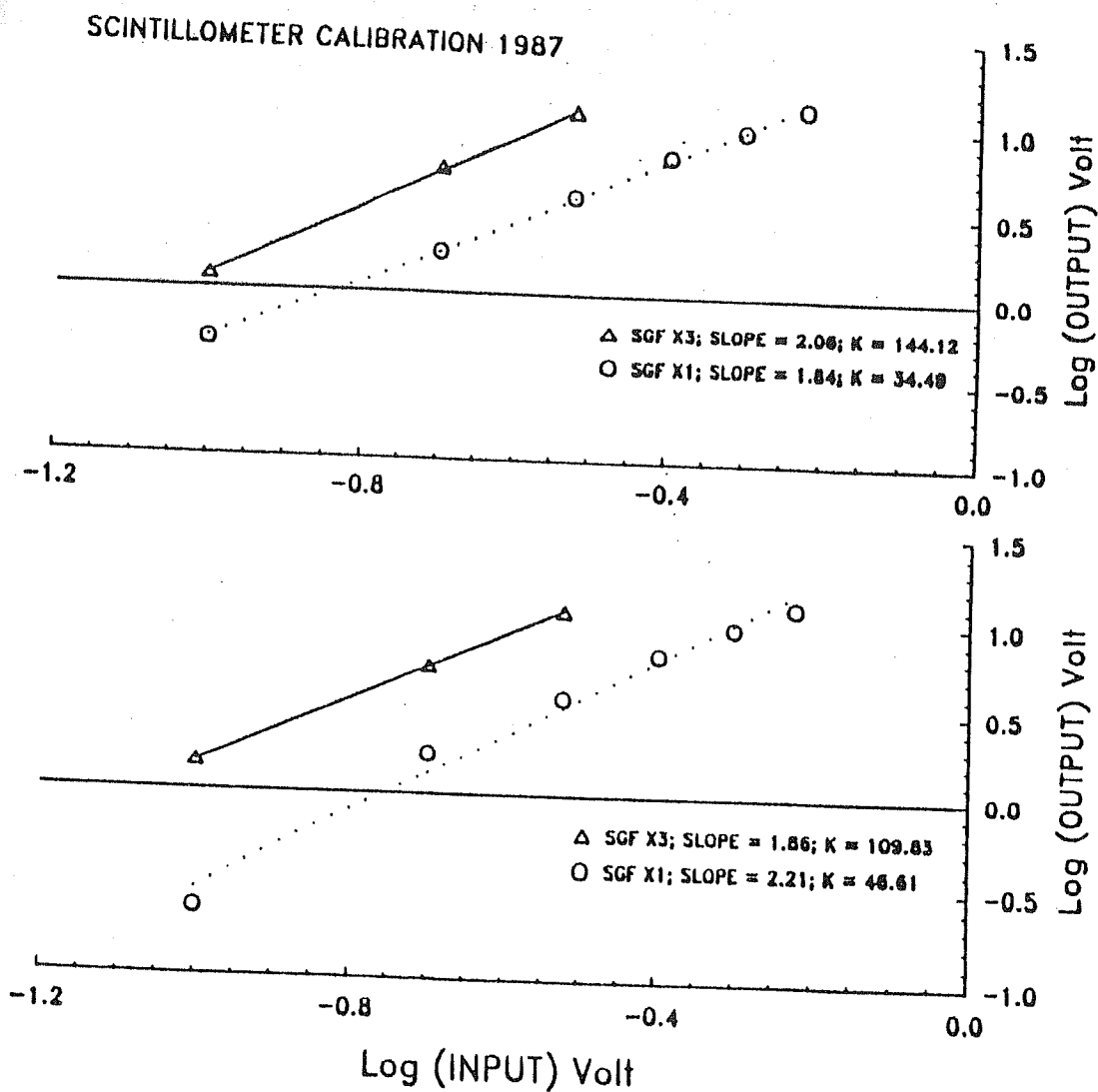


Figure 4.3 c

Shows a log-log plot of input voltage of a noise source at 8 Hz Vs output voltage for the scintillometer. The open triangles and circles represent the two available gain settings of  $\times 3$  and  $\times 1$  respectively with the solid and dotted lines being straight line fits.  $K$  is the antilog of the  $y$ -intercept. The two data sets were chosen at random from the available data sets in 1987.

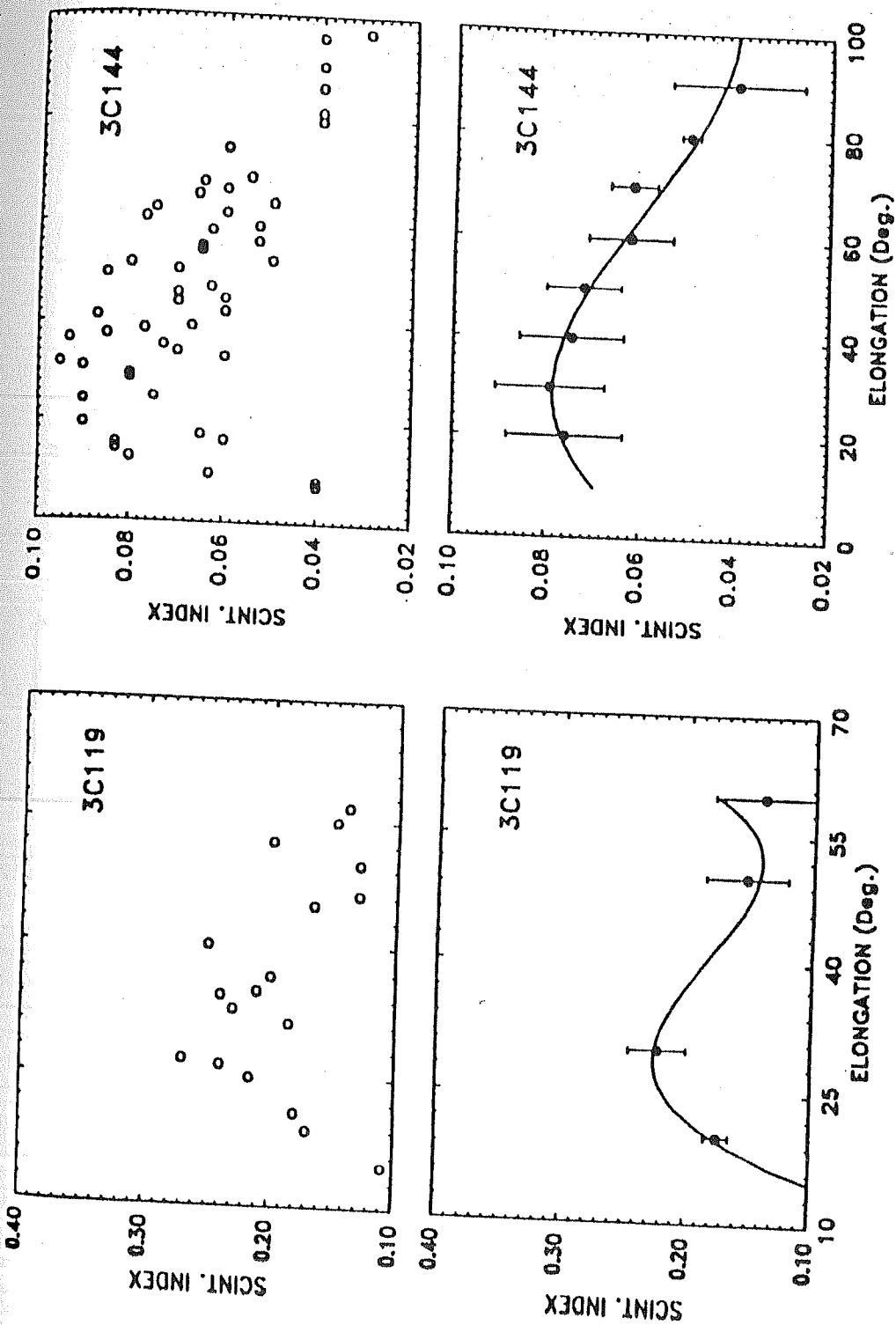


Figure 4.4 a

Shows the observations (upper boxes) of scintillation index (m) as a function of solar elongation ( $\epsilon$ ) for the sources 3C119 and 3C144. Third order polynomial fits (lower boxes) with filled circles representing the mean value in every  $10^\circ$  bin and corresponding standard error bars are also shown. Each open circle represents the mean of all values in a  $1^\circ$  bin.



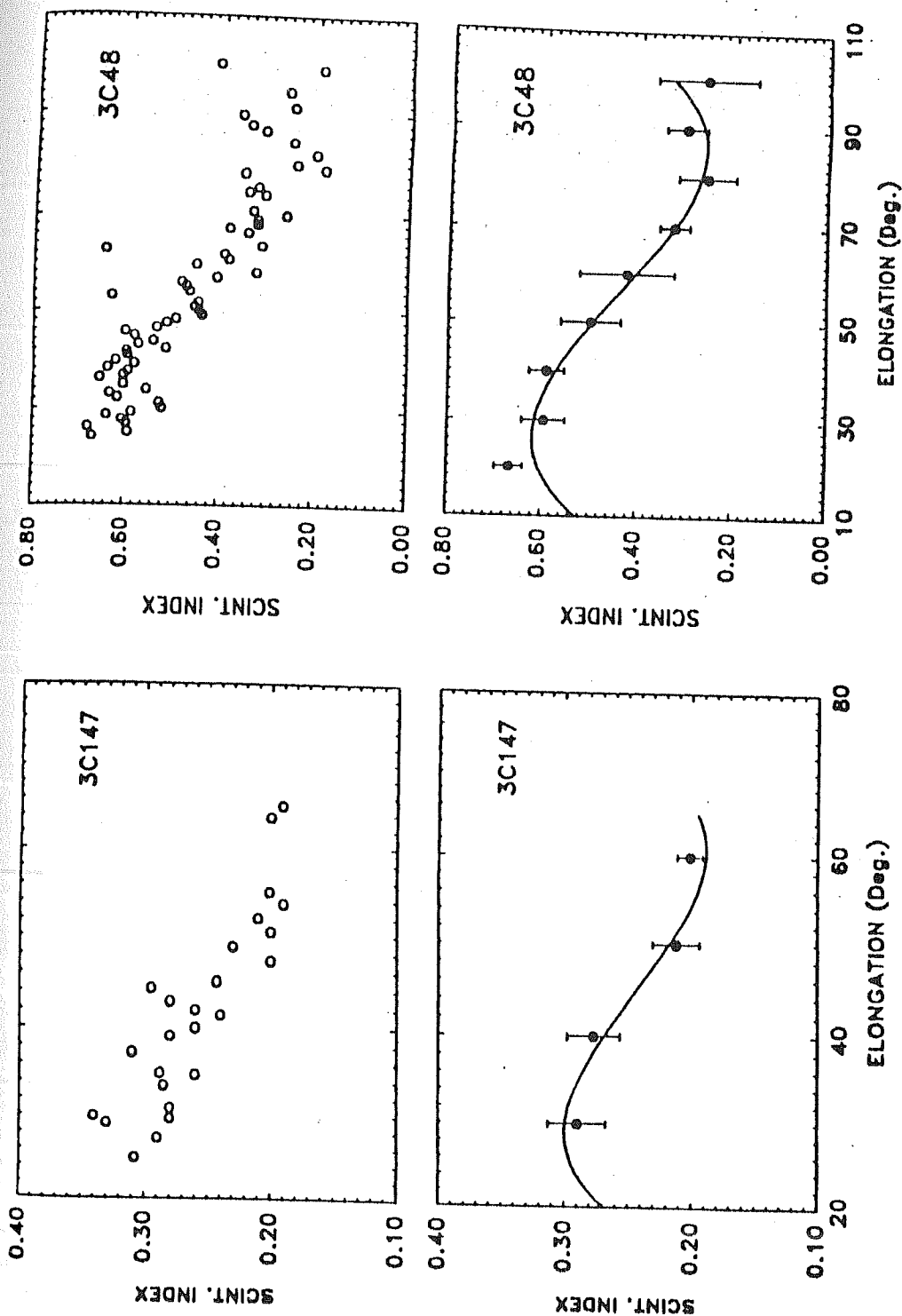


Figure 4.4 b

Shows the observations (upper boxes) of scintillation index ( $m$ ) as a function of solar elongation ( $\epsilon$ ) for the sources 3C147 and 3C48. Third order polynomial fits (lower boxes) with filled circles representing the mean value in every  $10^\circ$  bin and corresponding standard error bars are also shown. Each open circle represents the mean of all values in a  $1^\circ$  bin.

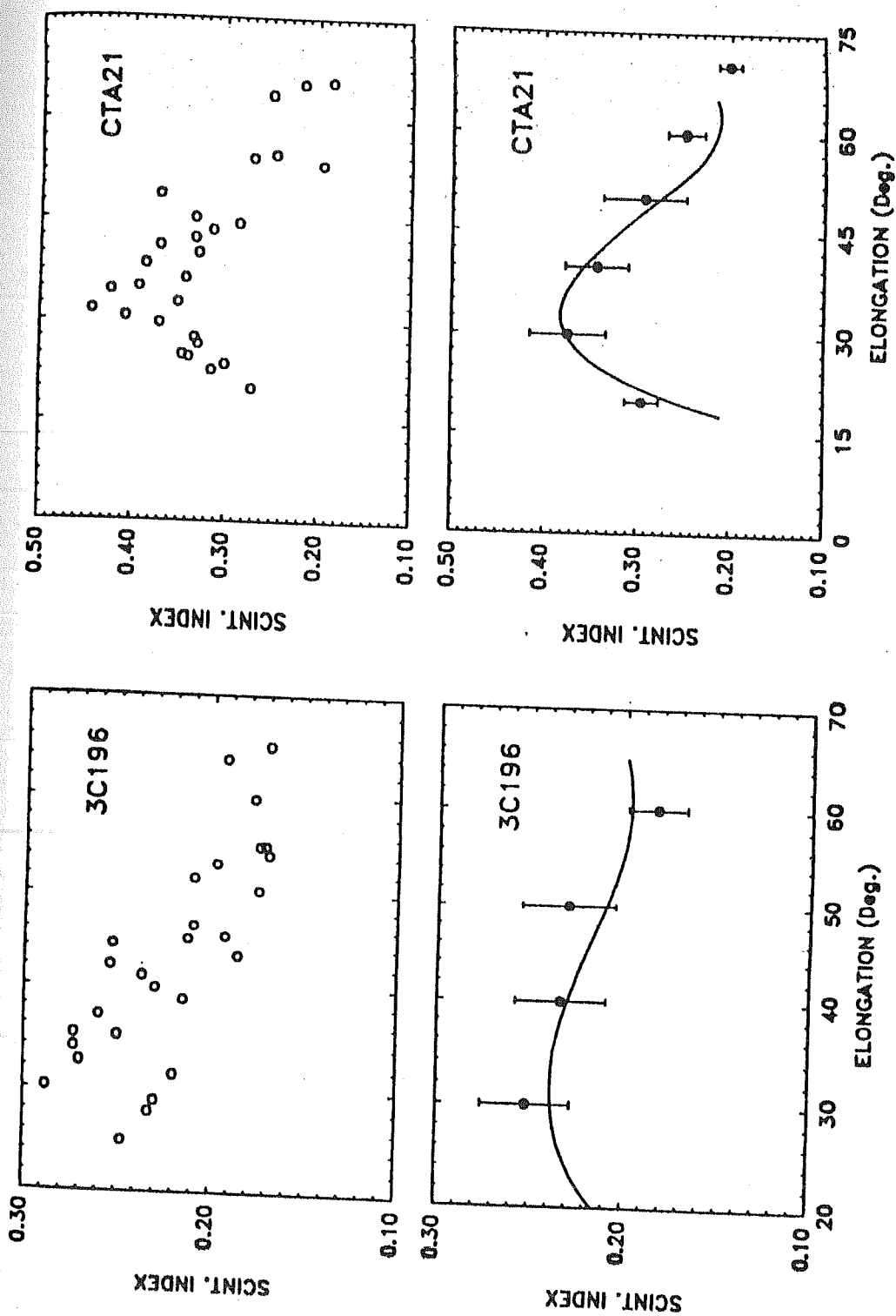


Figure 4.4 c

Shows the observations (upper boxes) of scintillation index ( $m$ ) as a function of solar elongation ( $\epsilon$ ) for the sources 3C196 and CTA21. Third order polynomial fits (lower boxes) with filled circles representing the mean value in every  $10^\circ$  bin and corresponding standard error bars are also shown. Each open circle represents the mean of all values in a  $1^\circ$  bin.

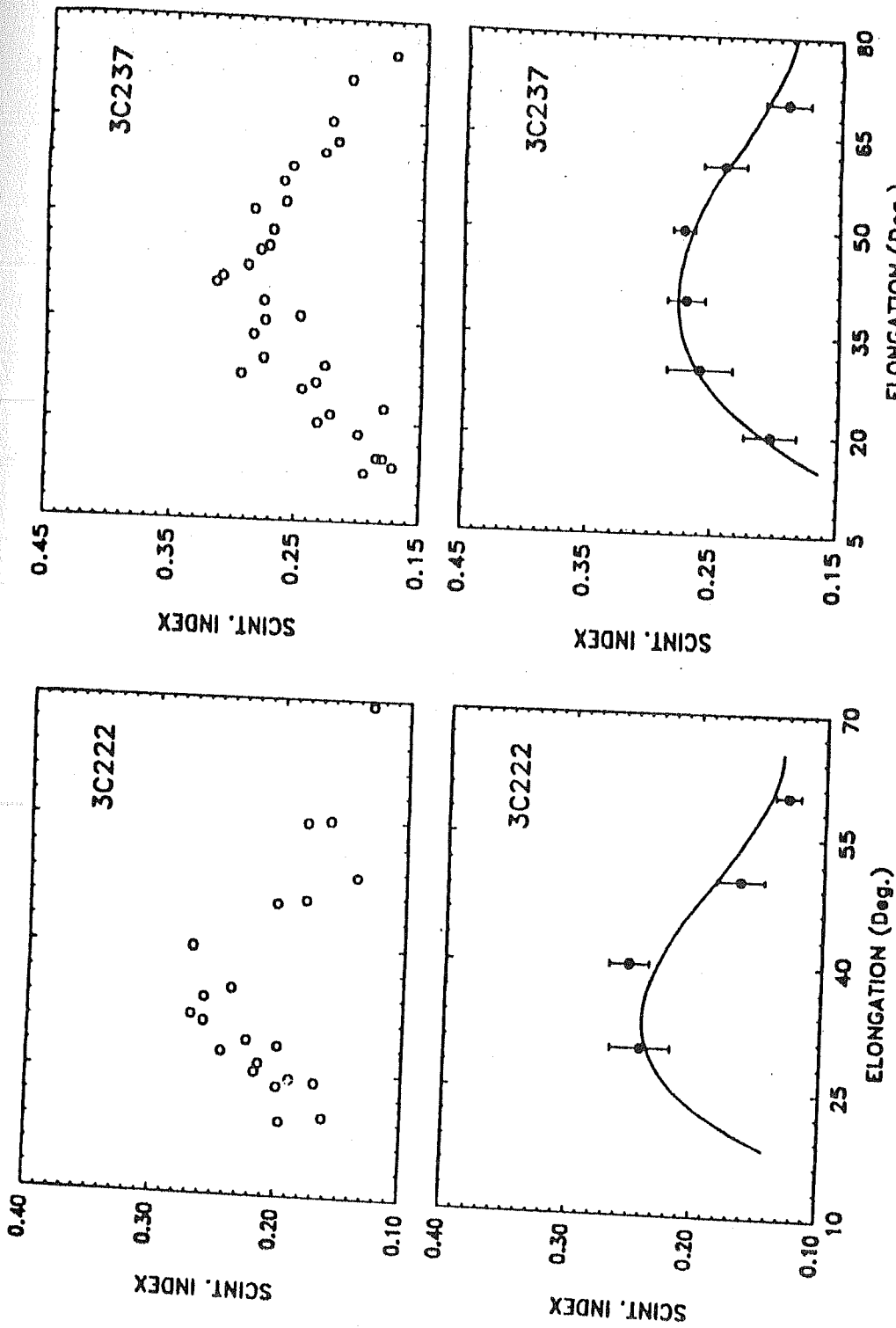


Figure 4.4 d

Shows the observations (upper boxes) of scintillation index (m) as a function of solar elongation (e) for the sources 3C222 and 3C237. Third order polynomial fits (lower boxes) with filled circles representing the mean value in every 10° bin and corresponding standard error bars are also shown. Each open circle represents the mean of all values in a 1° bin.

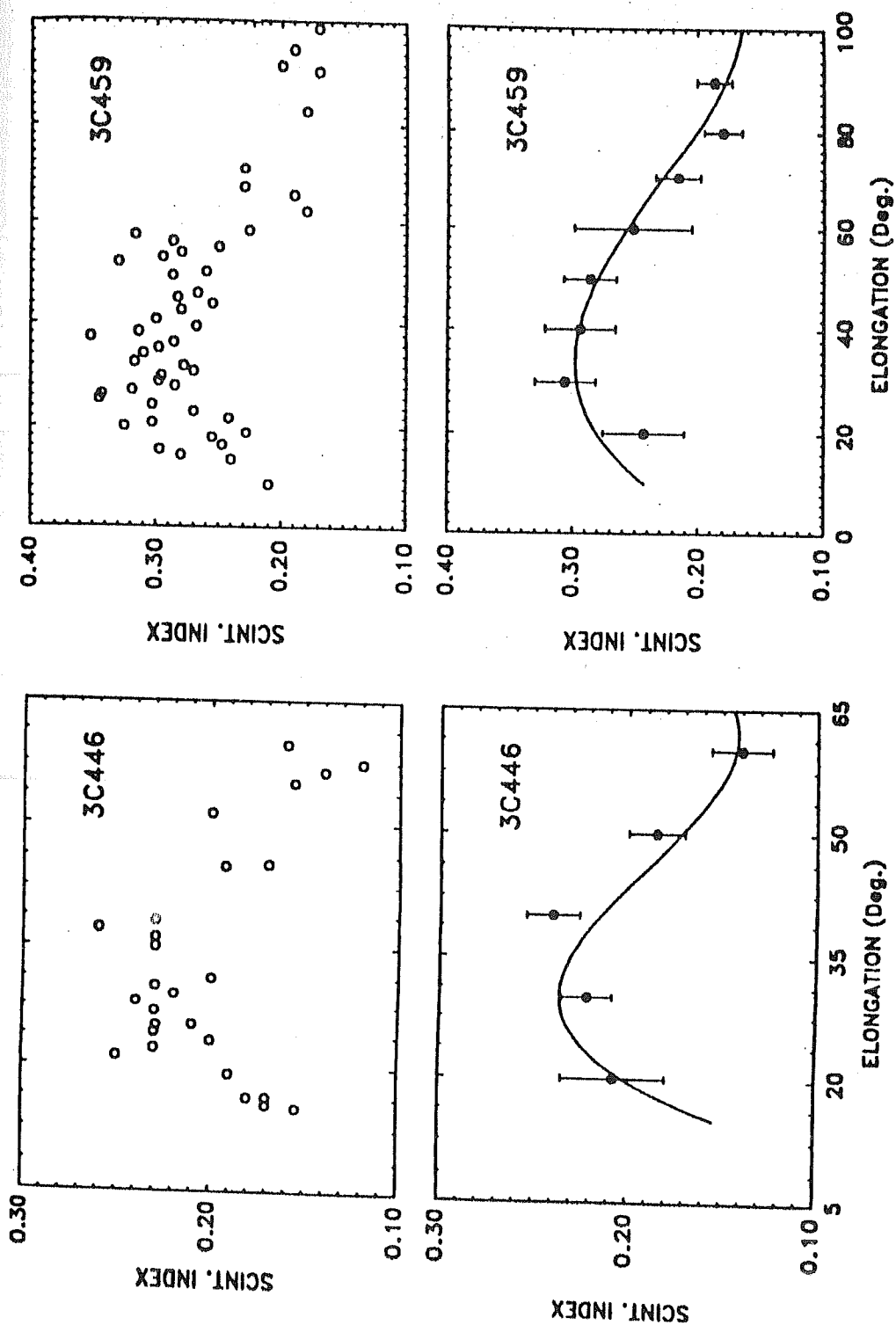


Figure 4.4 e

Shows the observations (upper boxes) of scintillation index (m) as a function of solar elongation ( $\epsilon$ ) for the sources 3C446 and 3C459. Third order polynomial fits (lower boxes) with filled circles representing the mean value in every  $10^\circ$  bin and corresponding standard error bars are also shown. Each open circle represents the mean of all values in a  $1^\circ$  bin.

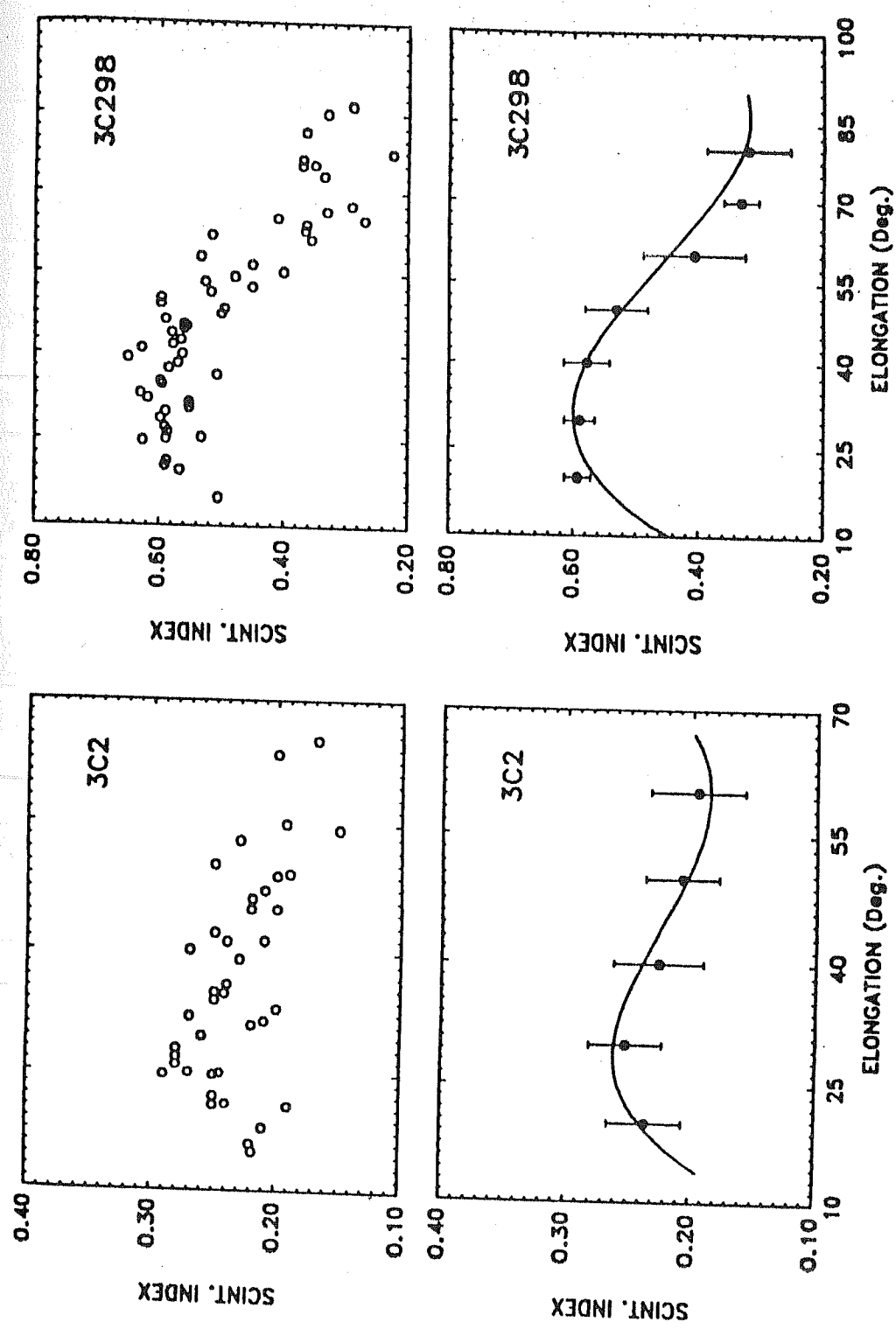


Figure 4.4 f

Shows the observations (upper boxes) of scintillation index ( $m$ ) as a function of solar elongation ( $\epsilon$ ) for the sources 3C2 and 3C298. Third order polynomial fits (lower boxes) with filled circles representing the mean value in every  $10^\circ$  bin and corresponding standard error bars are also shown. Each open circle represents the mean of all values in a  $1^\circ$  bin.

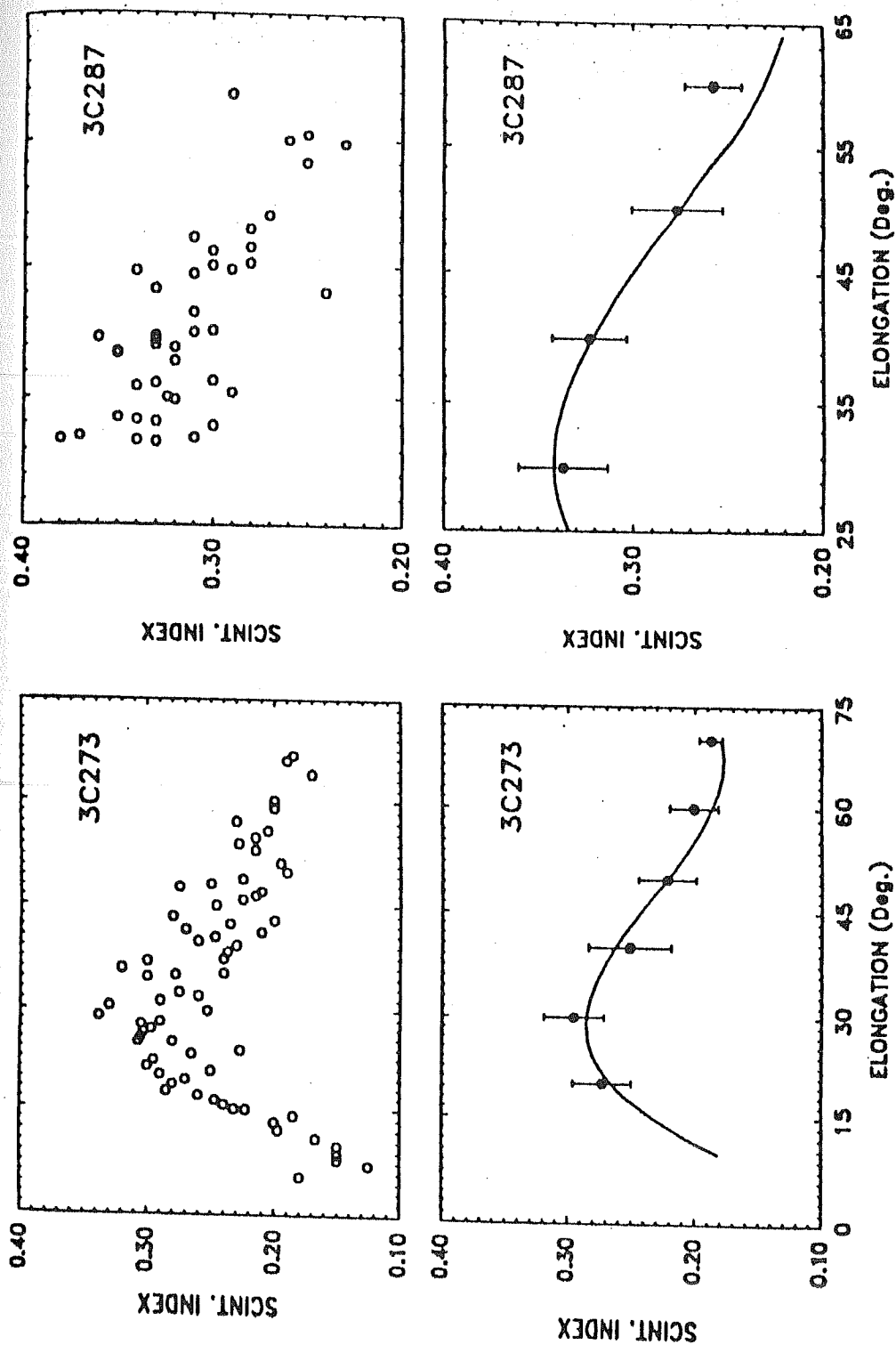


Figure 4.4 g

Shows the observations (upper boxes) of scintillation index (m) as a function of solar elongation ( $\epsilon$ ) for the sources 3C273 and 3C287. Third order polynomial fits (lower boxes) with filled circles representing the mean value in every 10° bin and corresponding standard error bars are also shown. Each open circle represents the mean of all values in a 1° bin.

**Table 4.2:** SOURCE SIZES DETERMINED AT 103 MHz

Source <sup>#</sup>	Coordinates RA and Dec.	Angular Size $\Theta''$ (103 MHz)	Error $\Theta''$	G. Latitude $ b $
3C119	0429+41	0.72	0.14	4
3C144	0531+22	0.34	0.10	6
3C147	0539+50	0.30	0.06	10
3C48	0135+33	0.35	0.04	29
3C196	0810+47	0.84	0.27	33
CTA21	0316+16	0.21	0.04	34
3C222	0934+06	0.33	0.08	38
3C237	1005+08	0.58	0.13	47
3C446	2223-05	0.25	0.05	49
3C459	2314+03	0.41	0.09	51
3C2	0004+01	0.49	0.10	61
3C298	1416+07	0.59	0.07	61
3C273	1226+02	0.55	0.06	64
3C287	1328+25	0.45	0.09	81

# The sources have been arranged in increasing order of galactic latitude  $|b|$ .

**Table 4.3: COMPARISON OF DIAMETER ESTIMATES AT DIFFERENT FREQUENCIES**

Source <sup>#</sup>	IPS - Frequency				V L B I
	103 MHz.	74 MHz	81.5 MHz	151.5 MHz	74 MHz
3C119	0.72	—	0.35	0.20	—
3C144	0.34	0.21	—	—	0.18
3C147	0.30	0.42	0.60	0.30	—
3C48	0.35	0.41	0.45	0.25	0.32
3C196	0.84	—	1.20	1.00	—
CTA21	0.21	—	0.20	0.25	—
3C222	0.33	—	0.20	0.30	—
3C237	0.58	0.39	0.40	0.40	0.28
3C446	0.25	—	0.35	0.10	—
3C459	0.41	0.48	0.45	0.40	—
3C2	0.49	—	0.70	0.40	—
3C298	0.59	0.42	0.40	0.40	0.34
3C273	0.55	0.44	1.0	0.50	0.37
3C287	0.45	—	0.35	0.40	—

# The sources have been arranged in increasing order of galactic latitude  $|b|$ .



the same accuracies. Table 4.3 shows the values of source sizes at other frequencies using IPS. The last column shows a few available VLBI measurements at 74 MHz (Resch, 1974).

#### 4.4 Measurement of Interstellar Scattering at 103 MHz

Interstellar scattering, as has already been discussed, causes sources to appear larger (Cohen and Cronyn, 1974) than their true intrinsic size. The angular broadening of radio sources was also studied by (Duffett-Smith and Readhead, 1976) who used IPS diameter measurements at 81.5 MHz and 151.5 MHz on a sample of 32 scintillating radio sources to determine the contribution to source broadening at 81.5 MHz. Using the present measurements at 103 MHz and the available diameter measurements at 151.5 MHz a similar study was carried out to determine interstellar broadening at 103 MHz.

The method used is very simple. Any given source can be thought of as having an intrinsic source size  $\Theta_i$  and an additional component  $\Theta_s$  which arises due to scattering in the interstellar medium. This can be expressed as

$$\theta_A^2(\nu) = \theta_i^2(\nu) + \theta_s^2(\nu) \tag{4.1}$$

$\Theta_s$  is the width to 1/e of the angular spectrum of the scattered radiation. If  $\Theta_A$  is measured at two different frequencies  $\nu_1$  and  $\nu_2$ , then we can use

equation (4.1) and the facts that  $\theta_1$  is independent of frequency and  $\theta_s$  scales as  $\nu^{-2}$  (Duffett-Smith and Readhead, 1976) to write

$$\begin{aligned} \Theta_A^2(\nu_1) - \Theta_A^2(\nu_2) &= \Theta_s^2(\nu_1) - \Theta_s^2(\nu_2) \\ &= \Theta_s^2(\nu_1) \left[ 1 - \frac{\Theta_s^2(\nu_2)}{\Theta_s^2(\nu_1)} \right] \\ &= \Theta_s^2(\nu_1) \left[ 1 - \left( \frac{\nu_1}{\nu_2} \right)^4 \right] \end{aligned}$$

$\Theta_A^2(\nu_1) - \Theta_A^2(\nu_2) \approx \Theta_s^2(\nu_1)$

..... (4.2)

Using equation (4.2) and the measured diameters at 103 MHz ( $\nu_1$ ) and 151.5 MHz ( $\nu_2$ ) the value of  $\Theta_s$  for each of the sources can be determined. Due to large errors, caused by subtracting two quantities which are themselves uncertain, the apparent 103 MHz diameters are smaller than the 151.5 MHz estimates in some cases. To study the behaviour of  $\Theta_s$  as a function of galactic latitude, it is therefore necessary to average  $\Theta_s$  ranges of galactic latitude. In the present study another difficulty was that the sample of sources available was very small, thereby doing away with the need for any statistical analysis. Figure 4.5 shows a plot of  $(\Theta_s)^2$  as a function of the modulus of galactic latitude for each of the sources. The sources have been marked off into bins of  $20^\circ$  and each value is shown by an open circle. The

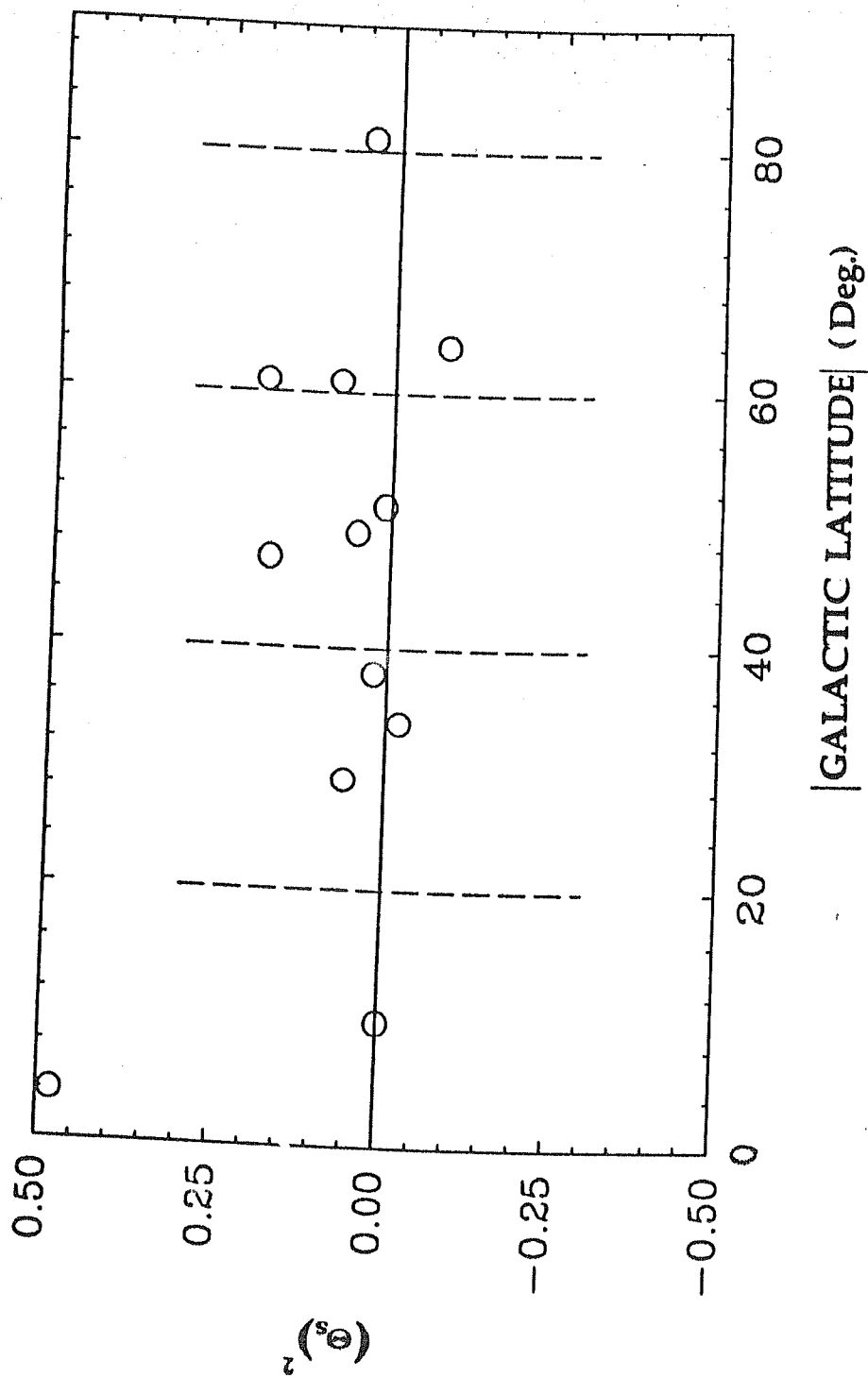


Figure 4.5 Shows a scatter plot of the derived values of  $\Theta_s^2$ , as a function of the galactic latitude  $|b|$ . The vertical broken lines divides the galactic latitude into four ranges of latitude.

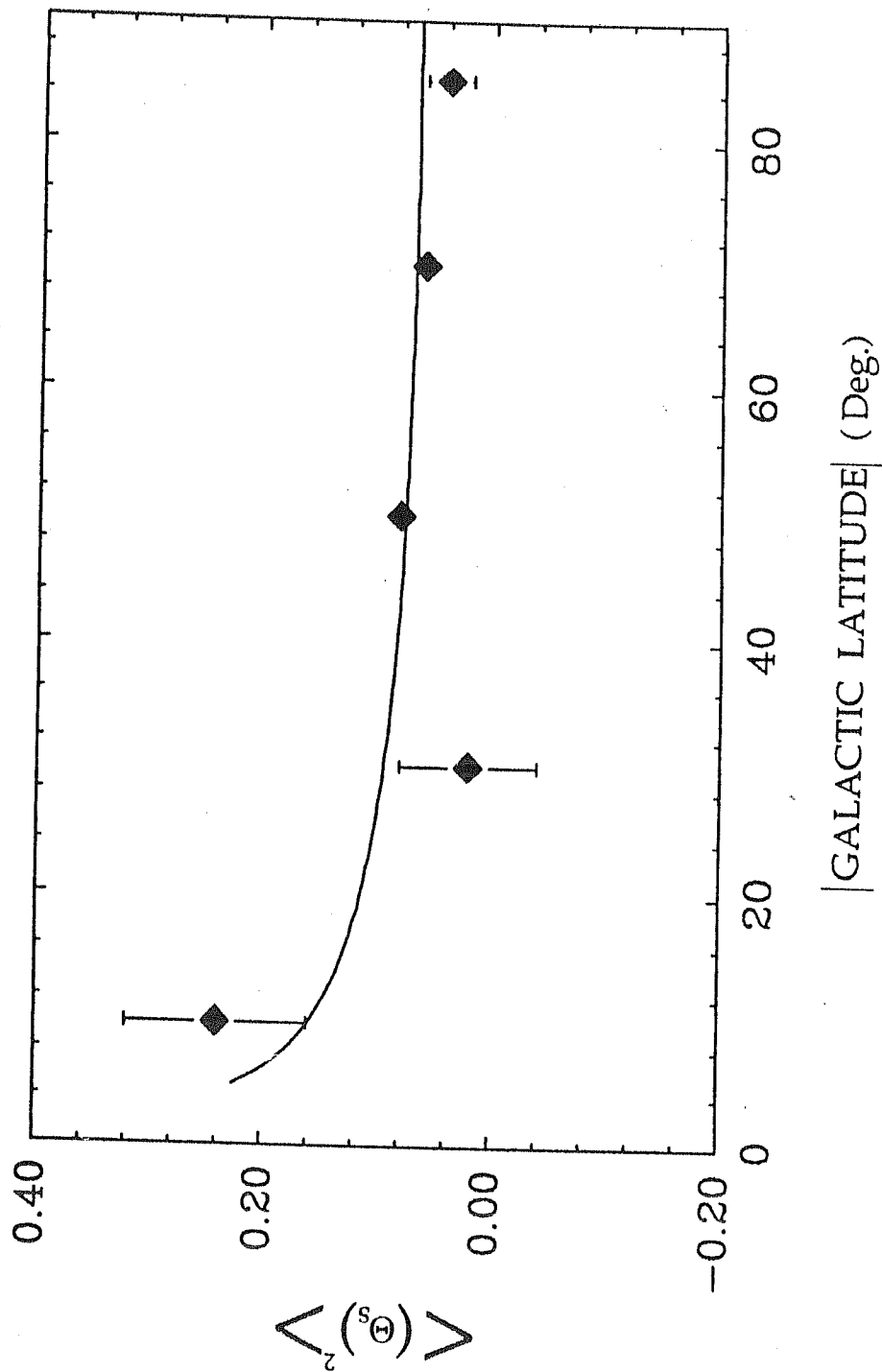


Figure 4.6

Shows the values of  $\langle \Theta_s^2 \rangle$  for the four ranges of galactic latitude. The solid line is a best fit to the data corresponding to  $\Theta_0 = 0.07$  arc seconds at 103 MHz.

source 3C196, the weakest scintillator at 103 MHz, has been dropped from this analysis due to its large error. The source 3C144 does not have a corresponding 151.5 MHz measurement and is also not shown. Figure 4.6 shows the values of  $\langle \Theta_s^2 \rangle$  for the four ranges of galactic latitude Viz.  $|b| \geq 20^\circ$  and  $< 40^\circ$ ;  $|b| \geq 40^\circ$  and  $< 60^\circ$ ;  $|b| \geq 60^\circ$  and  $< 80^\circ$ ;  $|b| \geq 80^\circ$ . The solid curve is a best fit to the data beyond  $20^\circ$  using a functional form (Duffett-Smith and Readhead, 1976),

$$\Theta_s = \frac{\Theta_o}{(\sin |b|)^{\frac{1}{2}}}$$

where  $\Theta_o$  is a constant. The curve shown in Figure 4.6 corresponds to a value of  $\Theta_o = 0.07$  arc seconds. In conclusion we can thus say that the interstellar scattering at 103 MHz amounts to  $0.07 \pm 0.01$ . This value compares well with what is expected at this frequency. In a similar study at 81.5 MHz Duffett-Smith and Readhead (1976) derived a value of  $\Theta_o = 0.15$  arc seconds. Since  $\Theta_s$  scales as  $\nu^{-2}$ , one would expect  $\Theta_o = 0.09$  at 103 MHz.

## 4.5 Conclusion.

The measurements of angular diameters of fourteen compact radio sources by the IPS technique at 103 MHz has yielded results which are comparable with those at other frequencies and with VLBI measurements where available. In spite of having a very small sample of scintillating

radio sources the interstellar scattering at 103 MHz has been determined with reaonable accuracy.

# Chapter - V

## ENHANCED IPS DUE TO COMETARY ION TAILS AT 103 MHZ - COMETS AUSTIN AND HALLEY

### 5.1 Introduction.

Part of the fascination comets hold for astronomers is their transient behaviour. With orbital periods ranging from a few years to thousands of years, comets, when bright, can provide a spectacular sight to the naked eye for a period of several weeks, slowly fading out as they reach the cold outer reaches of the solar system. The main reason that comets are studied, though, is that they can provide answers to some profound astrophysical questions, such as the initial composition and formation mechanism of the solar system.

Astronomers use many techniques to observe comets. These include observations with the unaided eye, binoculars and telescopes; photographs in visual and ultraviolet wavelengths; photometry in visual and infrared wavelengths; spectral scans in many wavelength regions; observations by astronauts orbiting the earth; and observations in extreme ultraviolet wavelengths obtained from rockets and orbiting spacecraft above the earth's atmosphere. In recent times comet Halley was studied by a number of space probes like Vega 1 and Vega 2, Sakigake and Suisei, Giotto and the International Cometary explorer (ICE).

Photographs of bright comets often show two distinct types of tails, the plasma tail and the dust tail. They can exist separately or together in the same comet and both generally point in the anti-solar direction. In a colour photograph, the plasma tail appears blue due to the emission of ionized carbon monoxide ( $\text{CO}^+$ ) bands in the vicinity of  $4,200 \text{ \AA}$ , while the dust tail appears yellow due to the sunlight reflected from it.

If one assumes that density fluctuations similar to those that give rise to IPS in the solar wind plasma also exist in cometary plasma tails then the occultation of a compact radio source by the tail of a comet might lead to an increase in scintillation. In the present study the IPS data obtained during the occultation by the ion tails of comets Austin and Halley of two different compact radio sources was analyzed. The question addressed was whether cometary plasma contained in the tail of a comet can cause radio scintillations and if so under what conditions? The former part of this question has been addressed several times, with positive results being



reported in some cases (Ananthakrishnan *et al.* 1975, Alurkar *et al.* 1986, Slee *et al.* 1986, Janardhan *et al.*, 1991 a) and negative results in others (Ananthakrishnan *et al.* 1987, Hajivassiliou and Duffett-Smith 1987). It has recently been shown conclusively (Slee *et al.* 1990; Janardhan *et al.*, 1991) that under suitable conditions cometary plasma can contain a higher level of turbulence than the normal solar wind and give rise to enhanced scintillations. The importance of occulting geometry and control sources was first pointed out in the science correspondence section of *Nature* (Alurkar *et al.*, 1989a) and (Ananthakrishnan *et al.* , 1989).

The observation of Comet Austin in May 1990 has again confirmed the importance of having the proper occulting geometry, ie. solar elongations ( $\epsilon$ ) in excess of  $60^\circ$ , failing which meaningful enhancements are not observable due to the proximity to the sun causing normal solar-wind IPS to dominate and swamp out any enhancements due to the comet. The observations of Comet Austin have also confirmed the existence of finer scale sizes of turbulence in the tail than are expected in the normal solar wind.

## 5.2 Observations and Analysis - Comet Austin (1989 c1) .

The observations were carried out with the enhanced 20,000  $\text{m}^2$  dipole array in conjunction with the dual channel correlation receiver which has been described fully in the third chapter. As already mentioned

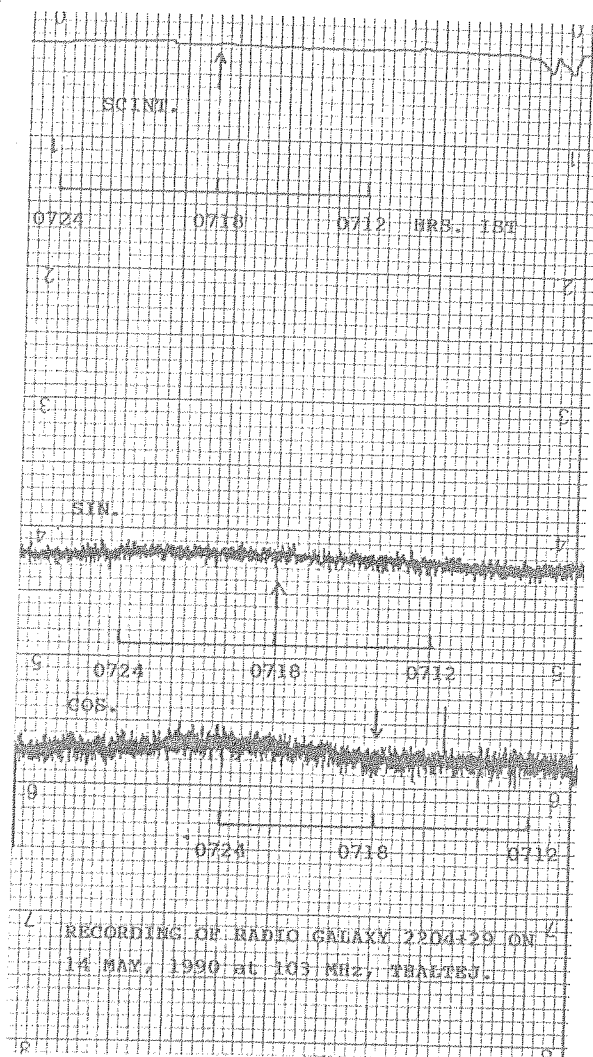
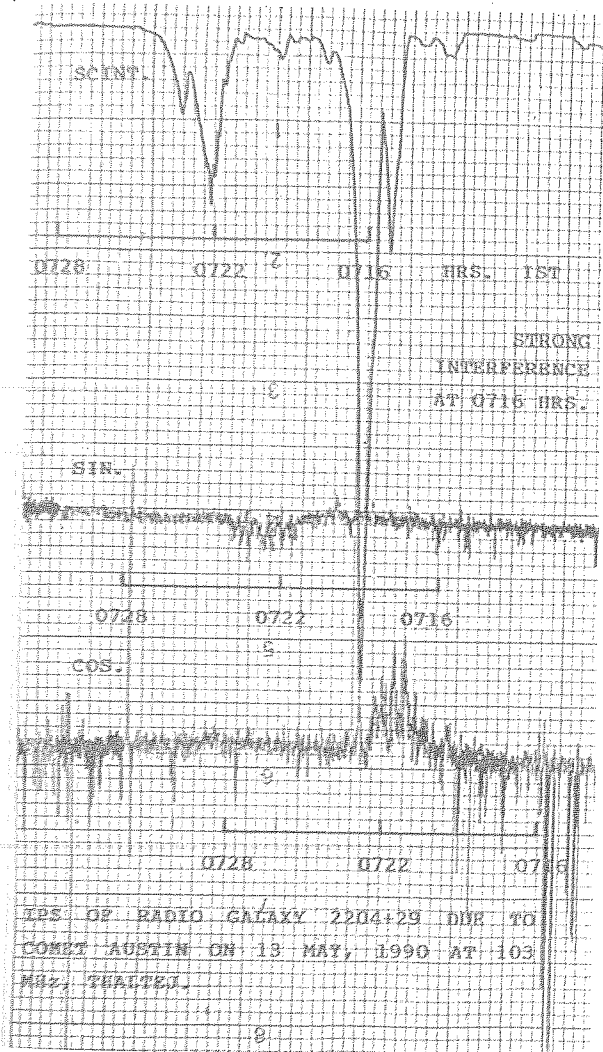
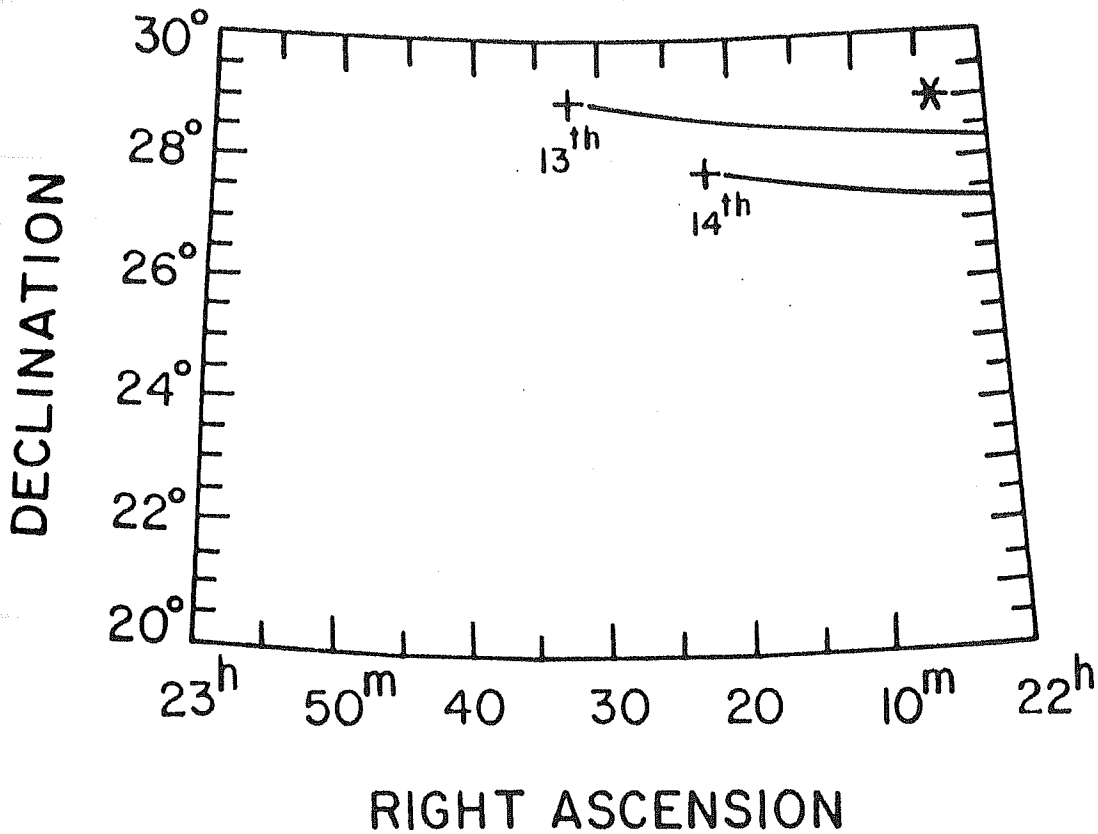


Plate 3 Shows the chart recordings of the occulted source 2204+29 (3C441), during transit on 13 May 1990 when the tail of comet Austin (1989 cl) swept in front of it. Note the clear evidence of scintillation on the sin, cos and scintillometer channels on 13 May while there is no scintillation on 14 May 1990.

before the enhanced array was designed to operate with a total power receiver of much narrower bandwidth but since the receiver was still being built the present observations were carried out with the correlation receiver used with the 10,000 m<sup>2</sup> array. The occulted source declination was such that its position was between the 3rd and 4th Northern beams of the array. The observations were thus made after combining the responses of the 3rd and 4th Northern beams by using a T-connector with good isolation (iso-t) and equal lengths of cable to add the adjacent Butler matrix outputs. The beam width for this observation was thus 3.6° N-S × 1.8° E-W. Plate 3 shows the actual chart recordings of the occulted source on 13 th and 14 th May 1990. The source was monitored continuously for about two weeks prior to and after the occultation and except for the date of the occultation it did not show detectable scintillations. The source 0038+33 (3C19) was the closest scintillating source to 2204+29 and was monitored as a control source. Several other scintillating sources, viz. CTA21, 3C42, 3C48, 3C123, 3C144, 3C161, and 3C196, which were being observed regularly during that period and lying in the declination range -5° to 33° also did not show enhanced scintillation during the period under consideration. It has been shown (Hewish *et al.*, 1985) that large scale interplanetary transients typically cover a solid angle of  $\pi/2$  sr. in heliographic latitude and longitude. They also showed a strong correlation between the total plasma density along the line of sight to a source and enhancement in scintillation. Thus the enhancement observed only in the direction of the occulted source rules out the presence of a large scale transient.

Figure 5.1 shows the path of the cometary nucleus projected onto the

## COMET AUSTIN-MAY 1990



**Figure 5.1** Shows the path of the cometary nucleus projected on the plane of the sky. The crosses mark the nuclear positions at Ahmedabad transit on 13th and 14th May 1990 while the solid lines indicate the approximate directions along which the cometary tail axis would lie. These directions include a tail-lag correction of  $+3^\circ$ .

plane of the sky; the crosses are the nuclear positions at Ahmedabad transit on the two days including the occultation date of 13 May. The solid lines indicate the approximate directions along which the cometary tail axis would lie. These directions include a small correction of  $+3^\circ$  to the azimuth of the anti-solar vector to account for the so called "tail-lag", which is caused by the interaction of the comet's velocity with the radially directed solar wind. The ephemeris for the comet is that published in IAU Circular No. 4985 (March 27, 1990).

Ideally, we require a wide-angle, blue-sensitive photograph of the comet within a few hours of the present radio observation in order to define the position angle of the tail axis, about which the densest part of the plasma should be concentrated. It is clear that an accurate value for the tail-lag is needed to define the position of the radio source with respect to the tail axis. If the tail-lag were as much as  $+5^\circ$ , then the source would be shining through the densest plasma on the axis. If the tail-lag were zero, then the source would be  $5^\circ$  off-axis during the observation, for which one may expect scintillation effects to be significantly reduced.

Figure 5.2 shows the relative positions of the sun, earth and comet Austin during the observations at 103 MHz and Table 5.1 gives a list of the solar elongations for various observations. It can be seen that in all the observations where the occulting geometry has been favorable, ie. solar elongations ( $\epsilon$ ) in excess of  $60^\circ$ , a positive result has been reported. During the first reported observations of enhancements in scintillation (Ananthakrishnan *et al.*, 1975) the solar elongation was only  $20^\circ$ , but at 327

### Relative Positions of Sun, Earth & Comet Austin - May 1990

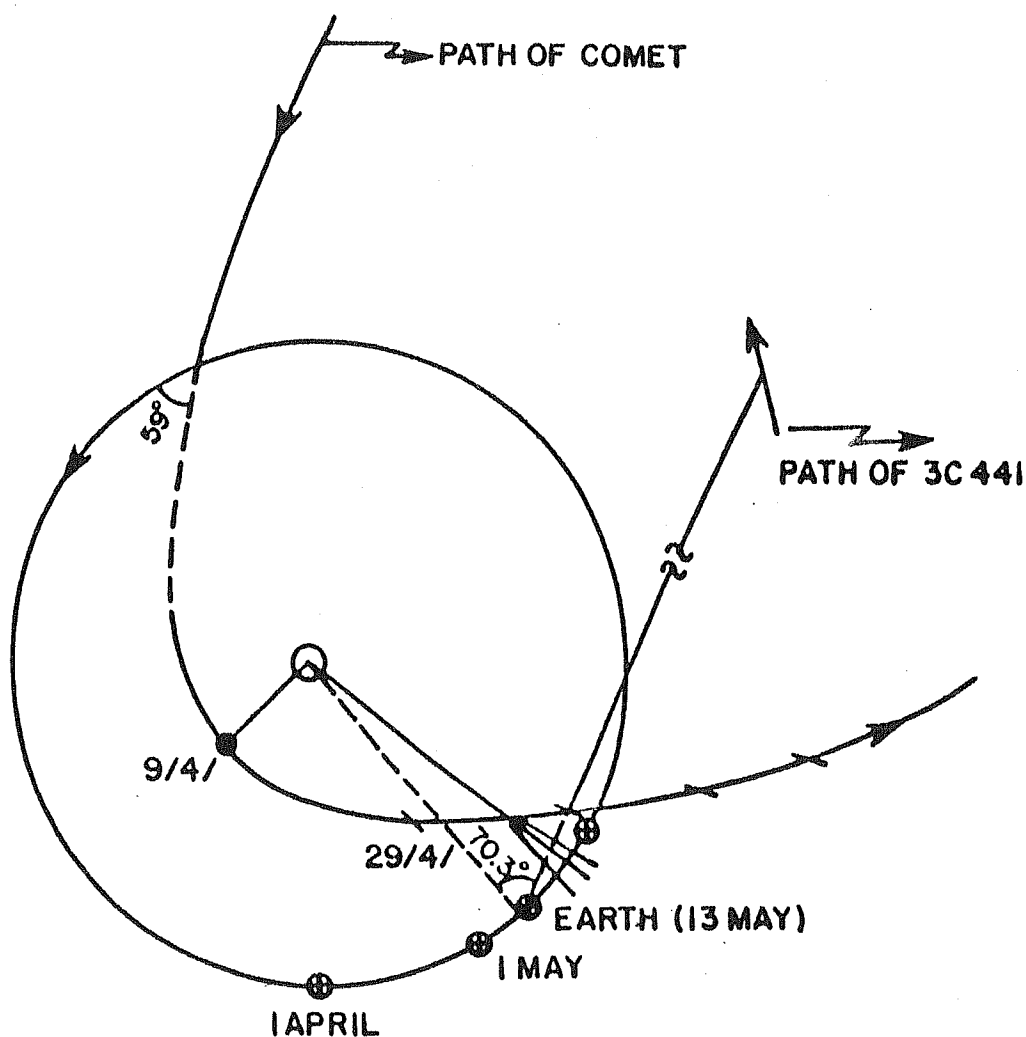


**Figure 5.2** Shows the occulting geometry during the observation of the source 2204+29 (3C441) when the tail of comet Austin (1989 c1) swept in front of it on 13 th May 1990.

**Table 5.1: OCCULTED SOURCE ELONGATIONS FOR DIFFERENT EVENTS**

DATE	FREQ.	COMET	OCCULTED SOURCE	ELONG.	RESULT
	(MHz.)		(RA & DEC 1950)	( $^{\circ}$ )	
05/01/74	327	Kohoutek	2025 - 150	20.0	Positive
18/12/85	103	Halley	2314 +038	86.5	Positive
11/02/86	327	Halley	2052 - 106	11.2	Negative
29/03/86	408	Halley	1827 - 360	86.0	Positive
01/05/87	408	Wilson	0606 - 795	92.8	Positive
02/05/87	408	Wilson	0637 - 752	93.0	Positive
13/05/90	103	Austin	2204 +292	70.3	Positive

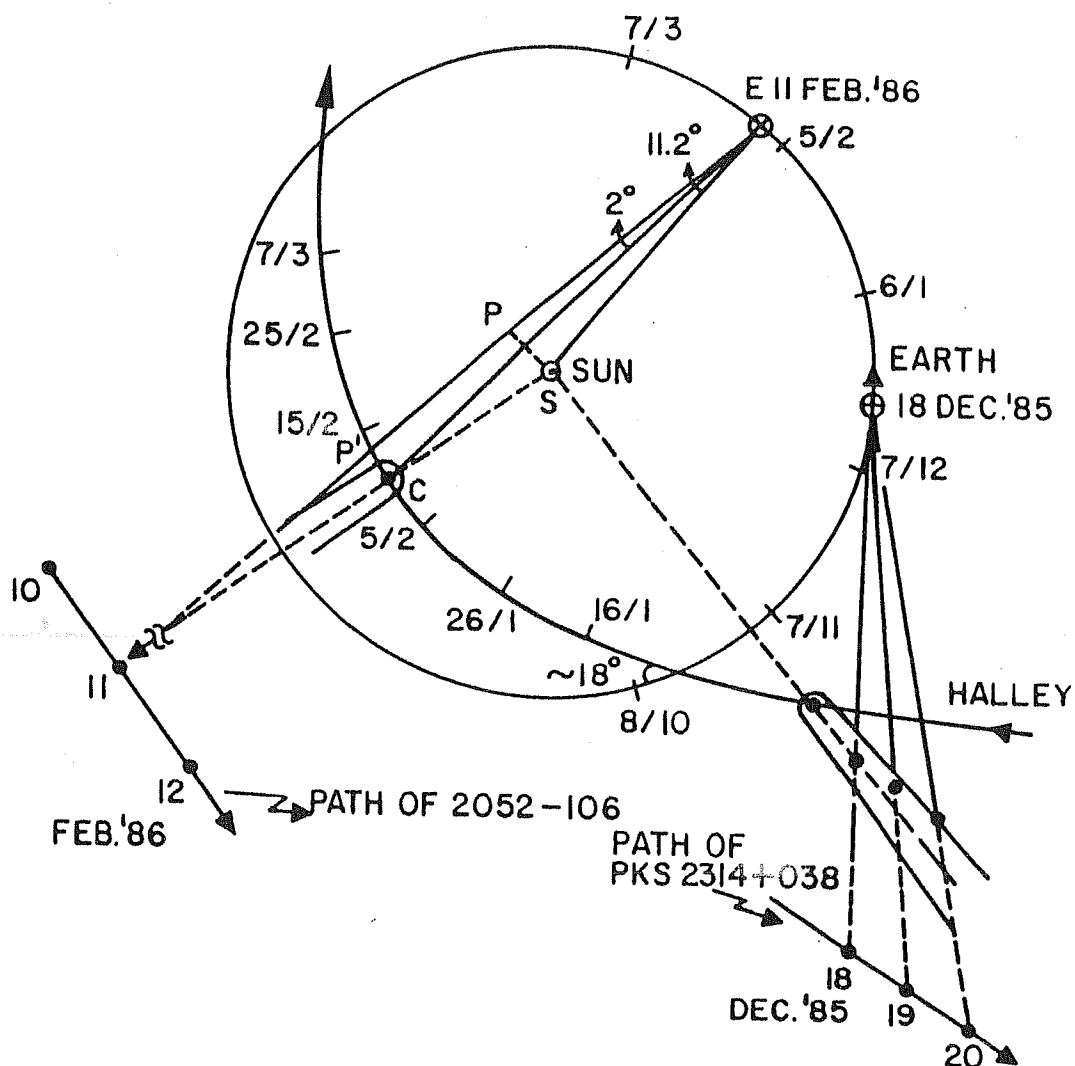
MHz. this elongation is well into the region where weak interplanetary scattering prevails. Figure 5.3 shows the occulting geometry for the observations of comet Halley carried out at 327 MHz, where a negative result was reported (Ananthakrishnan *et al.*, 1987) and the observations of comet Halley at 103 MHz (Alurkar *et al.*, 1986) where a positive result was reported. Note that the observations at small solar elongations cause one to be looking essentially into the sun, thereby swamping the enhancements from the tail of the comet.

Table 5.2 gives the parameters of comet Austin, while Table 5.3 gives the occulted and control source parameters along with the calculated scintillation index for different days and the corresponding scintillation index expected from the RKH model (Readhead *et al.*, 1978). It can be seen that the scintillation index ( $m$ ) of 0.43 on the 13th for the source 2204+29 is greater by a factor of three than that expected from the RKH model, which gives  $m=0.14$ . The scintillation indices were calculated from the chart recordings of the sine, cosine and scintillometer outputs following the calibration procedure described in chapter four, after first correcting the Sine and Cosine channels for the effects of the automatic gain control (AGC) used in the system.

To check the possibility that at least some of the intensity variations may be due to ionospheric scintillation of the radio source, the ionospheric conditions were monitored with the ionosonde at PRL, Ahmedabad. The ionograms taken during the time of transit of the source showed no spread-F or sporadic-E echoes, both of which have been correlated with



# RELATIVE POSITIONS OF SUN, EARTH & COMET HALLEY – DECEMBER 1985 and FEBRUARY 1986



**Figure 5.3** Shows the occulting geometry for two independent observations of comet Halley. Note the very small solar elongation ( $\epsilon$ ) during the Feb'86 observations at 327 MHz, while the Dec'85 observations at 103 MHz had a large  $\epsilon$  and hence a favourable observing geometry.

Table 5.2: COMET AUSTIN PARAMETERS

DATE at 1400 UT	N.COORD. <sup>\$</sup> (RA & DEC)	DISTANCE (AU)		ELONG. ( <sup>o</sup> )	PA of TAIL ( <sup>o</sup> ) <sup>#</sup>
		T.CENTRIC	H.CENTRIC		
12 MAY	22 42.2+30 00.44	0.3597	0.9020	62.4	268.3
13 MAY	22 32.4+28 57.38	0.3443	0.9221	65.4	266.0
14 MAY	22 22.0+27 45.74	0.3296	0.9420	68.6	263.7

<sup>\$</sup> The coordinates are those of the comet nucleus.

<sup>#</sup> The position angles of the tail are given at 0200 UT. The transit time of the source was 0152 UT.

**Table 5.3: OCCULTED AND CONTROL SOURCE PARAMETERS  
DURING COMET AUSTIN OBSERVATIONS**

SOURCE	APPROX. COORD. (1950)	DATE (1990)	ELONG. ( <sup>o</sup> )	OBS. SCINT. INDEX <sup>1</sup>	CALC. SCINT. INDEX <sup>2</sup>	SOURCE DIA. <sup>3</sup> (")
3C441 <sup>*</sup>	2204+29	13/05	70.3	0.43	0.14	1.0
3C19	0038+33	12/05	37.0	0.16	0.18	0.8
		14/05	38.0	0.17	0.18	0.8
3C42	0126+30	12/05	26.0	0.16	0.14	1.2
3C123	0434+30	12/05	24.0	0.18	0.22	0.8

- 1 Calculated scintillation index from observations.
  - 2 Scintillation index calculated from RKH model.
  - 3 Equivalent Gaussian diameter in arc. seconds.(Readhead *et al.*, 1974)
- \* Occulted Source

ionospheric radio scintillations. The geomagnetic planetary index  $K_p$ , another indicator of fine ionization structure in the ionosphere, was very low to moderate throughout May 13. Finally, solar activity, which influences both the ionosphere and solar wind velocity and structure, was low to moderate during the week preceding and including the occultation date.

For making a quantitative estimate of the electron content in the plasma turbules contained in the tail the power spectrum of intensity variations of the source was taken using the data around the transit time. Figure 5.4 shows the spectrum of the source 2204+29. The values have been normalized to the highest spectral density. Making the assumption that the thin screen scattering theory of Salpeter (1967) is valid for these observations the scale sizes of the turbulence can be calculated. The scale size is given by

$$a = \frac{v}{2 \pi f_2}$$

where  $v$  is the velocity of the diffraction pattern across the observer and  $f_2$  is the width of the scintillating power spectrum at the  $\exp(-0.5)$  points.  $f_2$  was found to be 0.923 Hz. as can be seen from Figure 5.4. Assuming that the plasma at this point in the tail had not yet been accelerated to typical solar-wind velocities, we can assign a velocity of  $v = 100$  km/sec. (Jockers 1981). Thus the scale size  $a = 17$  km, which is a much finer scale of turbulence than the typical values of 100 km - 1000 km for IPS in the

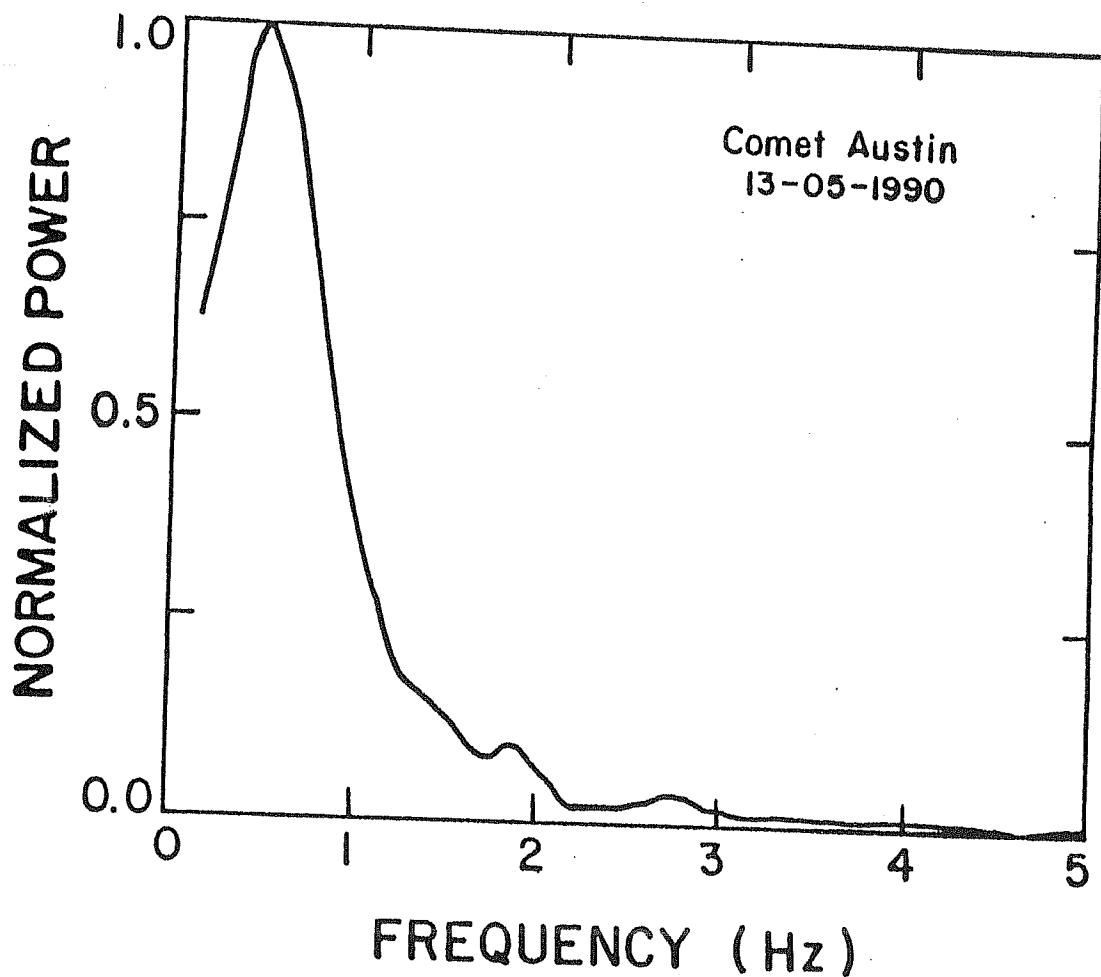


Figure 5.4 Shows the power spectrum of the source 2204 + 29 (3C441) during its occultation by the tail of comet Austin (1989 c1) in May 1990. The values have been normalized to the highest spectral density.

normal solar-wind. If the occultation were to take place at the edge of the tail where the tail plasma merges with the solar-wind then one can expect the velocities to approach that of the normal solar wind, i.e. around 400 km/sec. This would give a scale size  $a = 68$  km, which is also a much finer scale than expected in the normal solar wind close to 1 AU from the sun.

For a Gaussian electron density correlation function, the r.m.s phase deviation imposed across a wavefront emerging from a thin screen containing plasma turbulence is given by equation 2.1 as

$$\phi = (2\pi)^{1/4} r_e \lambda (aL)^{1/2} \Delta N$$

where :

$r_e = 2.82 \times 10^{-13}$  cm is the classical electron radius.

$a = 17 \times 10^5$  cm is the scale size.

$\lambda = 291$  cm is the operating wavelength.

$L = 10^{11}$  cm is the thickness of the screen (assumed, Jockers 1981).

$\Delta N =$  r.m.s electron density deviation.

For weak scattering, the scintillation index is given by equation 2.6 as  $m = \sqrt{2}\phi$ . In the present case  $m = 0.43$ , thus  $\phi = 0.304$  rad. Thus we get  $\Delta N \approx 6 \text{ cm}^{-3}$ . If the mean density in the tail is taken to be  $100 \text{ ions cm}^{-3}$  (Schmidt and Wegmann 1982.) then this value corresponds to a 6% modulation in the ion density at a distance of about 1 A.U. while the normal solar wind shows about 4% modulation around 0.1 A.U. Table 5.4 shows the scale sizes and rms electron density deviations that are obtained assuming

**Table 5.4: ESTIMATED SCALE SIZES AND  $\Delta N$  IN THE TAIL OF COMET AUSTIN**

VELOCITY	SCALE SIZE	$\Delta N$	REFERENCES
(Km/Sec.)	(Km.)	( $\text{cm}^{-3}$ )	
25	4	11	Scherb et al., 1990
100	17	6	Jockers, 1981
400	68	3	Avg. S.Wind Velo.

different velocities for the diffraction pattern. All scale sizes obtained lie in the range 4 km to 70 km which are much finer than those of IPS from the solar wind.

### 5.2.1 Discussions and Conclusions.

Since the occultation of the source took place only on one day, it was not possible to see if there was a gradient of scale sizes as one moved away from the axis of the comet. Nevertheless our value of 17 km for the scale sizes  $2^\circ$  from the tail axis is in good agreement with the observations of Comet Wilson by Slee *et al.* 1990. Since no photographs of the comet were available around this period an accurate estimate of the tail-lag, opening angle and thickness is not possible. It is possible that the actual tail-lag was much larger than the assumed  $3^\circ$  thus bringing the point of occultation much closer to the axis. A photographic study of the comet about a week prior to our observations (private communication, Jockers) has shown that the comet tail was showing rapid changes in pointing direction with the tail-lag varying from  $0^\circ$  to  $8^\circ$  in a few days, with the mean tail-lag in this period being approximately  $5.2^\circ$ . The occulted source would thus have been shining through the densest part of the plasma tail along the axis during our observations. A reanalysis of Halley's comet data (Alurkar *et al.*, 1986) taking into account the tail-lag was thus carried out in view of the new results obtained during the observations of comet Wilson (Slee *et al.*, 1990) and the present observations of comet Austin (Janardhan *et al.*, 1991).



With regard to the accuracies of the values of  $a$  and  $\Delta N$ , it is apparent from Table 5.4 that the velocity of the plasma is not known to better than a factor of four, causing scale sizes to have the same inaccuracy. This would in turn lead to a variation in  $\Delta N$  by a factor of two. This may become worse when the error in  $L$  is also taken into consideration.

### 5.3 Enhanced Scintillations Due to Comet Halley .

The recent observations of Comet Wilson (Slee *et al.*, 1990) during the occultation by it of two quasars, in May 1987 have shown the presence of two scintillating regimes in the plasma tail. One, a small-scale turbulence of 10 km to 40 km close to the axis and a second large-scale turbulence of 90 km to 350 km in the transition region where the tail merged with the solar wind. A second look at the observations of Alurkar *et al.*, 1986 was thus undertaken to see if a similar trend, if any, could be observed in the tail of Halley's Comet. Also the interaction of the radially directed solar wind with the comet's velocity causes the tail to deviate from the true radial direction by a few degrees. This tail-lag, which can be as much as  $5^\circ$  (Belton *et al.*, 1966), is very crucial in determining the correct occulting geometry and it was not allowed for in the observations of Alurkar *et al.*, 1986. The analysis has also provided an opportunity to recalculate more accurately and with better calibration the scintillation indices reported in the earlier paper (Alurkar *et al.*, 1986). The earlier values were overestimated as no allowance was made for the effect of the Automatic Gain Control (A.G.C.) in the receiving system during the 103

MHz observations in Dec. 1985.

Recent high spectral resolution  $\text{H}_2\text{O}^+$  emission spectra (Scherb *et al.*, 1990) have been used to measure the doppler shifts of emission lines and to determine directly the outflow velocities of the plasma in the coma and tail. These measurements report an average velocity of  $\text{H}_2\text{O}^+$  ions on December 16th, 1985 of about  $45 \text{ km sec}^{-1}$  between 0 to  $2 \times 10^6 \text{ km}$  from the nucleus. Photographic studies of displacements of features in cometary plasma tails have been used to infer velocities lying in the range 20 to  $250 \text{ km sec}^{-1}$  (Celnik and Schmidt-Kaler, 1987; Jockers 1981, 1985). Several theoretical studies of the morphology and formation of ion tail structures have also been conducted (Ip *et al.*, 1982, 1985; Miller, 1970; Schmidt *et al.*, 1979) and in the case of structures like rays - which are plasma sheets sandwiched between regions of opposite magnetic polarity - it has been derived (Ness and Donn., 1965) that tail-aligned flow speeds in these structures must vary linearly across a width of 1 to  $2 \times 10^5 \text{ km}$ . A photographic study (Saito *et al.*, 1987) has shown the presence of rays in Comet Halley's tail during mid Dec. 1985 to Jan. 1986. In a more recent work (Schmidt-Voigt 1989) have carried out a three dimensional time-dependant MHD model of cometary plasmas and have shown that tail condensations move down the tail with a velocity of 20 to  $70 \text{ km sec}^{-1}$ .

The occulting geometry during the present observations was such that accurate estimates of r.m.s. electron density variations ( $\Delta N$ ) and scale size ( $a$ ) could be obtained on each day during 16-21 Dec. 1985 at different distances with respect to the tail axis and nucleus, provided an estimate of

the velocity of the plasma at that point in the tail was made. These observations were made between  $6$  and  $30 \times 10^6$  km downstream of the nucleus where no accurate estimates or observations of ion velocities are available. The simplest assumption therefore would have been that of a single velocity of about  $50$  or  $100 \text{ km sec}^{-1}$  at all points across the width of the tail. Such an assumption, though, would have been unrealistic because one expects that at the interaction zone where the tail merges with the normal solar wind, the velocity must surely become equal to that of the undisturbed solar wind. In the following analysis therefore it is assumed that the velocity varied linearly across the tail having a value of  $50 \text{ km sec}^{-1}$  at the tail axis and attaining a value of  $385 \text{ km sec}^{-1}$  at the edge of the tail. This is based on the velocity measurements of  $\text{H}_2\text{O}^+$  ions in the tail of Halley's comet (Celnik and Schmidt-Kaler, 1987) which give a range of velocities of about  $50$  to  $140 \text{ km sec}^{-1}$  in the range  $6 \times 10^6$  and  $30 \times 10^6$  km downstream of the nucleus. The value of  $385 \text{ km sec}^{-1}$  was the average value of the solar wind velocity in the direction of the source 3C459 between 17th and 21st Dec. 1985, as measured at the three station IPS network in Japan, operating at 327 MHz. The distance of the occulted source (3C459) with respect to the tail axis on each day was calculated using the wind-sock model (Hajivassiliou and Duffett-Smith, 1987) with an opening angle of  $7^\circ$  as measured on a masked and contrast enhanced UK Schmidt photograph of the comet and a coma radius of  $10^{-3}$  AU.

### 5.3.1 Observations and Analysis - Comet Halley.

The observations were carried out with the 10,000 m<sup>2</sup> dipole antenna array (Alurkar *et al.*, 1990) which is located at Thaltej, near Ahmedabad, and has been fully described in the third chapter. The occulted source was regularly observed between mid-1984 and end of 1987 and Figure 5.5 shows a plot of the variation of scintillation index (r.m.s. flux/mean source flux) with solar elongation ( $\epsilon$ ) for all the data obtained in this period. The open circles represent the scintillation indices which have been averaged into one degree bins and then fitted by a third order polynomial - here marked by a continuous curve. This matches well with the values expected from the RKH model (Readhead *et al.*, 1978). The filled triangles represent the scintillation indices obtained during 16-21 December 1985, when the tail of comet Halley occulted the source. These values have not been considered when making the fit. A standard error bar is shown for each 10 degree bin, with the filled circles showing the mean value in each bin. It can be seen that there is an enhancement by a factor of about two in the scintillation index ( $m$ ) of 18th as compared to the expected level, of about 0.19 from the third order fit and about 0.18 as calculated from the RKH model. From Figure 5.5 it is apparent that this enhancement is very significant when compared with the scatter at a solar elongation of 90°. All the scintillation indices ( $m$ ) were obtained from the measured deflections, on a strip chart, of the Sine, Cosine and Scintillometer outputs after correcting the deflections of the Sine and Cosine channels for the effects of the AGC. The calibration procedure was that suggested by Duffett-Smith 1986. Table 5.5 gives the scintillation indices ( $m$ ) and other important

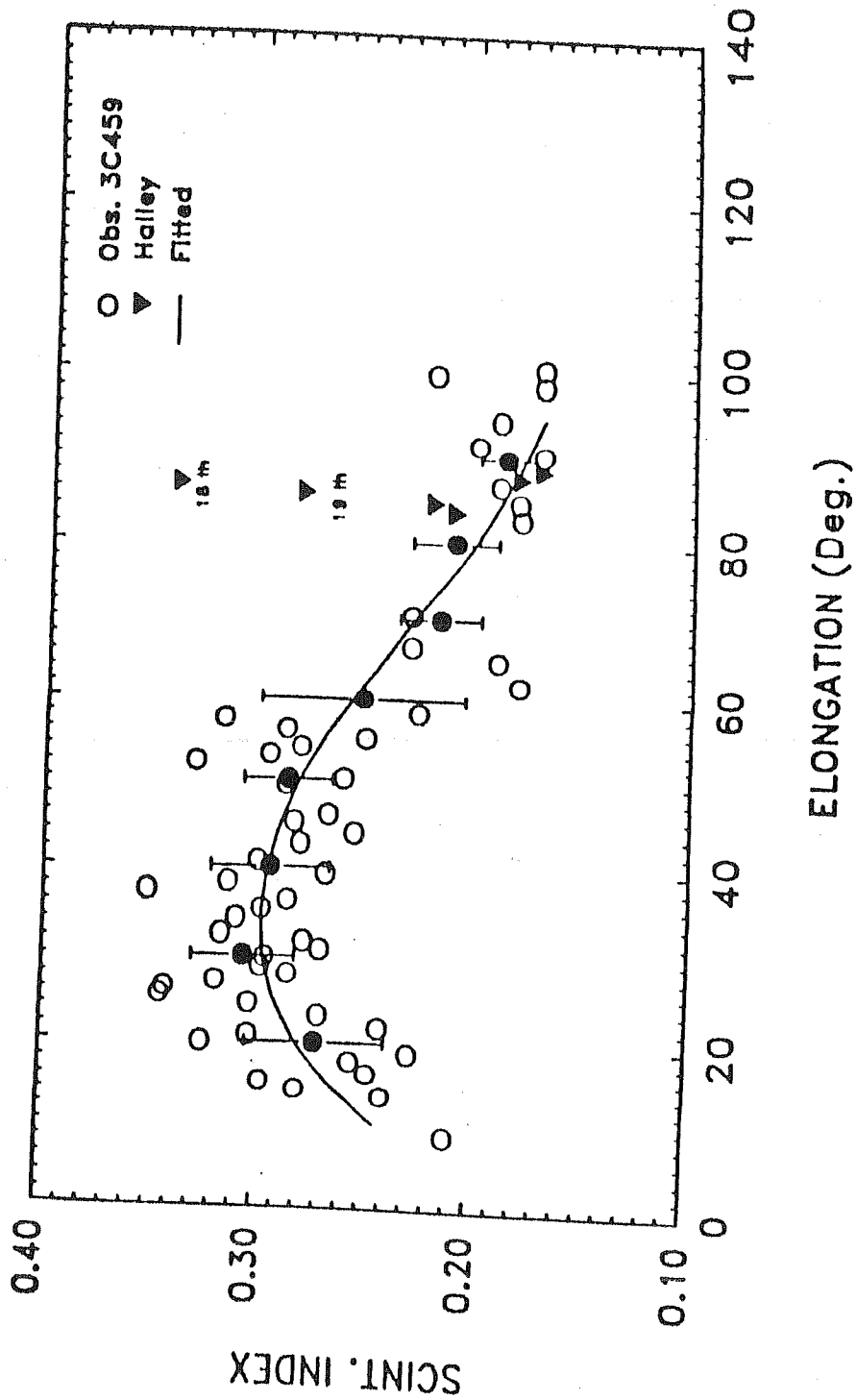


Figure 5.5

Shows the variation of scintillation index ( $m$ ) with solar elongation ( $\epsilon$ ) for the source 3C459. The open circles represent the observations of  $m$  while the solid line is a 3rd order polynomial fit to the data. A standard error bar has been shown for every  $10^\circ$  bin with the filled circles representing the mean value in each bin. The filled triangles are the scintillation indices obtained during the occultation of the source by comet Halley's plasma tail in December 1985.

**Table 5.5: SOURCE PARAMETERS DURING ITS OCCULTATION BY  
COMET HALLEY**

OCCULTED SOURCE		: 23 14 + 038 (3C459)			
GAUSSIAN DIAMETER ( $\theta$ ) <sup>#</sup>		: 0.41 " arc.			
MEAN SOURCE FLUX (103 MHz) <sup>*</sup>		: 43 Jy.			
DATE (1985)	TRANSIT (U.T.)	ELONG. ( $^{\circ}$ )	DIST. FROM NUCLEUS (AU)	DIST FROM AXIS ( $\times 10^5$ km)	OBS. SCINT. INDEX
16-12-85	1246	88.6	0.04	5.17	$0.17 \pm 0.015$
17-12-85	1242	87.6	0.08	2.59	$0.18 \pm 0.015$
18-12-85	1238	86.5	0.12	0.00	$0.34 \pm 0.015$
19-12-85	1234	85.5	0.14	1.29	$0.28 \pm 0.015$
20-12-85	1230	84.5	0.18	3.88	$0.22 \pm 0.015$
21-12-85	1226	83.5	0.20	5.17	$0.21 \pm 0.015$

<sup>#</sup> Estimated from 103 MHz. Observations using the RKH model.

<sup>\*</sup> From Readhead and Hewish 1974.

parameters calculated for 3C459 during its occultation between 16th and 21st December 1985.

On the 18th, when the scintillating power observed was maximum, the position angle (PSANG) of the comet tail was  $65.9^\circ$ . To bring out the crucial nature of the tail-lag, the tail axis has been plotted in Figure 5.6 at 10 hours UT on Dec. 18th, 0 hours UT and 10 hours UT on December 19th for three different values of tail-lag, ie.  $(65.9^\circ - 3^\circ)$ ,  $(65.9^\circ)$ , and  $(65.9^\circ + 3^\circ)$ . It can be seen that for the case when the tail-lag is  $-3^\circ$  the source was closest to the axis on Dec 18th during the transit at 1238 UT. On the other hand for a tail-lag of  $0^\circ$  the tail axis would not have passed across the source until Dec. 22nd, while for a tail-lag of  $+3^\circ$  the date of passage of the axis across the source would have been much before Dec. 18th. The tail-lag is thus a very crucial factor in deciding the actual time of passage of the source across the tail axis and the correct path of the source through the tail. Figure 5.7 shows the actual path of the source 3C459 through the comet tail for a tail-lag of  $-3^\circ$ . It can be seen that the source cut across the tail moving progressively downstream of the nucleus, being on the edge of the tail on 16th Dec. at a distance of 0.04 AU from the nucleus (measured along the axis), on the axis and 0.12 AU downstream on 18th and on the other edge and 0.2 AU downstream on the 21st.

The position angle of the tail axis was also measured from a contrast enhanced photographic plate taken with the U.K. Schmidt telescope. The original plate was a forty minute exposure on III aJ emulsion with a UG 395 filter (395 nm - 540 nm), with the mid point of exposure at 10h 14m 30s UT,

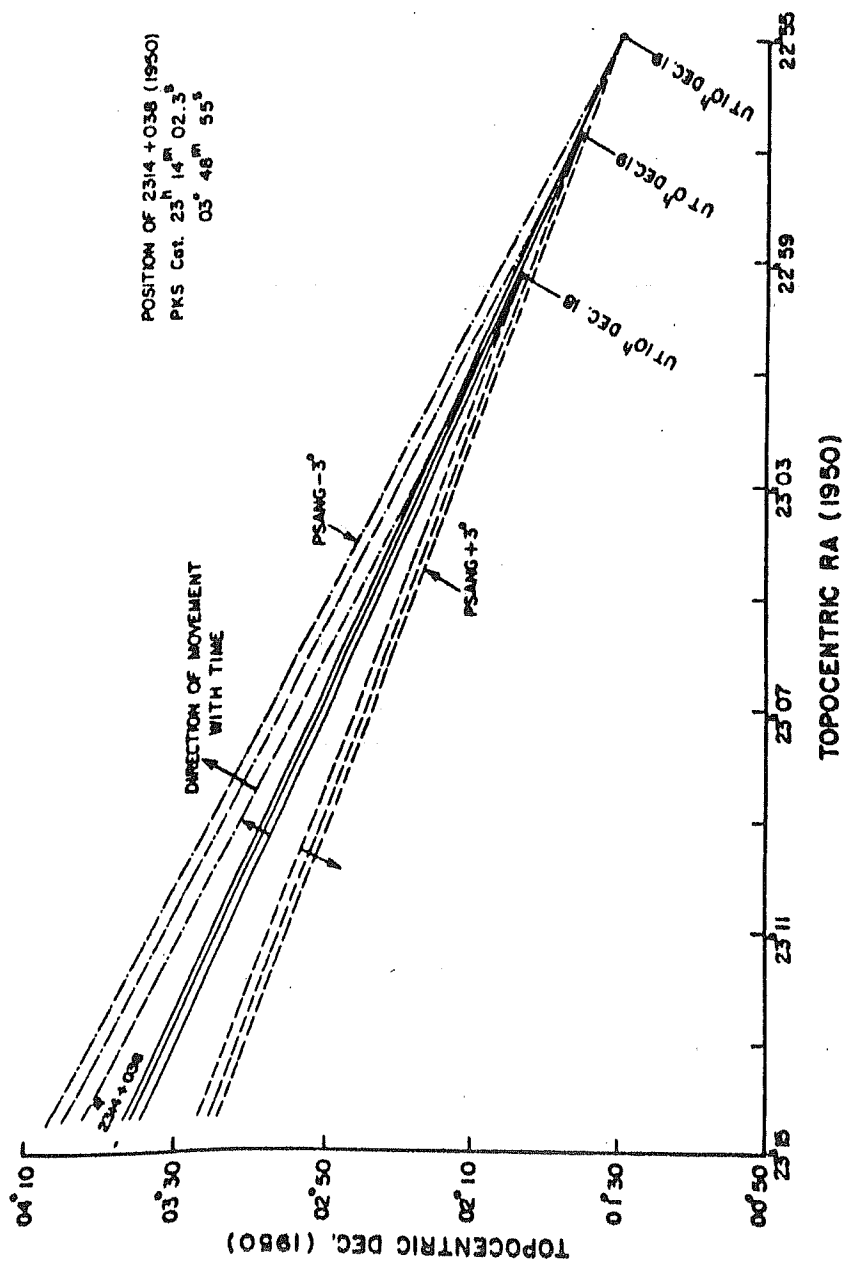


Figure 5.6 Shows the tail axis plotted for 3 different values of tail-lag Viz.  $-3^\circ$ ,  $0^\circ$ , and  $+3^\circ$  at  $10^h$  UT Dec. 18,  $0^h$  UT Dec. 19 and  $10^h$  UT Dec. 19 respectively. Note the position of the source close to the axis on Dec. 18 for a tail-lag of  $-3^\circ$ .



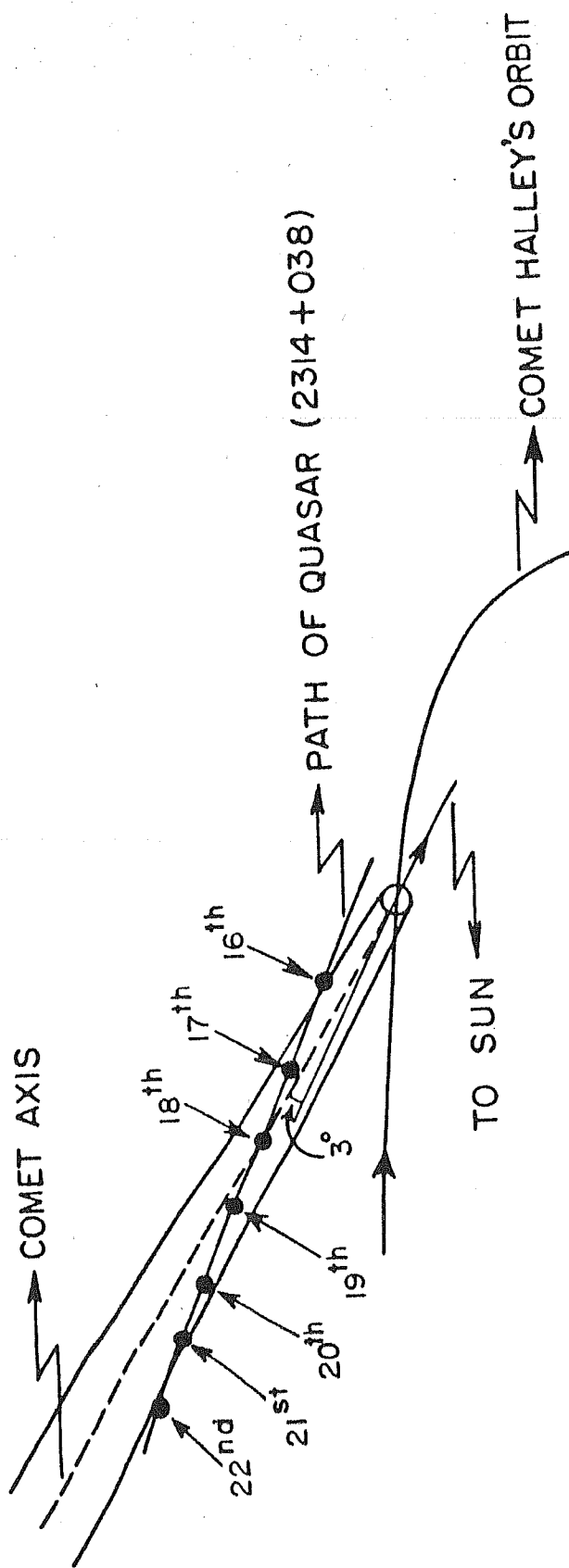
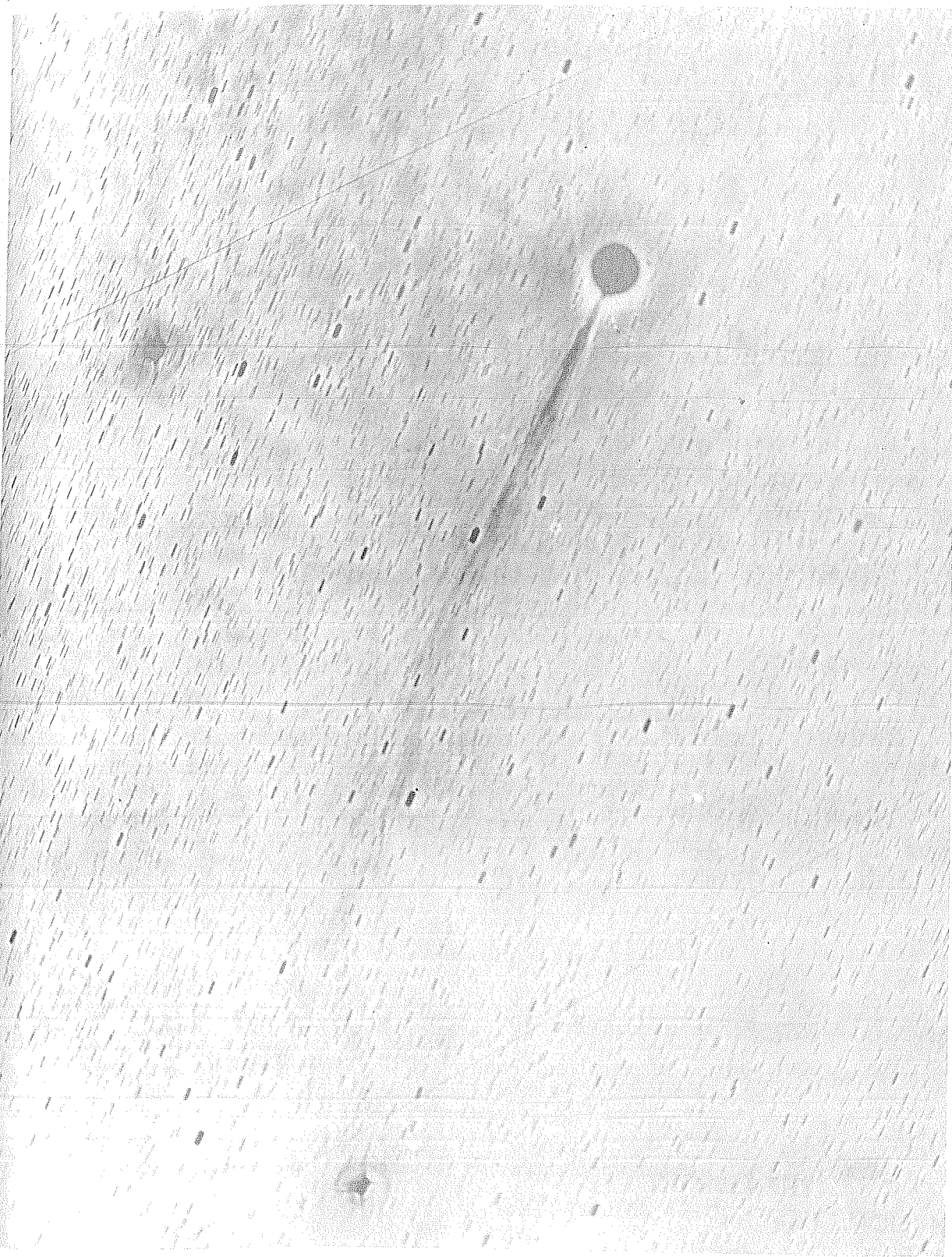


Figure 5.7 Shows the actual path of the source (3C459) through the tail of comet Halley. The azimuth of the anti-solar vector has been corrected by 3° to account for the tail-lag of -3° during these observations.

December 13th 1985. The original plate (J 10591T) was first copied using a high contrast unsharp-masking technique, whereby the original was exposed in a diffuse-light contact copy unit, on to continuous tone film. A 2 mm thick sheet of glass was used to separate the original and the film, so that an unsharp positive copy was obtained. This was exposed and processed to an appropriate density and contrast, and once dry was fixed to the glass side of the original plate. The effect of this was to mask the general large scale density variations, leaving the fine detail unaffected. A contact copy of the masked original was then made, using the diffuse-light copier again, and high contrast line film. The result was a film positive which was then used to create a paper print in the normal manner.

The cone of plasma emission extending out to about 30 arc minutes is well defined and is seen to converge sharply on to the nucleus as shown in Plate 4, which is a copy of the actual contrast enhanced UK Schmidt plate of Dec. 13th obtained by the above procedure. This cone of plasma is seen to cover a range of position angles from  $60.6^{\circ}$  to  $67.6^{\circ}$ . Taking the average of these two values, which is equal to  $64.1^{\circ}$ , to define the tail axis and comparing it with the anti-solar position angle of  $67.0^{\circ}$  on the evening of 13th. December 1985, a value of the position angle correction works out to be  $-2.9^{\circ} \pm 0.5^{\circ}$ . On this print the tail can also be traced out to about  $4.0^{\circ}$ , where the plasma is all seen to be contained within a transverse angular size of about  $7.0^{\circ}$ , corresponding to a linear size of approximately  $1.7 \times 10^6$  km.



**Plate 4** A contrast enhanced copy of the UK Schmidt plate of comet Halley on Dec. 13, 1985  
(UK Schmidt Telescope, Royal Observatory, Edinburgh).

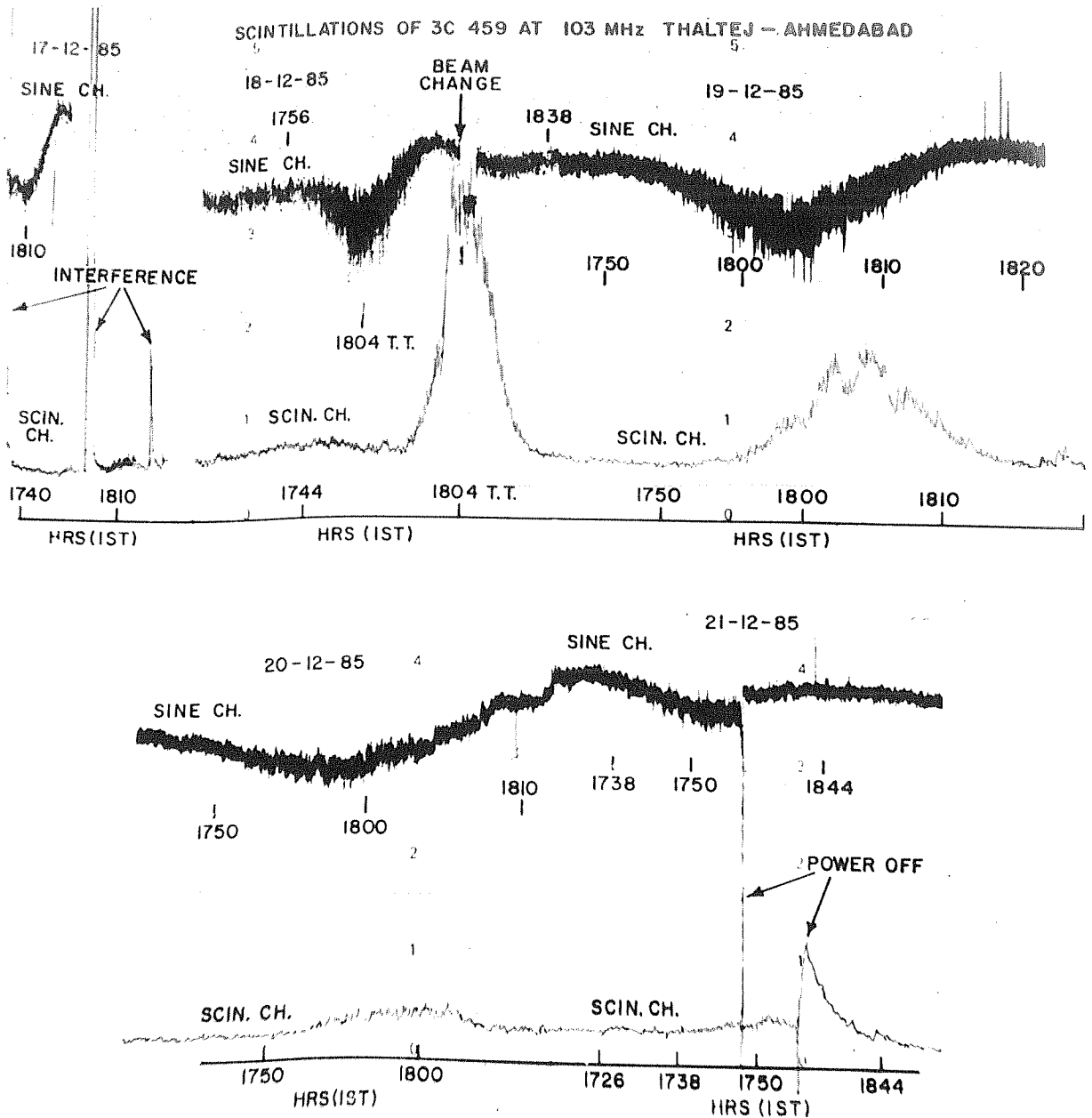


Plate 5 Shows the chart recordings of the source 3C459 (2314+03) between 17 and 21 Dec. 1985 when the tail of comet Halley swept in front of it. The three traces shown are the sin, cos and scintillometer outputs of the correlation receiver.

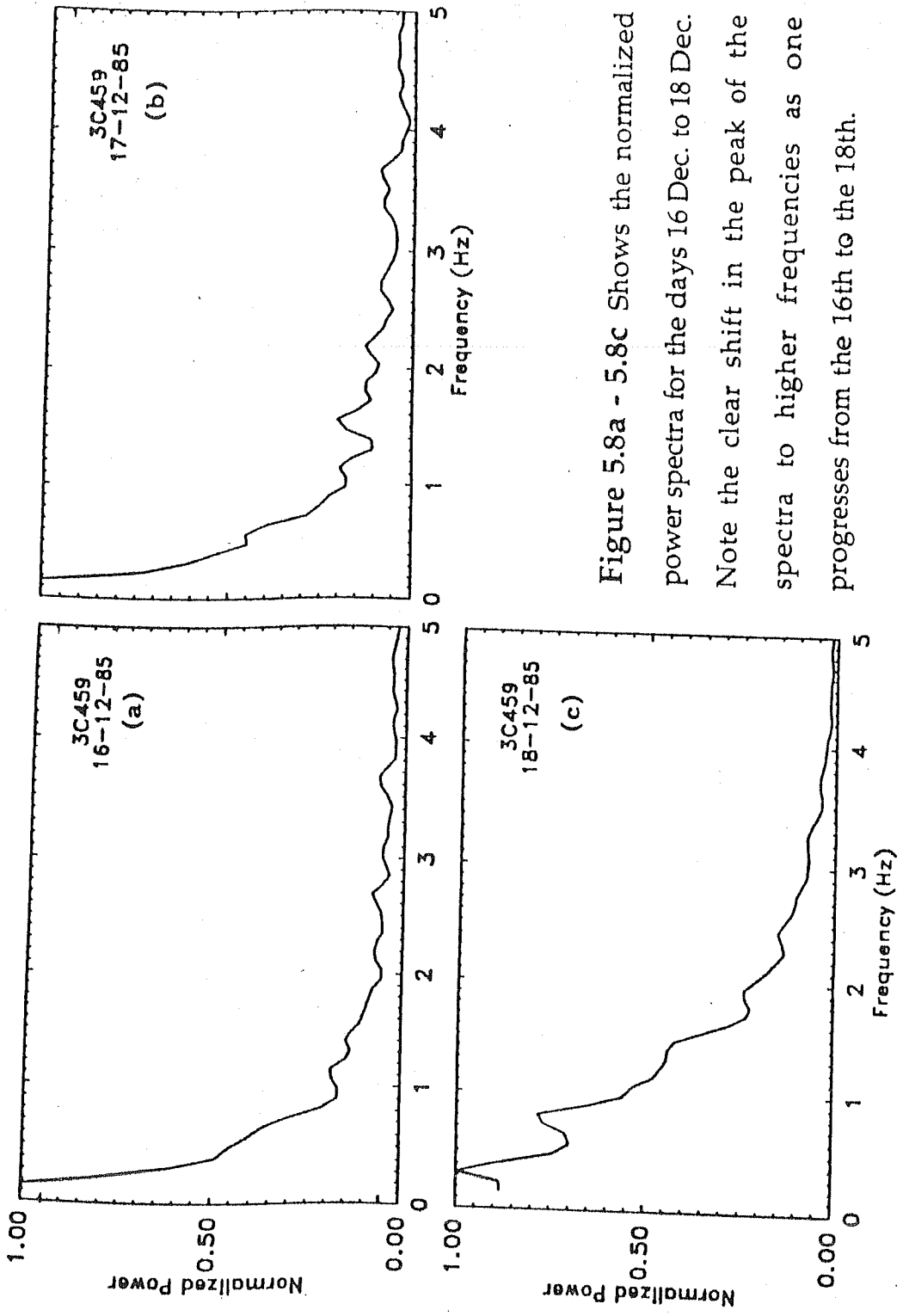


Figure 5.8a - 5.8c Shows the normalized power spectra for the days 16 Dec. to 18 Dec. Note the clear shift in the peak of the spectra to higher frequencies as one progresses from the 16th to the 18th.

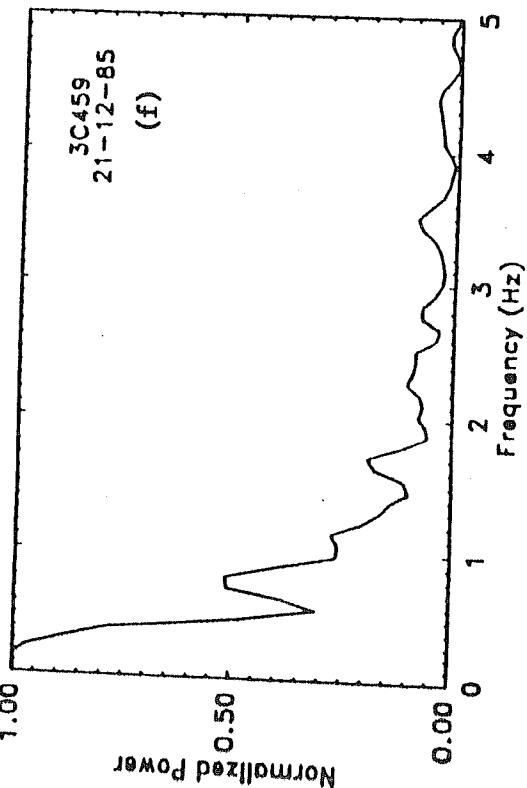
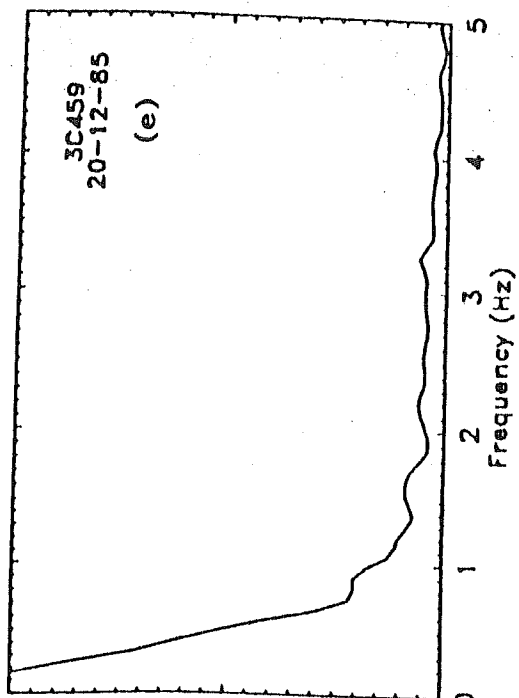
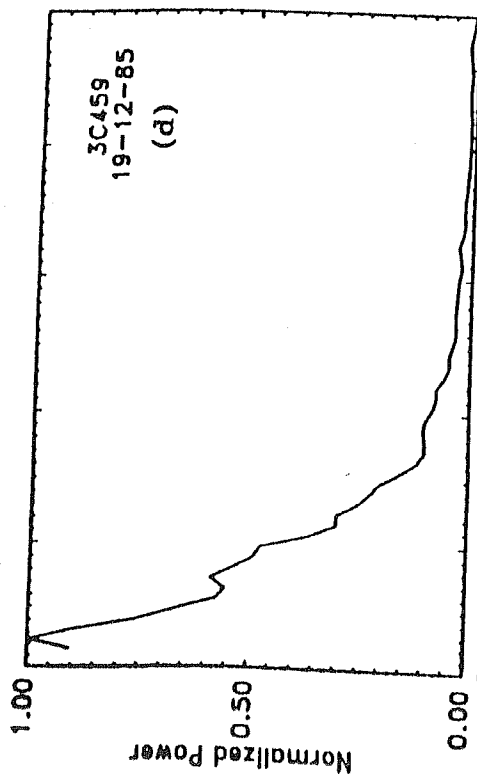


Figure 5.8d - 5.8f Shows the normalized power spectra for the days 19 Dec. to 21 Dec. Note the clear shift in the peak of the spectra to lower frequencies as one progresses from the 19th to the 21th.

Plate 5 shows the actual chart recordings of the source 3C459 between December 16 and 21. The three traces shown on each day are the Sine, Cosine and Scintillometer outputs of the correlation receiver. Figure 5.8a - 5.8f shows the power spectra obtained for each day between 16th and 21st December. The power spectra were computed by subtracting a Hanned spectrum of 10 minutes of data off-source, from a Hanned spectrum of 10 minutes of data on-source. The on-source data was taken five minutes on either side of the transit time on each day from the available on-source data of about 15 minutes. The data was sampled at 20 Hz. and digitized using a 12 bit,  $\pm 5$  V A/D converter (Alurkar *et al.*, 1989) and stored on a magnetic tape for analysis. On the 21st, however, due to a power failure (see Plate 5) occurring during the transit of the source through the beam, only  $\pm 2$  minutes of data was available on-source. The spectrum of the 21st was thus obtained by subtracting a Hanned spectrum of 10 minutes off-source data from a Hanned spectrum of 4 minutes on-source data. All the spectra were normalized to the highest spectral density and had a frequency resolution before Hanning of 0.0813 Hz. It can be seen that the spectrum of 18th has a peak around 0.33 Hz which slowly decayed out to about 3.5 Hz. This is a very typical IPS spectrum. On the 16th, when the source was at the edge of the tail, the spectrum decayed much faster than on the 18th, with the peak being around 0.16 Hz. The decay on the 17th is seen to be slower, though the peak does not shift. On the 19th the source was still close to the axis and the spectrum showed a less rapid decay than that on 16th and 17th and went out to about 2.5 Hz, with the peak at about 0.24 Hz. On the 20th the decay was a little faster than that of the 19th and went out

to about 1.5 Hz. The spectrum of 21st had much more noise, as compared to the other days, but it clearly had some scintillating power.

It is important to note the clear shift in the peak from 0.16 Hz. on the 16th to 0.33 Hz. on the 18th, when the source was closest to the axis, and 0.24 Hz. on the 19th. If the shift in the peak to higher frequencies were not present then it would have meant that other processes like ionospheric scintillation or gain changes were responsible for obscuring the true peak due to the plasma in the tail. Table 5.6 gives the spectral widths measured on each day from the power spectrum and the r.m.s. phase deviation imposed on the wave emerging from the screen.

Assuming that the thin screen theory developed by Salpeter (1967) is valid for these observations the correlation length or scale size ( $a$ ) and the rms phase deviation ( $\phi$ ) can be calculated in the manner already described. For a circularly symmetric Gaussian electron density correlation function the r.m.s. phase deviation imposed across the wave emerging from the screen is again given by equation [2.1]. The thickness of the screen ( $L$ ) is taken to be  $1.7 \times 10^6$  km. This value is obtained by assuming that the thickness of the tail is equal to the width measured on the contrast enhanced U.K. Schmidt photograph of 13th December. Also for weak scattering we know that the scintillation index ( $m$ ) is given by the expression 2.6. If one assumes that the velocity of the plasma in the tail of the comet varies as described earlier, from a value of  $50 \text{ km sec}^{-1}$  at the axis to  $385 \text{ km sec}^{-1}$  at the edge, then the scale sizes and  $\Delta N$  of the turbulence can be calculated using the above equations. Table 5.7 summarizes these



**TABLE 5.6: SPECTRAL WIDTHS AND RMS PHASE DEVIATIONS**

DATE	SPECTRAL WIDTH - $f_2$	RMS PHASE - $\Phi$
( 1985 )	( Hz )	( Rad. )
16-12-85	0.23	0.12
17-12-85	0.31	0.13
18-12-85	0.87	0.24
19-12-85	0.56	0.20
20-12-85	0.34	0.16
21-12-85	0.49	0.15

**TABLE 5.7: SCALE SIZES & RMS ELECTRON DENSITY DEVIATIONS  
FOR VARYING VELOCITIES**

DATE	DIST. FROM AXIS <sup>+</sup> ( $\times 10^5$ km )	VELOCITY <sup>#</sup> ( km sec <sup>-1</sup> )	SCALE SIZE ( km )	RMS DENSITY ( $\Delta N$ cm <sup>-3</sup> )
16-12-85	5.17	385.00	266	0.43
17-12-85	2.59	192.54	99	0.77
18-12-85	0.00	50.00	9	4.68
19-12-85	1.29	96.23	27	2.26
20-12-85	3.88	288.77	135	0.81
21-12-85	5.17	385.00	125	0.79

+ Calculation uses a correction of  $-3^\circ$  for the tail-lag.

# These velocities were obtained by assuming a linear gradient in velocities as one moved from the tail axis to the edge.

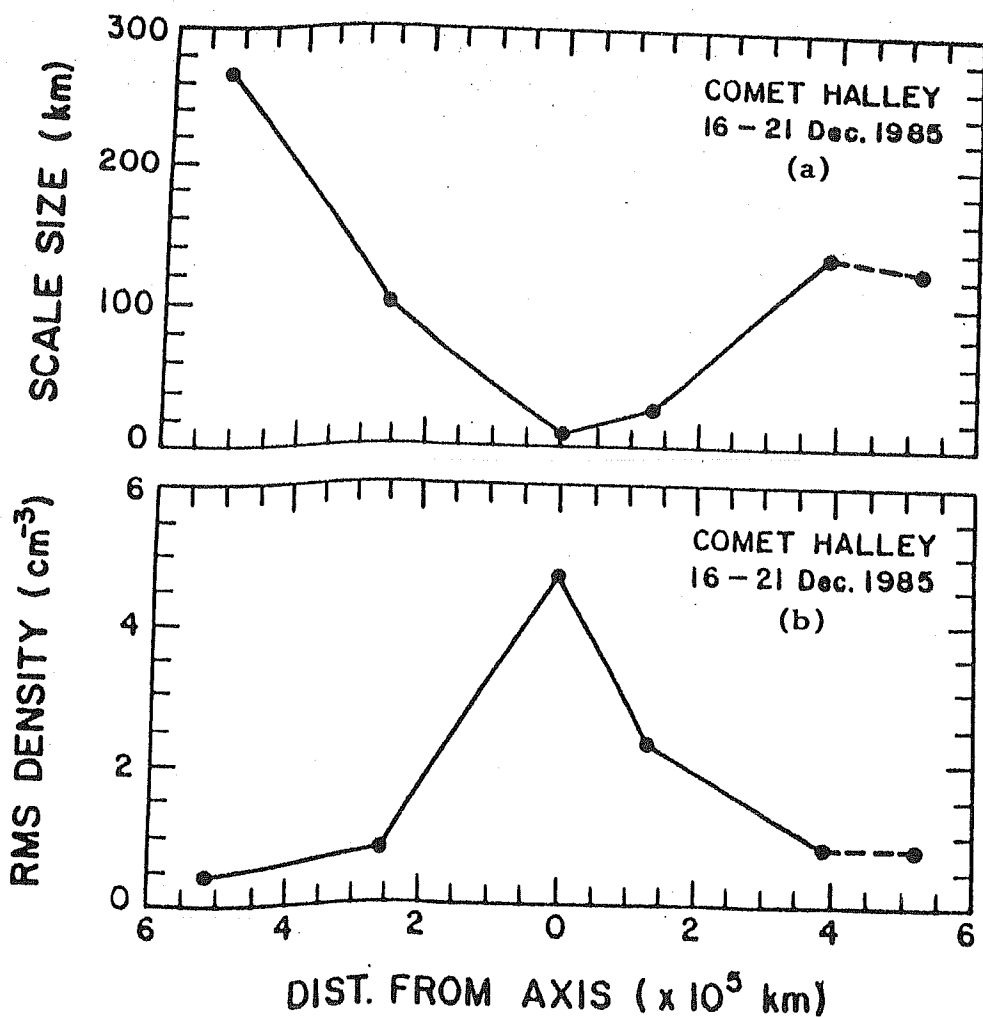


Figure 5.9a - 5.9b Shows the variation of scale size (a) and rms electron density deviations ( $\Delta N$ ) as a function of distance on either side of the comet tail axis. The dotted line is drawn to the last point due to the spectrum of the 21st being calculated with just four minutes of on source data as compared to 10 minutes for the other dates.

values while Figure 5.9a - 5.9b plots the variation of scale sizes and  $\Delta N$  as a function of distance away from the axis. It can be seen that on and near the axis (during 18th and 19th) the scale sizes are in the range 9 km to 27 km and these are much finer than those expected in normal IPS from the solar wind. On the 16th and 17th scale sizes are in the range 100 to 266 km which are normal IPS scale sizes. Again on the 20th when the position of the source with respect to the tail axis was neither at the edge nor on the axis it yields a scale size of 135 km,  $\Delta N$  between  $2.3 \text{ cm}^{-3}$  and  $4.7 \text{ cm}^{-3}$  near the axis and between  $0.4 \text{ cm}^{-3}$  and  $0.8 \text{ cm}^{-3}$  near the edge. Since the spectrum of 21st has been derived from a very few number of blocks of data near transit, these points have been marked by a dotted line in figures 5.8a and 5.8b.

### 5.3.2 Estimation of the Amount of Enhancement from Other Causes.

Some groups of observers (Ananthakrishnan *et al.*, 1987) have expressed the opinion that the observed enhancements in scintillation seen during the the 103 Mhz observations could have been caused by an unfortunately located corotating stream which swept past the line of sight. Using available spacecraft data during that period an attempt was made to see if this was indeed the case.

Figure 5.10 shows the spacecraft data available from the Interplanetary Medium Data Book - Supplement 4, 1985 - 1988, NASA Goddard. The data showed that a shock reached the earth around midday

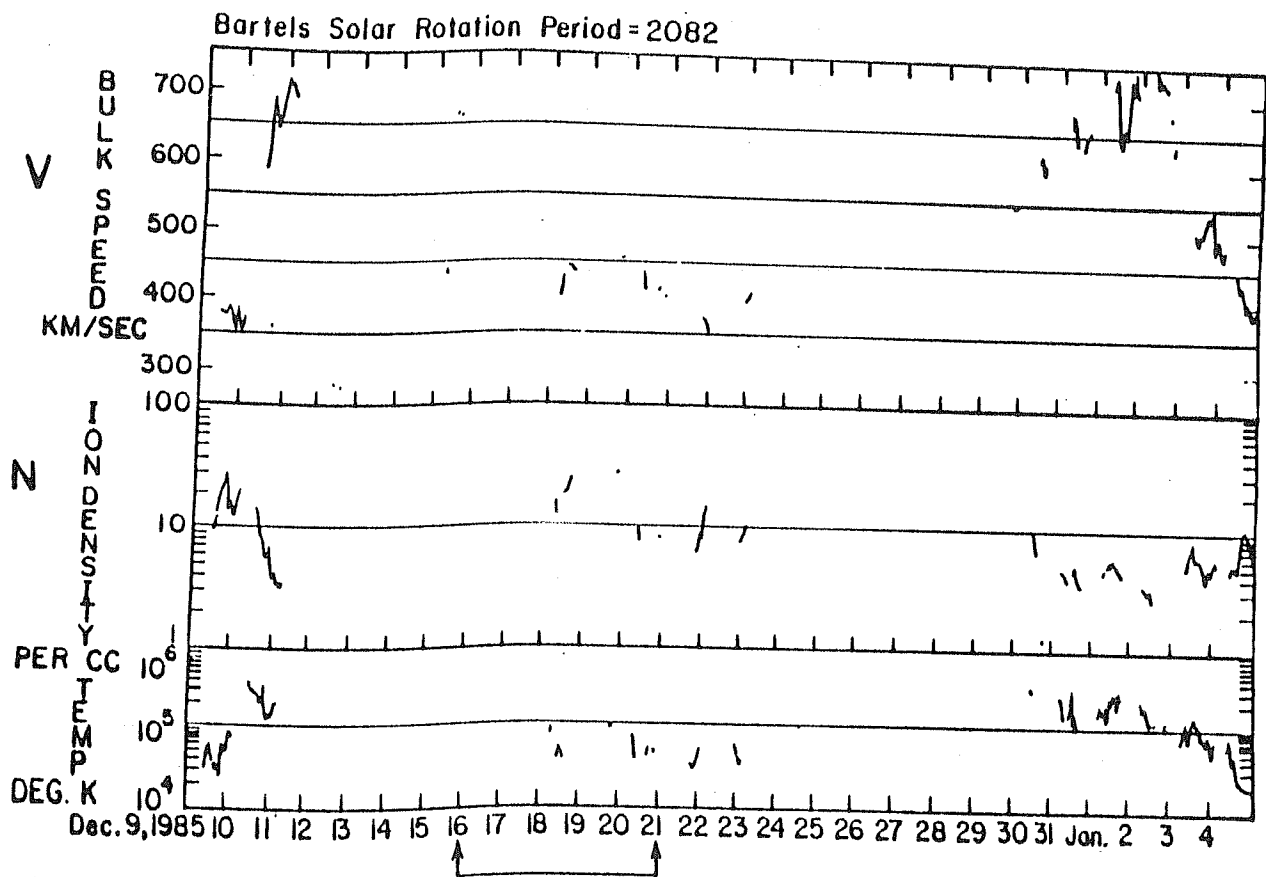


Figure 5.10 Shows spacecraft data available during December 1985. The bulk velocities, ion densities and temperature are shown on different days. The period of interest has been marked by arrows.

# PRELIMINARY H-ALPHA SOLAR SYNOPTIC CHART

CARRINGTON ROTATION NUMBER 1769

(November 20 to December 17, 1985)

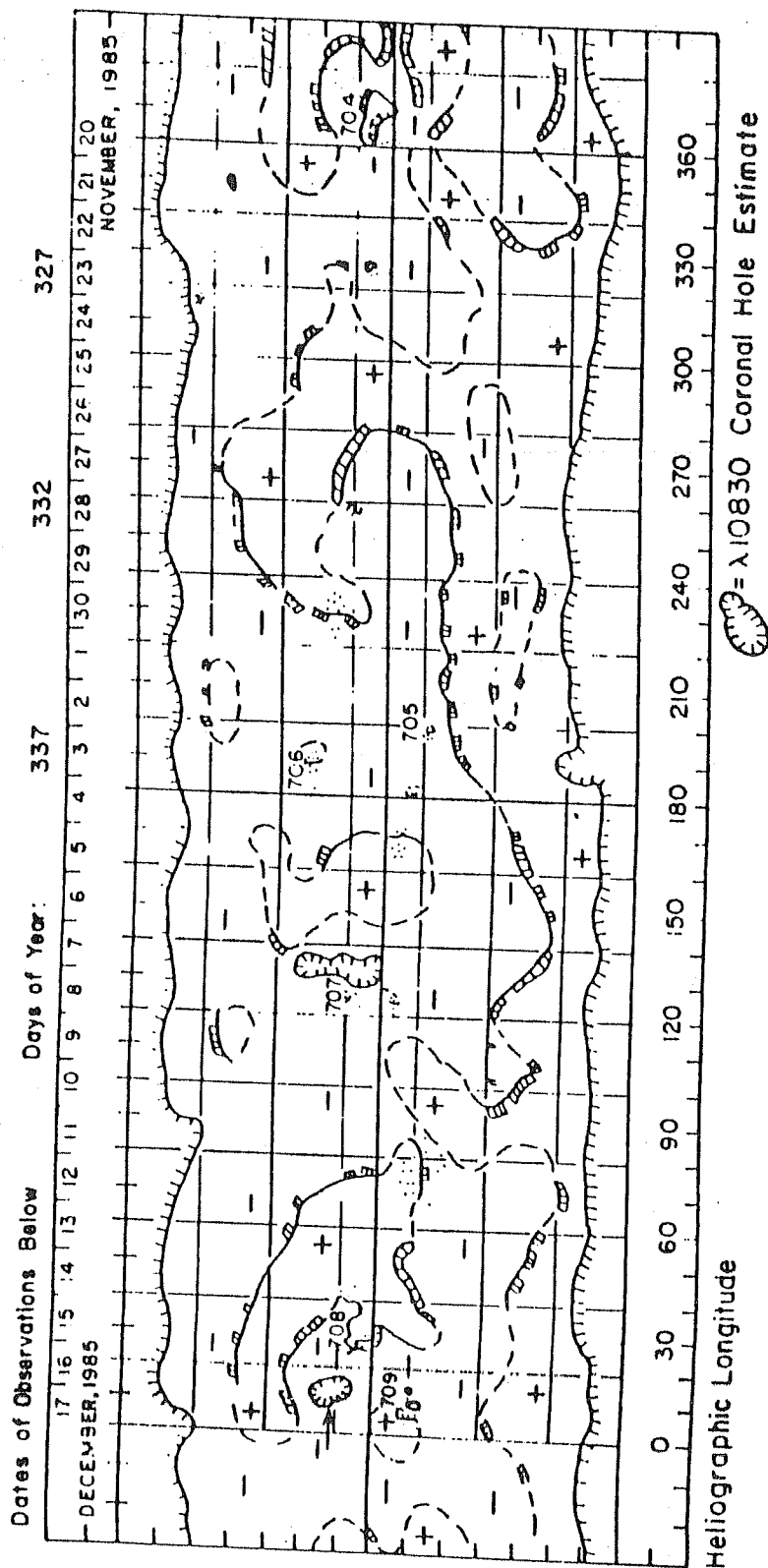


Figure 5.11 Shows the H-Alpha solar Synoptic Chart for December 1985 showing the positions of coronal holes identified at 10830 Å. Marked by an arrow on the left hand side close to active region 708 is a coronal hole which is located in a position convenient to cause a corotating stream which could have rotated past the line of sight to 3C459.

on December 18th. The bulk velocity  $V$  increased to  $450 \text{ km sec}^{-1}$ , the ion density increased to at least  $20 \text{ cm}^{-3}$  which is roughly twice the quiet value, and the interplanetary magnetic field rose to more than  $12 \gamma$  which is more than twice the average value. The magnetic  $K_p$  index showed a sudden commencement around 0600 on Dec. 18th followed by a moderately strong magnetic storm (see Solar Geophysical Data Handbook - Feb. 1986). The solar source of this disturbance was probably the coronal hole at central meridian on 16th December, adjacent to the active region 708 as seen from the H-Alpha Solar Synoptic Chart shown in Figure 5.11. The disturbance probably left the sun about four days earlier so that it would have been most pronounced to the East of the Sun-Earth line, thus affecting 3C459 more than sources to the West of the sun. Figure 5.10 also shows a high speed stream and its associated enhancement of  $N$ , which corotated past the earth between 9th and 14th December 1985. This stream was due to the coronal hole at central meridian on 7th December and is clearly a CIR as  $N$  peaked one day before  $V$  increased.

From these data it is apparent that the enhancement in scintillation observed on the 18th December was not due to a CIR. Recent work (Lindblad, 1990) has shown that the measured lifetime of a plasma stream at the earth orbit is about three days if the parent coronal hole has a latitudinal extension of around  $45^\circ$ . The parent coronal hole during our observations was no more than  $20^\circ$  in latitudinal extent and could not have caused the observed effects over a period of 6 days. Also since our observations are limited to once every 24 hours, it is most likely that streams less than two days in extent will be missed altogether. Moreover it

is known from many observations (Niedner *et al.*, 1978; Jockers, 1981; Brandt *et al.*, 1980) that the interaction of a cometary plasma tail with a CIR will cause rapid changes of the ion-tail pointing direction. Observations of Halley's comet did not indicate any such deflections.

The same equations can now be used to calculate the rms phase deviation ( $\phi$ ) assuming that the enhancements were entirely caused by the shock-front which gave rise to the sudden commencement geomagnetic storm on the 18th. Using the value of the width of the observed spectrum and the spacecraft velocity of  $450 \text{ km sec}^{-1}$  the scale size of the irregularities in the shock-front turns out to be about 82 km. A detailed study of interplanetary disturbances in the solar wind caused by the strong flare activity of August 2, 4 and 7, 1972 has been made using the data obtained by Pioneer 9, and upper limits on the thickness of these shock-fronts have been estimated (Dryer *et al.*, 1976) to be  $\approx 10^5 \text{ km}$ . The rms electron density deviation  $\Delta N$  in the solar wind is known to be about  $0.1 \text{ cm}^{-3}$  at 1 AU and  $0.4 \text{ cm}^{-3}$  at 0.1 AU representing respectively a 1% and 4% modulation (Hewish, 1971) of the mean ion density  $N$ . The spacecraft data showed an increase in  $N$  to  $20 \text{ cm}^{-3}$  and since the scintillation index  $m$  is  $\propto \Delta N$  and  $m$  is correlated with  $N$  (Houminer and Hewish, 1974) the value of  $\Delta N$  on the 18th December can be taken to be 2 percent of the observed value. Thus  $\Delta N = 0.4 \text{ cm}^{-3}$  will be a reasonable estimate. Using these values the rms phase deviation imposed on the wavefront by the interplanetary shock will be  $\phi \approx 0.015$  radian giving a scintillation index ( $m$ ) equal to 0.021. The background scintillation index at a solar elongation of around  $90^\circ$ , as seen from Figure



**Table 5.8: ESTIMATED ENHANCEMENTS FOR DIFFERENT  $\Delta N$**

OBSERVED SCINT. INDEX : 0.34 (18/12/85).	
EXPECTED SCINT. INDEX : 0.19	
THICKNESS OF SHOCK : $10^5$ km (Pioneer 9)	
RMS $\Delta N$ ( $\text{cm}^{-3}$ )	SCINTILLATION. INDEX (CALCULATED)
0.4	0.21
0.8	0.23

5.5, is 0.19. Thus the expected scintillation index on the 18th would be 0.21. Table 5.8 shows the scintillation index calculated for various values of  $\Delta N$ .

The above analysis shows that in the case of the comet Halley observations of December 1985 - the presence, on the day of maximum observed scintillation, of a shock-front that gave rise to the moderately strong sudden-commencement type geomagnetic storm, had around 10% contribution to the observed enhancements in scintillation. This is within the scatter at  $90^\circ$  as seen from Figure 5.5. The observed effects between 16 and 21 December (Alurkar *et al.*, 1986; Janardhan *et al.*, 1991b) were thus caused mainly due to the plasma tail of the comet sweeping across the line of sight in front of the source during the observations. Even if the value of  $\Delta N$  was taken to be  $0.8 \text{ cm}^{-3}$ , (representing a 4% modulation of the mean ion density which is the case in the quiet solar wind at 0.1 AU) the expected scintillation would turn out to be 0.23. Noting that the expected value of scintillation index is 0.19, this enhancement is not significant.

### 5.3.3 Results and Discussions.

A comparison of these results with those of Slee *et al.*, 1990 for Comet Wilson is instructive. Slee *et al.*, derive a fine scale turbulence between 10 and 40 km for a range of velocities between 100 and 400  $\text{km sec}^{-1}$ , while the present results - which are statistically more significant due to the larger number of observations across the tail - suggest that the actual scale size is a more sensitive function of the velocity than was seen earlier.

One can now say that a fine scale regime of scale sizes dominated by high values of  $\Delta N$  exists along and close to the axis of cometary plasma tails. The  $\Delta N$  in this region is about an order of magnitude greater than that expected in the normal solar wind at heliocentric distances of about 1 AU (Cohen *et al.*, 1967). A larger scale size regime along and close to the edge is also seen to exist but the range could be from 100 km to 265 km. This region is dominated by a value of  $\Delta N$  which is much closer to the normal solar wind value. The analysis also suggests that the physical processes at work close to the axis of the comet are independent of the solar wind and hence show different characteristics, while as one moves towards the edges of the plasma tail, the solar wind effects begin to dominate and slowly damp out the effects of the processes dominant at the axis. A detailed magneto-hydrodynamic model study though will be required before anything definite could be said about the actual processes at work.

The post perihelion observations (Slee *et al.*, 1987) of comet Halley in March 1986 measured a  $\Delta N$  of  $1.9 \text{ cm}^{-3}$  at a distance of 0.036 AU downstream of the nucleus. If one were to make an allowance of about  $+3^\circ$  in this case for the post perihelion period, the point of occultation would have been near the edge and not along the axis of the comet. Also the width of the tail measured from the masked and contrast enhanced photo of the comet (Plate 3) is greater than the value used by (Slee *et al.*, 1987) by a factor of about 3.5. If this difference in width is corrected for, the value of  $\Delta N$  for the observations of (Slee *et al.*, 1987) would have to be reduced by a factor of  $\sqrt{3.5}$ , giving  $\Delta N = 1 \text{ cm}^{-3}$ . This value is thus identical to the value of  $\Delta N = 1 \text{ cm}^{-3}$  obtained from the present observations. This value is the

**TABLE 5.9: SCALE SIZES AND RMS ELECTRON DENSITY DEVIATIONS  
FOR A SINGLE VELOCITY OF 100 km sec<sup>-1</sup>**

DATE	DIST. FROM AXIS ( $\times 10^5$ km )	SCALE SIZE ( km )	RMS DENSITY ( $\Delta N$ cm <sup>-3</sup> )
16-12-85	5.17	69	0.85
17-12-85	2.59	51	1.07
18-12-85	0.00	18	3.31
19-12-85	1.29	28	2.22
20-12-85	3.88	47	1.38
21-12-85	5.17	33	1.55

average value for the dates 16, 17, 19, 20, and 21 when the source was not close to the axis of the tail. Thus it appears that provided the rate of ionization of nuclear material remains unchanged over a period of few months, there was no radial variation in  $\Delta N$  in the off axis region of the tail, though more observations of a similar nature would be required to confirm this. This is consistent with the model (Ip and Axford, 1982) of ion compositions for a Halley type comet at a distance of 1 AU from the sun. The model predicts negligible dependance of ion density on axial distance beyond  $10^6$  km downstream of the nucleus.

Even if one were to assume a velocity of  $100 \text{ km sec}^{-1}$  for the plasma throughout the tail, a fine scale turbulence zone is seen on and near the axis. The scale sizes lie between 18 km and 28 km and  $\Delta N$  between  $3.3 \text{ cm}^{-3}$  and  $2.2 \text{ cm}^{-3}$ . The zone near the edge though, is not so distinct with scale sizes and  $\Delta N$  in the range 33 - 70 km and  $1.6 \text{ cm}^{-3}$  to  $0.9 \text{ cm}^{-3}$  respectively. In conclusion, it can be said that evidence for the presence of a fine scale turbulence dominated by high values of  $\Delta N$  along and near the axis of cometary plasma tails is strong. Table 5.9 gives the scale sizes and  $\Delta N$  obtained for comet Halley by assuming a constant velocity of  $100 \text{ km sec}^{-1}$  throughout the tail. Even in this case one sees distinct fine scale sizes and high rms  $\Delta N$  along and close to the comet tail axis.

## 5.4 Conclusions.

The spectral analysis of the IPS data taken during the occultations discussed in this chapter clearly shows that cometary plasma can indeed contain a level of turbulence, much in excess of that in the normal solar wind at 1 AU, and cause enhanced scintillation observable at large solar elongations. The analysis also indicates that a gradation of scale sizes and rms  $\Delta N$  exists in cometary tails, with the region around the axis of the tail being dominated by fine scale sizes and large values of  $\Delta N$  as compared to the quiet solar wind at similar distances. The tail-lag is shown to be very crucial in determining the accuracy of occultation and also the correct path of the source through the tail. Also, when the observations of comet Austin were carried out, a tail-lag of  $+3^\circ$  was assumed. This geometry thus put the occulted source  $2^\circ$  off the comet axis on the day of the occultation. The inferred  $\Delta N$  though was  $6 \text{ cm}^{-3}$  suggesting that the occulted source was much closer to the axis. It was learnt later (private communication, Jockers) that the tail of comet Austin was showing rapid changes in pointing direction, a week prior to our observations, and the tail-lag on 13th May could have been about  $5.3^\circ$ . This clearly shows the crucial nature of the tail-lag and also reenforces the fact that cometary tail plasma can indeed cause enhanced interplanetary scintillations.

Estimates of the amount of scintillation caused by a shock front which hit the earth on the 18th December, though, have to be treated with a great deal of caution. This is because the available spacecraft data is very sketchy and cannot be given too much weightage. Assuming that the

mean curve in Figure 5.5 represents average conditions in 1985 and noting that the mean density at 1AU for that year, based on Helios data, was  $7\text{cm}^{-3}$  (See - Physics of the Inner Heliosphere, 1990, pp 160) the relation  $g \propto (N/N_0)^{\frac{1}{2}}$  (Tappin, 1986), where  $g$  is the enhancement factor,  $N$  is the observed density and  $N_0$  is the mean value of density for the year 1985, gives  $g = (20/7)^{\frac{1}{2}} = 1.7$ . Our observations of scintillation index on the 18th give  $g = (0.34/0.19) = 1.8$ . These values being so close seem to suggest that the effects from the comet are not significant. The assumption here is that the transient is sufficiently extended to cover the relevant portion of the line of sight which may not be the case because the latitudinal extent of the coronal hole that is suspected to have led to the transient (Figure 5.11) was small enough so as to have been completely missed by a transit instrument. Recent work (Lindblad, 1990) has shown that the measured lifetime of a plasma stream at the earth's orbit is about three days if the parent coronal hole has a latitudinal extension of around  $45^\circ$ . The parent coronal hole during our observations was no more than  $20^\circ$  in latitudinal extent and could not have caused the observed effects over a period of 6 days. Also, since our observations are limited to once every 24 hours, it is most likely that streams less than two days in extent will be missed altogether. Moreover, it is known from many observations (Niedner et al., 1978; Jockers, 1981; Brandt et al., 1980) that the interaction of a cometary plasma tail with a CIR would cause rapid changes of the ion-tail pointing direction. Observations of Halley's comet did not indicate any such deflections.

# Chapter - VI

## SCOPE FOR FUTURE WORK USING THE ENHANCED THALTEJ TELESCOPE

### 6.1 Angular Distribution of Radio Sources and IPS Surveys.

The dipole array at Thaltej has only just had its physical area enhanced from  $10,000 \text{ m}^2$  to  $20,000 \text{ m}^2$ . The entire receiving system is also undergoing modification, with 32 total power receivers with scintillometers being built so that all the available 32 beams of the Butler matrix can be used simultaneously to scan the sky. Moreover during the expansion of the physical area of the array and the upgrading of the receiving system, most of the drawbacks encountered with the  $10,000 \text{ m}^2$  array have been effectively dealt with. The  $20,000 \text{ m}^2$  telescope is thus expected to be fully operational, with its full complement of receivers and scintillometers scanning the entire sky in the declination range  $6^\circ \text{ S}$  to  $54^\circ \text{ N}$  once every 24 hours, by the middle of 1992.



The present study of the angular diameters of scintillating radio sources was severely limited by the sensitivity of the  $10,000 \text{ m}^2$  array. Thus one could not make a detailed study of the angular distribution of radio sources at 103 MHz. With the new system one can make scintillation measurements each day on a very large number of IPS sources and thereby study the angular distribution of sources as a function of galactic latitude. These observations may enable us to model the scattering in the galaxy at 103 MHz. Recent work (Hajivassiliou and Duffett-Smith, 1990) has shown that the observed angular distribution inferred by the IPS technique differs from the true picture of the sky due to inherent biases caused by finite sensitivity of the receiving instrument and the indirect methods used for estimation of angular diameters. Also present theoretical models of the solar wind do not cover all elongations causing uncertainty in the turnover of the scintillation index Vs elongation curves. This causes further distortion in the observed estimates . It is hoped that with the  $20,000 \text{ m}^2$  array a large amount of data can be collected and the data quality improved by correcting the observations of each source for variations in the power of the irregularity spectrum correlated over many neighboring sources.

An offshoot of simultaneously observing in 32 independent declination beams would be the production of a sensitive radio source survey. While the single receiver used with the  $10,000 \text{ m}^2$  array would require a minimum of 32 days to scan the sky once, the upgraded  $20,000 \text{ m}^2$  array could produce a picture of the sky every 24 hours. Averaging the observations of every beam a large number of times would then get rid of

the spurious day-to-day variations and bring out the near-true D.C. flux of the sources.

## 6.2 Occultation Observations by Cometary Ion Tails.

The biggest drawback in the present observations of scintillation measurements due to cometary ion tails was the fact that control sources could not be monitored simultaneously. The best that one could do was to observe other sources in the same or adjacent beams after the occultation event. With the enhanced sensitivity of the Thaltej array and the use of many beams simultaneously, cometary occultations of radio sources, when they occur, can be studied in more detail. Also if the comet is bright and the occulted source is a strong scintillator at 103 MHz, a simultaneous 3-station measurement can be made and used to derive the velocity of the plasma in the tail of the comet. This information, if available, could greatly increase the accuracies in the determination of the scale sizes and rms electron density deviations in cometary plasma tails. Moreover existing data, either insitu or ground based, is confined almost entirely to the coma and near-nucleus regions of the comet. IPS radio observations are typically well downstream of the nucleus and many more similar observations, to create a larger data base, will be required before an attempt is made to model cometary plasma at large distances downstream of the nucleus. The  $20,000 \text{ m}^2$  array at Thaltej and the two out stations can be used to build up such a data base whenever possible.

### 6.3 Velocity Measurements and Large-scale Structure of the Interplanetary Medium.

Ever since Dennison and Hewish (1967) first showed that multi-station observations of compact radio sources could be used to estimate the solar wind velocity, ground based multi-station IPS velocity measurements have been used successfully to study the large-scale structure of the IPM. Recently Manoharan and Ananthakrishnan (1990) have demonstrated that single station IPS measurements can also be used to derive solar wind velocities by fitting a model to observed scintillation spectra.

Three station measurements (Coles and Maagoe, 1972; Coles and Rickett, 1976) have been used to study the latitudinal variation of solar wind speeds and Sime and Rickett (1978) have compared six rotation averages of IPS velocity with coronal hole observations. This analysis led to the identification of the fact that high-speed streams observed in the ecliptic near solar minimum were extensions of polar streams from polar coronal holes. Kojima and Kakinuma (1987) mapped observed velocities back to the source surface near the sun and tried to relate speed to distance from the neutral sheet. More recently (Lindblad, 1990) using spacecraft data has shown a very good correlation between inferred solar sources of high-speed solar wind streams and extended white light coronal features.

Using IPS data obtained at Thaltej between 1984 and 1990 and the single station method of determining solar wind velocities (Manoharan and Ananthakrishnan, 1990) the derived velocities were mapped back to

the source surface, along Archimedian spirals, to create plots of velocity distribution (Alurkar and Vats, 1991) on the source surface. Such plots (V-maps) are very useful in determining large-scale features of the solar wind structure. Figure 6.1 and 6.2 are two examples of such V-maps for the years 1986 and 1990 the solar minimum and near-maximum years respectively. Since the number of sources used was small the maps were made by averaging over 10 solar rotations and also into  $15^\circ \times 15^\circ$  bins on the source surface. Speeds  $\leq 450 \text{ km s}^{-1}$  are marked by red contours while speeds  $< 450 \text{ km s}^{-1}$  are marked by green contours. The detailed analysis of this data is underway and has not been included as a part of this thesis.

Preliminary analysis, though, has shown good correlation between the regions of low velocities and the position of the neutral line. Mid latitude high speed contours have also shown a good correlation with positions of coronal holes identified by 10830 Å synoptic pictures. The existing measurements, due to having few sources, have to be averaged over an entire year to give meaningful results. Even then the contour density is weak in some regions as can be seen from the two maps (Figures 6.1 and 6.2). It is hoped that the 20,000  $\text{m}^2$  array will provide a sufficient density of data so as to be able to analyze data from rotation to rotation, thereby making the study with higher resolution and, possibly, identifying streams lasting for a rotation or so.

Similar to the V-maps described above, large-scale features in the IPM between the sun and the earth can be studied by measuring daily

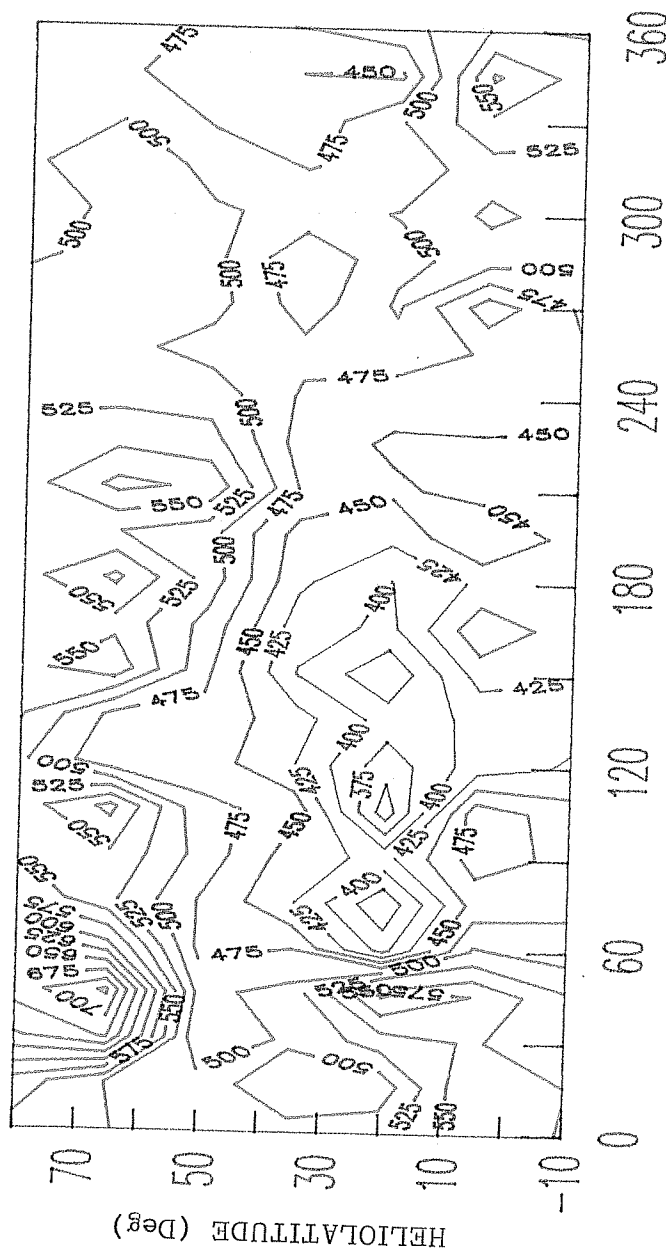
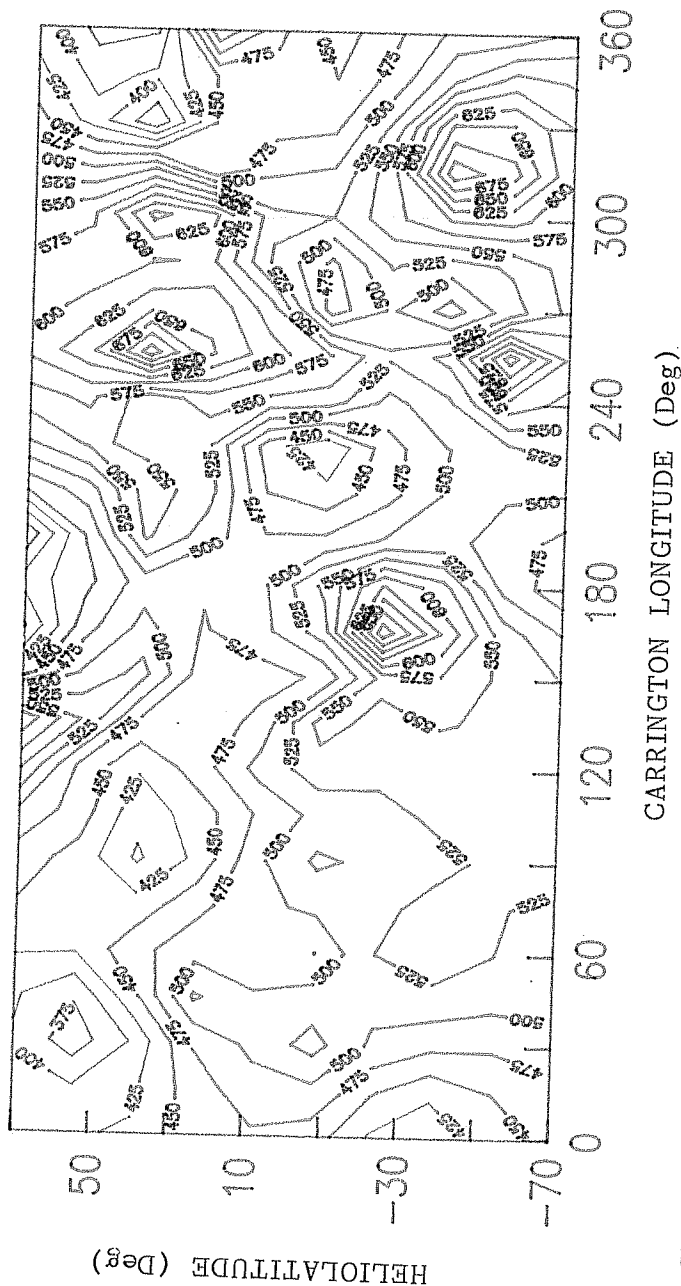


Figure 6.1 Shows the measured solar wind velocities in 1986 using data from Thaltej. The velocities have been averaged over 10 rotations and mapped back along Archimedean spirals to the source surface near the sun. The velocities have also been averaged over 15° x 15° bins on the source surface. Velocities greater than 450 km/sec are shown in red while velocities less than 450 km/sec are shown in green.



**Figure 6.2** Shows the measured solar wind velocities in 1990 using data from Thaltej. The velocities have been averaged over 10 rotations and mapped back along Archimedian spirals to the source surface near the sun. The velocities have also been averaged over  $15^\circ \times 15^\circ$  bins on the source surface. Velocities greater than 450 km/sec are shown in red while velocities less than 450 km/sec are shown in green.

enhancements  $g = \frac{\Delta S}{\overline{\Delta S}}$ , of a large number of scintillating radio sources and plotting the g-values on the sky to create maps called g-maps (Gapper *et al.*, 1983; Tappin *et al.*, 1984; Hewish *et al.*, 1985; Hewish and Duffett-Smith, 1987). Here  $\Delta S$  is the daily measurement of scintillating flux of a given source at a given elongation while  $\overline{\Delta S}$  is the long term average scintillating flux of the source at the corresponding elongation. Such g-maps can enable one to track major interplanetary disturbances from day-to-day and coupled with velocity measurements both the structure and dynamics of the IPM can be studied. It is hoped that the 20,000 m<sup>2</sup> array along with the two 5,000 m<sup>2</sup> arrays at Rajkot and Surat will achieve these objectives in the future.

## REFERENCES

- Alfvén, H. (1957). *Tellus*. 9, 92.
- Alurkar, S.K., Bhonsle, R.V., Sharma, R., Bobra, A.D., Sohan Lal, Nirman, N.S., Venat, P., and Sethia, G. (1982). *J.IETE*. 28, No.11, 577.
- Alurkar, S.K., Bhonsle, R.V., and Sharma, A.K. (1986). *Nature*. 322, 439.
- Alurkar, S.K., Slee, O.B. and Bobra, A.D. (1986). *Aust. J. Of Phys.* 39, 433.
- Alurkar, S.K., Bobra, A.D., Nirman, N.S., Venat, P., and Janardhan, P. (1989 b). *Indian Journal of Pure and Applied Phys.* 27, 322.
- Alurkar, S.K., Sharma, A.K., Janardhan, P., and Bhonsle, R.V. (1989). *Nature* 338, 211.
- Alurkar, S.K., Vats, H.O. (1991). (Presented at the Indo-US workshop On Interplanetary Scintillation and Propagating Disturbances, Ahmedabad, Sept. 1991).
- Ananthakrishnan, S., Bhandari, S.M., and Rao, A.P. (1975). *Astrophys. Space Sci.* 37, 275.
- Ananthakrishnan, S., Manoharan, P.K., and Venugopal, V.R. (1987). *Nature* 329, 698.



- Ananthakrishnan, S., Manoharan, P.K., and Venugopal, V.R. (1989). *Nature* 338, 212
- Armstrong, J.W. and Coles, W.A. (1978). *Astrophys. J.* 220, 346.
- Belton, M.J.S., and Brandt, J.C. (1966). *Astrophys. J. Suppl.* 13, 125
- Bhandari, S.M., Ananthakrishnan, S., and Rao, A., Pramesh (1974). *Aust. J. Phys.* 27, 121.
- Biermann, L., (1951). *J. Astrophys.* 29, 274.
- Bobra, A.D., Selvaraj, M., Alurkar, S.K., and Bhonsle, R.V. (1981). *J. IETE*, 27, 569.
- Booker, H.G. (1958). *Proc. IRE.* 46, No. 1, 298.
- Brandt, J. C. and Mendis, D. A. (1979). *Solar System Plasma Physics. Vol - II*, Eds. Kennel, C. F., Lazerotti, L.J., and Parker, E. N. (Amsterdam: North Holland Publ. Co.), pp. 253.
- Brandt, J. C., Hawley, J. D., and Niedner, M. B. (1980). *Astrophys. J.* 241, L51.
- Buckley, R., (1971). *Planet Space Sci.* 19, 421.
- Budden, K.G., and Uscinski, B.J. (1970). *Proc. Roy. Soc. Lond. A.* 316, 315.
- Burlaga, L.F. and Ness, N. F. (1968). *Can. J. of Phys.* 46, S962.
- Butler, J. (1966). *Microwave Scanning Antennas, III*. N.Y. Acad Press. pp. 254. ed. Hansen, R.C.
- Butler, J. and Lowe, R. (1961). *Electron Design* 9, 170.
- Celnik, W.E. and Th. Schmidt-Kaler. (1987). *Astron. Astrophys.* 187, 233.

- Chernov, L.A. (1960). *Wave Propagation in a Random Medium*. Dover, New York.
- Cohen, M.H., Gundermann, E.J., Hardbeck, J.B., and Sharp, L.E. (1967). *Astrophys. J.* **147**, 449.
- Cohen, M.H., Gunderman, E.J., and Harris, D.E. (1967). *Astrophys. J.*, **150**, 767.
- Cohen, M.H. and Cronyn, W.M. (1974). *Astrophys. J.* **192**, 193.
- Coles, W.A. and Maagoe, S. (1972). *Journal Geophys. Res.* **77**, 5622.
- Coles, W.A. and Rickett, B.J. (1976). *J. Geophys. Res.* **81**, 4797.
- Coles, W.A., Rickett, B.J., and Rumsey, V.H. (1974). *Solar Wind Three*. ed. Russell, C.T. Proc. of the Third Solar Wind Conference, Asilomar.
- Cordes, J.M., Weisberg, J.M. and Boriakoff, V. (1985). *Ap J*, **288**, 221.
- Cordes, J.M., Spangler, S.R., Weisberg, J.M., and Clifton, T.R. (1988). *AIP Conf. Proc.* **174**, ed. Cordes, J.M., Rickett, B.J. and Backer, D.C. (New York: AIP), pp. 180.
- Cronyn, W.M., (1970). *Astrophys. J.* **161**, 755.
- Davis Jr., L.J., Smith, E.J., Coleman Jr., P.J., and Scnett, C. P. (1966). *The Solar Wind*. Ed. Mackin Jr., R. J. and Neugebauer, M. (Pergamon Press, Oxford).
- Delaney, W.P. (1962). *IRE Trans. Military Electron.* **6**, 179.
- Dennison, B., Thomas, M., Booth, R.S., Brown, R.L., Broderick, J.J. and Condon, J.J. (1984). *Astron. Astrophys.*, **135**, 199.
- Duffett- Smith, P.J. (1976). (*Ph.D Thesis., Camb.Univ.* ).

- Duffett-Smith, P.J. and Readhead, A.C.S. (1976). *Mon. Not. Roy. Astron. Soc.* **174**, 7.
- Erickson, W.C. (1964). *Astrophys. J.* **139**, 1290.
- Fey, A.L., Spangler, S.R., and Mutel, R.L. (1989). *Ap J.*, **337**, 730.
- Fey, A.L., Spangler, S.R., and Cordes, J.M. (1991). *Ap J.*, **372**, 132.
- Gapper, G.R., Hewish, A., Purvis, A. and Duffett-Smith, P.J. (1982). *Nature*, **296**, 633.
- Hajivassiliou, C.A. and Duffett-Smith, P.J. (1987). *Mon. Not. R. Astron. Soc.* **229**, 485.
- Harris, D.E., Zeissig, G.A. and Lovelace, R.V. (1970). *Astron. Astrophys.* **8**, 98.
- Hewish, A. (1955). *Proc. Roy Soc. London. A.* **228**, 238.
- Hewish, A. and Wyndham, J.D. (1963). *Mon. Not. Roy. Astr. Soc.* **126**, 649.
- Hewish, A., Scott, P.F. and Wills, D. (1964). *Nature*. **203**, 1214.
- Hewish, A and Symonds, M.D. (1969). *Planet. Space Sci.* **17**, 313.
- Hewish, A. (1971). *Astrophys. J.* **163**, 645.
- Hewish, A. (1975), *Science*. **188**, 1079.
- Hewish, A., Tappin, S.J., and Gapper, G.R. (1985). *Nature* **314**, 137.
- Hewish, A., and Duffett-Smith, P.J. (1987). *Planet. Space Sci.* **35**, No. 4, 487.
- Intriligator, D.S. and Wolfe, J.H. (1970). *Astrophys. J. Lett.* **162**, L187.

- Ip, W.H., and Axford, W.I. (1982). *Comets* (ed. Wilkening, L.L). *The Univ. of Arizona Press, Tuscon*, 588.
- Ip, W.H., Fink, U. and Johnson, J.R. (1985). *Astrophys.J.* **293**, 609.
- Janardhan, P., Alurkar, S.K., Bobra, A.D., and Slee, O.B. (1991a). *Aust. J. Phys.* **44**, No. 5, 565.
- Janardhan, P., Alurkar, S.K., Bobra, A.D., and Slee, O.B., Waldron, D. (1991 b). *Aust. J .Phys..* (In Press).
- Jockers, K., Lüst, R., and Nowak, Th. (1972). *Astron. Astrophys.* **21**, 199.
- Jockers, K. (1981). *Icarus.* **47**, 397.
- Jockers, K. (1985). *Astron. Astrophys. Suppl. Ser.* **62**, 791.
- Jokipii, J.R. and Hollweg, J.V. (1970). *Astrophys. J.* **160**, 745.
- Jokipii, J.R. and Lee, L.C. (1973). *Astrophys. Journal.* **182**, 317.
- Kaufmann, J.J. (1976). (*Ph.D Thesis, University of California, San Diego* ).
- Keller, H.U., Delemare, W. A., Hubener, W.F., Reitsema, H.J., Schmidt, H.U., Whipple, F.L., Curdt, W., Kramm, R., Thomas, N., Arpigny, C., Barbieri, C., Bonnet, R.M., Cazes, S., Coradini, M., Cosmovici, C.B., Hughes, D.W., Jamar, C., Malaise, D., Schmidt, K., Schmidt, W.K.H. and Seige, P. (1987). *Astron. Astrophys.* **187**, 807.
- Kojima, M., and Kakinuma, T. (1987). *J. Geophys. Res.* **92**, 7269.
- Kraus, J.D. (1966). *Radio Astronomy*. N.Y. McGraw Hill.
- Lindblad, B.A. (1990). *Astrophysics and Space Science.* **170**, 55.

- Little, C.G. and Lovell, A.C.B. (1950). *Nature*. **165**, 423.
- Little, L.T. and Hewish, A. (1966). *Mon. Not. Roy. Astron. Soc.* **134**, 221.
- Little, L.T. and Hewish, A. (1968). *Mon. Not. Roy. Astr. Soc.* **138**, 393.
- Little, L.T. (1971). *Astron. Astrophys.* **10**, 301.
- Little, L.T. (1976). *Meth. Exptl. Phys.* **12c**, 118.
- Lovell, R.V.E., Salpeter, E.E., Sharp, L.E. and Hariss, D.E. (1970). *Astrophys. J.* **159**, 1047.
- Manoharan P.K. and Ananthakrishnan, S. (1990). *Mon. Not. Roy. Astron. Soc.* **244**, 691.
- Marians, M. (1975 a). (*Ph.D. Thesis, Univ. Of California, San Diego*).
- Marians, M. (1975 b). *Radio Science*. **10**, 115.
- Matheson, D.N. and Little, L.T. (1971). *Planet. Space Sci.* **19**, 1615.
- Miller, F.D. (1970). *Icarus* . **37**, 443.
- Ness, N.F. and Donn, B.D. (1965). *Mem. Soc. Roy. Liege, Ser.* **5**, 12, 141.
- Neugebauer, M. (1975). *J. Geophys. Res.* **80**, 998.
- Okoye, S. and Hewish, A. (1967). *Mon. Not. Roy. Astr. Soc..* **137**, 287.
- Oort J. (1950). *Bull. Astron. Inst. Netherlands*. **11**, 91.
- Parker, E.N. (1958 a). *Astrophys. J.* **128**, 664.
- Parker, E.N. (1958 b). *Phys. of Fluids*. **1**, No.3, 171.

- Parker, E.N. (1963). *Interplanetary Dynamical Processes* (Interscience Publishers, New York).
- Prokhorov, A.M., Bunkin, F.V., Gochelashvily, K.S., and Shishov, V.I. (1975). *Proc. IEEE.* **63**, 790.
- Purvis, A. (1981). (*Ph.D. Thesis, Univ. Of Cambridge*).
- Rahe, J., Donn, B., and Wurm, K. (1969). *Atlas of Cometary Forms*. (Washington : NASA SP- 198).
- Rao, A.P., Bhandari, S.M. and Anantahkrishnan, S. (1974). *Aust. J. of Phys.* **27**, 105.
- Ratcliffe, J.A. (1956). *Rep. Progr. Phys.* **19**, 188.
- Readhead, A.C.S. (1971). *Mon. Not. Roy. Astron. Soc.* **155**, 185.
- Readhead, A.C.S. and Hewish, A. (1972). *Nature.* **236**, 440.
- Readhead, A.C.S., and Hewish, A. (1974). *Mem. R. Astr. Soc.* **78**, 1.
- Readhead, A.C.S., Kemp, M.C. and Hewish, A. (1978). *Mon. Not. Roy. Astron. Soc.* **185**, 207.
- Resch, G.M. (1974). (*Ph.D Thesis, Florida State University* ).
- Rickett, B.J. (1969). *Nature.* **221**, 158.
- Rickett, B.J. (1973). *J. Geophys. Res.* **78**, 1543.
- Rickett, B.J. (1977). *Ann. Rev. Astron . Astrophys.* **15**, 479.
- Rosenberg, R.L. and Coleman, P.J. Jr. (1970). *Solar Phys.* **15**, 72.

- Rumsey, V.H. (1975). *Radio Science*. **10**, 107.
- Saito, T., Saito, K., Aoki, T. and Yumoto, K. (1987). *Astr. Astrophys.* **187**, 201
- Salpeter, E.E. (1967). *Astrophys.J.* **147**, 433.
- Scherb, F., Magee-Sauer, K., Roesler, F.L., and Harlander, J. (1990). *Icarus* **86**, 172.
- Scheuer, P.A.G. (1968). *Nature*. **218**, 920.
- Schmidt, H.U., and Wegmann, R. (1982). *Comets* (Ed. Wilkening, L.L.) *The Univ. Of Arizona Press, Tuscon*. 538.
- Schmidt-Voigt, M. (1989). *Astron. Astrophys.* **210**, 433.
- Schulz, M. (1973). *Astrophys. Space Sci.* **24**, 371.
- Schwenn, R (1990). **Physics of the Inner Heliosphere** - Springer-Verlag , Ed. Schwenn, R and Marsch, E.
- Shelton, J.P. and Kelleher, K. S. (1961). *IRE Trans. Antennas Propagation*. **9**, 154.
- Sime, D.G., and Rickett, B.J. (1978). *J. Geophys. Res.* **83**, 5757.
- Slee, O.B., Bobra, A.D., Waldron, D. and Lim, J. (1990). *Aust.J.Phys.* **43**, 801.
- Slee, O.B., Mc Connell, D., Lim, J., and Bobra, A.D. (1987). *Nature*. **325**, 699.
- Smith, E. J. (1964). *Space Physics*. Eds. Le Galley, D.P. and Rosen A. (John Wiley and Sons, New York).
- Smith, E.J., Tsurutani, B. and Rosenberg, R.L. (1978). *J. Geophys. Res.* **83**, 717.

- Smith, F.G. (1950). *Nature*. **165**, 422.
- Spangler, S.R., Mutel, R.L., Benson, J.M. and Cordes, J.M. (1986). *Ap J.*, **301**, 312.
- Tappin, S.J. (1986). *Planet Space Sci.* **34**, 93.
- Tatarski, V.I. (1961). *Wave Propagation in a Turbulent Medium*. Dover, New York.
- Unti, T. and Russell, C. T. (1976). *J. Geophys. Res.* **81**, 469.
- Vandenberg, N.R. (1974). (*Ph.D Thesis, University of Maryland* ).
- Whipple, F.L. (1950). *Astrophys. J.* **111**, 375.
- Whipple, F.L. (1951). *Astrophys. J.* **113**, 464.
- Wilcox, J.M. and Colburn, D.S. (1970). *J. Geophys. Res.* **75**, 6366.
- Wilcox, J.M. and Ness, N.F. (1965). *J. Geophys. Res.* **70**, 5793.